

<sup>1</sup> SEARCH FOR  $t\bar{t}Z' \rightarrow t\bar{t}t\bar{t}$  PRODUCTION IN THE MULTILEPTON FINAL STATE IN  
<sup>2</sup>  $pp$  COLLISIONS AT  $\sqrt{s} = 13$  TEV WITH THE ATLAS DETECTOR

<sup>3</sup> By

<sup>4</sup> Hieu Le

<sup>5</sup> A DISSERTATION

<sup>6</sup> Submitted to  
<sup>7</sup> Michigan State University  
<sup>8</sup> in partial fulfillment of the requirements  
<sup>9</sup> for the degree of

<sup>10</sup> Physics — Doctor of Philosophy

<sup>11</sup> 2025

## ABSTRACT

13 Lorem ipsum dolor sit amet, consectetur adipiscing elit, sed do eiusmod tempor incididunt ut  
14 labore et dolore magna aliqua. Ut enim ad minim veniam, quis nostrud exercitation ullamco  
15 laboris nisi ut aliquip ex ea commodo consequat. Duis aute irure dolor in reprehenderit in  
16 voluptate velit esse cillum dolore eu fugiat nulla pariatur. Excepteur sint occaecat cupidatat  
17 non proident, sunt in culpa qui officia deserunt mollit anim id est laborum.

## ACKNOWLEDGMENTS

- <sup>19</sup> Advisor: Reinhard Schwienhorst
- <sup>20</sup> Postdoc: Binbin Dong
- <sup>21</sup> Committee
- <sup>22</sup> MSU group
- <sup>23</sup> ATLAS analysis group
- <sup>24</sup> Friend: Daniel, Grayson, Bella, Eric, Jordan
- <sup>25</sup> Other friends: Jasper, Adam, Brittany
- <sup>26</sup> Parents
- <sup>27</sup> Spouse: Allen Sechrist
- <sup>28</sup> ATLAS in general & funding agencies

## PREFACE

<sup>30</sup> This is my preface. remarks remarks remarks

## TABLE OF CONTENTS

31	<b>List of Tables . . . . .</b>	vii
32	<b>List of Figures . . . . .</b>	ix
33	<b>KEY TO ABBREVIATIONS . . . . .</b>	xi
34	<b>Chapter 1. Introduction . . . . .</b>	1
35	<b>Chapter 2. Theoretical Overview . . . . .</b>	5
36	2.1 The Standard Model . . . . .	5
37	2.1.1 Elementary particles . . . . .	5
38	2.1.2 Mathematical formalism . . . . .	9
39	2.1.2.1 Quantum chromodynamics . . . . .	10
40	2.1.2.2 Electroweak theory . . . . .	11
41	2.1.2.3 Higgs mechanism . . . . .	14
42	2.2 Beyond the Standard Model . . . . .	17
43	2.2.1 Top-philic vector resonance . . . . .	17
44	2.2.2 BSM $t\bar{t}Z' \rightarrow t\bar{t}t\bar{t}$ . . . . .	19
45	<b>Chapter 3. LHC &amp; ATLAS Experiment . . . . .</b>	21
46	3.1 The Large Hadron Collider . . . . .	21
47	3.1.1 Overview . . . . .	21
48	3.1.2 LHC operations . . . . .	23
49	3.1.3 Physics at the LHC . . . . .	24
50	3.2 The ATLAS detector . . . . .	24
51	3.2.1 Inner detector . . . . .	27
52	3.2.2 Calorimeter systems . . . . .	28
53	3.2.3 Muon spectrometer . . . . .	30
54	3.2.4 Trigger & data acquisition . . . . .	32
55	<b>Chapter 4. Particle Reconstruction &amp; Identification . . . . .</b>	33
56	4.1 Primary reconstruction . . . . .	33
57	4.1.1 Tracks . . . . .	33
58	4.1.2 Vertices . . . . .	34
59	4.1.3 Topological clusters . . . . .	35
60	4.2 Jets . . . . .	36
61	4.2.1 Jet reconstruction . . . . .	37
62	4.2.2 Flavor tagging . . . . .	38
63	4.3 Leptons . . . . .	42
64	4.3.1 Electrons . . . . .	42
65	4.3.2 Muons . . . . .	45
66	4.4 Missing transverse momentum . . . . .	47

67	4.5 Overlap removal . . . . .	48
68	4.6 Object definition . . . . .	49
69	<b>Chapter 5. Data &amp; Simulated Samples</b> . . . . .	<b>50</b>
70	5.1 Data samples . . . . .	50
71	5.2 Monte Carlo samples . . . . .	50
72	5.2.1 $t\bar{t}Z'$ signal samples . . . . .	51
73	5.2.2 Background samples . . . . .	53
74	<b>Chapter 6. Analysis Strategy</b> . . . . .	<b>55</b>
75	6.1 Event selection . . . . .	55
76	6.1.1 Event categorization . . . . .	56
77	6.2 Analysis regions . . . . .	57
78	6.2.1 Signal regions . . . . .	57
79	6.2.2 Control regions . . . . .	60
80	6.3 Background estimation . . . . .	63
81	6.3.1 Template fitting for fake/non-prompt estimation . . . . .	64
82	6.3.2 Charge misidentification data-driven estimation . . . . .	64
83	6.3.3 $t\bar{t}W$ background data-driven estimation . . . . .	67
84	<b>Chapter 7. Systematic Uncertainties</b> . . . . .	<b>70</b>
85	7.1 Experimental uncertainties . . . . .	70
86	7.1.1 Luminosity & pile-up reweighting . . . . .	70
87	7.1.2 Leptons . . . . .	70
88	7.1.3 Jets . . . . .	72
89	7.1.4 Missing transverse energy . . . . .	74
90	7.2 Modeling uncertainties . . . . .	75
91	7.2.1 Signal and irreducible background uncertainties . . . . .	75
92	7.2.2 Reducible background uncertainties . . . . .	77
93	<b>Chapter 8. Results</b> . . . . .	<b>79</b>
94	8.1 Statistical interpretation . . . . .	79
95	8.1.1 Profile likelihood fit . . . . .	79
96	8.1.2 Exclusion limit . . . . .	82
97	8.2 Fit results . . . . .	83
98	<b>Chapter 9. Summary</b> . . . . .	<b>89</b>
99	<b>References</b> . . . . .	<b>90</b>

# 100 List of Tables

101	Table 4.1: Overlap removal process for this analysis, applied sequentially from top to 102 bottom. . . . .	48
103	Table 4.2: Summary of object selection criteria used in this analysis. $\ell_0$ refers to the 104 leading lepton in the event. . . . .	49
105	Table 5.1: Summary of all HLT triggers used in this analysis. Events are required to 106 pass at least one trigger. . . . .	51
107	Table 5.2: Summary of all Monte-Carlo samples used in this analysis. $V$ refers to 108 an EW ( $W^\pm/Z/\gamma^*$ ) or Higgs boson. Matrix element (ME) order refers 109 to the order in QCD of the perturbative calculation. Tune refers to the 110 underlying-event tune of the parton shower (PS) generator. . . . .	52
111	Table 6.1: Definitions of signal, control and validation regions (VR) used in this anal- 112 ysis. $N_{\text{jets}}$ and $N_b$ refers to the number of jets and number of $b$ -tagged 113 jets respectively. $\ell_1$ refers to the leading lepton, $\ell_2$ refers to the subleading 114 lepton and so on. $H_T$ refers to the $p_T$ scalar sum of all leptons and jets 115 in the event. $m_{\ell\ell}$ refers to the dilepton invariant mass, which must not 116 coincide with the $Z$ -boson mass range of 81-101 GeV for SS2L+3L events.	58
117	Table 6.2: Definitions of SR sub-regions. Events are sorted into different sub-regions 118 based on the number of $b$ -tagged jets and leptons present. . . . .	60
119	Table 6.3: List of possible assigned values for DFCAA. . . . .	62
120	Table 7.1: Summary of the experimental systematic uncertainties considered in this 121 analysis. . . . .	71
122	Table 8.1: Normalization factors for backgrounds with dedicated CRs, obtained from 123 a simultaneous fit in all CRs and SR under the background-only hypothesis. 124 The nominal pre-fit value is 1 for all NFs and 0 for the scaling factors $a_0$ and 125 $a_1$ . Uncertainties shown include both statistical and systematic uncertainties.	84

126 Table 8.2: Pre-fit and post-fit background yields in the inclusive SR. The number of  
 127 data events and pre-fit estimate signal yields are also shown. Background  
 128 yields shown are obtained from the fit using the  $t\bar{t}Z'$  signal sample with  
 129  $m_{Z'} = 2$  TeV. Total yield uncertainty differs from the quadrature sum of  
 130 constituent uncertainties due to correlation and anticorrelation effects. . . . .  
 131 Table 8.3: Post-fit impact of uncertainty sources on the signal strength  $\mu$ , grouped by  
 132 categories. Values shown are obtained from the fit using the  $t\bar{t}Z'$  signal  
 133 sample with  $m_{Z'} = 2$  TeV. Impact on  $\mu$  is evaluated for each uncertainty  
 134 category by re-fitting with the corresponding set of NPs fixed to their best-  
 135 fit values. Total uncertainty differs from the quadrature sum of constituent  
 136 uncertainties due to correlation between NPs in the fit. . . . . . . . . . . . . . . . .  
 87  
 88

# List of Figures

<sup>137</sup>	Figure 2.1: Particles within the SM and their properties. . . . .	6
<sup>139</sup> <sup>140</sup> <sup>141</sup>	Figure 2.2: Feynman diagram for $t\bar{t}$ production and subsequent decay processes. Top quark decays into a $W$ -boson and $b$ -quarks, and $W$ -boson can decay to a $q\bar{q}$ or a $\ell\nu_\ell$ pair. . . . .	8
<sup>142</sup> <sup>143</sup> <sup>144</sup> <sup>145</sup> <sup>146</sup>	Figure 2.3: Illustration of a common representation of the Higgs potential. Before SSB, the ground state $\phi(0)$ is located at A which is symmetric with respect to the potential. A perturbation to this state fixes the ground state energy $ \phi(0) ^2$ to a particular value at B, "spontaneously" breaking the symmetry and degeneracy in $ \phi(0) ^2$ . . . . .	15
<sup>147</sup> <sup>148</sup> <sup>149</sup>	Figure 2.4: Feynman diagrams for tree level $Z'$ production in association with (a) $t\bar{t}$ , (b) $tj$ (light quark) and (c) $tW$ , decaying to final states containing (a) $t\bar{t}t\bar{t}$ or (b)(c) $t\bar{t}t$ . . . . .	19
<sup>150</sup> <sup>151</sup>	Figure 2.5: Branching ratios for $t\bar{t}t\bar{t}$ decay. The same-sign dilepton and multilepton channels together forms the SSML channel. . . . .	20
<sup>152</sup>	Figure 3.1: The full CERN accelerator complex as of 2022. . . . .	22
<sup>153</sup> <sup>154</sup>	Figure 3.2: Current and future timeline of LHC operations as of 2025 with corresponding center-of-mass energies and projected integrated luminosities. . . . .	23
<sup>155</sup> <sup>156</sup>	Figure 3.3: Summary of predicted and measured cross-section for SM processes at the LHC at different center-of-mass energies . . . . .	25
<sup>157</sup> <sup>158</sup> <sup>159</sup>	Figure 3.4: A cross section slice of the ATLAS detector showing different subsystems along with visualization of different types of particles traveling through the detector . . . . .	26
<sup>160</sup>	Figure 3.5: Cutaway illustration of the inner detector along with its subsystems. . . . .	27

161	Figure 3.6: Cutaway illustration of the calorimeter system including the EM, hadronic 162 and LAr forward calorimeters . . . . .	29
163	Figure 4.1: Stages of topo-cluster formation corresponding to each threshold. In (a), 164 proto-clusters are seeded from cells with adequate signal significance $\zeta_{\text{cell}}^{\text{EM}}$ . 165 The clusters are further merged and split in (b) according to a predefined 166 cluster growth threshold. The process stops in (c) when all sufficiently 167 significant signal hits have been matched to a cluster. . . . .	36
168	Figure 4.2: Jet energy scale calibration sequence for EM-scale jets. . . . .	38
169	Figure 4.3: Overview of the GN2 architecture. The number of jet and track features 170 are represented by $n_{\text{jf}}$ and $n_{\text{tf}}$ respectively. The global jet representation 171 and track embeddings output by the Transformer encoder are used as 172 inputs for three task-specific networks. . . . .	40
173	Figure 4.4: The $c$ -, light- and $\tau$ -jet rejection rate as a function of $b$ -tagging efficiency 174 for GN2 and DL1d using (a) jets in the $t\bar{t}$ sample, and (b) jets in the $Z'$ 175 sample. The performance ratios of GN2 to DL1d are shown in the bottom 176 panels. . . . .	41
177	Figure 6.1: Post-fit background composition in each analysis region and sub-region. 178 The fit was performed using ideal pseudo-datasets (Asimov data) in the SR. . . . .	59
179	Figure 6.2: Pre-fit kinematic distributions and event compositions for several observ- 180 ables in the inclusive SR. The shaded band represents the uncertainty in 181 the total distribution. The first and last bins of each distribution contains 182 underflow and overflow events respectively. . . . .	61
183	Figure 6.3: Charge flip rate calculated for SR and CR $t\bar{t}W$ in bins of $ \eta $ and $p_{\text{T}}$ . . . . .	66
184	Figure 7.1: Combined QmisID uncertainty rate for SR in bins of $ \eta $ and $p_{\text{T}}$ . . . . .	78
185	Figure 8.1: Observed (solid line) and expected (dotted line) upper limits as a function 186 of the $Z'$ mass at 95% CL on the cross-section of $pp \rightarrow t\bar{t}Z'$ production 187 times the $Z' \rightarrow t\bar{t}$ branching ratio. The region above the observed limit is 188 excluded. The solid blue line represents the theoretical signal cross-section 189 with $c_t = 1$ at LO in QCD. The green and yellow bands represent the 190 68% ( $\pm\sigma$ ) and 95% ( $\pm 2\sigma$ ) confidence intervals respectively. . . . .	85
191	Figure 8.2: Comparison between data and post-fit prediction for the discriminant ob- 192 servable in each non-prompt and $t\bar{t}W$ background CR. The fit is per- 193 formed simultaneously in all CRs and SR under the background-only 194 hypothesis. The lower panel shows the ratio between data and post-fit 195 predictions. The shaded band represents the total uncertainty on the fit.	86

## KEY TO ABBREVIATIONS

197

### Physical & Mathematical Quantities

198  $\chi^2$  chi-squared199  $d_0$  transverse impact parameter200  $\Delta R$  angular distance201  $\sqrt{s}$  center-of-mass energy202  $\eta$  pseudorapidity203  $E_T$  transverse energy204  $E_T^{\text{miss}}$  missing transverse energy205  $\Gamma$  decay width206  $\gamma_5$  chirality projection operator207  $\gamma_\mu$  Dirac matrices208  $H_0$  null hypothesis209  $H_T$  scalar sum of transverse momenta  $p_T$  of all objects in an event210  $\mathcal{L}$  Lagrangian211  $\mathcal{L}(\theta)$  likelihood function212  $L$  instantaneous luminosity213  $m_{\ell\ell}$  dilepton invariant mass214  $\mu$  signal strength215  $\mu_F$  factorization scale216  $\mu_R$  renormalization scale217  $N_{\text{jets}}$  number of jets/jet multiplicity218  $\mathcal{O}(n)$  on the order of  $n$ 219  $\mathcal{P}$  Poisson probability220  $p_T$  transverse momentum

- <sup>221</sup>  $Q$  electric charge  
<sup>222</sup>  $q_\mu$  profile likelihood ratio  
<sup>223</sup>  $\sigma$  standard deviation  
<sup>224</sup>  $\sigma[b]$  cross-section  
<sup>225</sup>  $z_0$  longitudinal impact parameter

<sup>226</sup> **Particles & Processes**

- <sup>227</sup>  $\gamma^*$  virtual photon  
<sup>228</sup>  $gg$  gluon-gluon fusion  
<sup>229</sup>  $pp$  proton-proton  
<sup>230</sup> PbPb lead-lead  
<sup>231</sup>  $q$  quark  
<sup>232</sup>  $q\bar{q}$  quark-antiquark pair  
<sup>233</sup>  $t\bar{t}$  top/anti-top quark pair  
<sup>234</sup>  $t\bar{t}X$  top pair in association with another particle  
<sup>235</sup>  $t\bar{t}t\bar{t}$  four-top-quark  
<sup>236</sup>  $V$  massive vector bosons ( $W^\pm, Z$ )  
<sup>237</sup>  $H$  Higgs in association with a vector boson

<sup>238</sup> **Acronyms**

- <sup>239</sup> **1LOS** one lepton, or two leptons of opposite charges  
<sup>240</sup> **2HDM** two-Higgs doublet model  
<sup>241</sup> **AF3** AtlFast3 fast simulation  
<sup>242</sup> **ALICE** A Large Ion Collider Experiment  
<sup>243</sup> **ATLAS** A Toroidal LHC ApparatuS  
<sup>244</sup> **AWAKE** Advanced WAKEfield Experiment  
<sup>245</sup> **BDT** boosted decision tree  
<sup>246</sup> **BR** branching ratio

- <sup>247</sup> **BSM** Beyond the Standard Model
- <sup>248</sup> **CB** combined muon
- <sup>249</sup> **CERN** European Organization for Nuclear Research
- <sup>250</sup> **CKM** Cabibbo-Kobayashi-Maskawa matrix
- <sup>251</sup> **CL** confidence level
- <sup>252</sup> **CMS** Compact Muon Solenoid
- <sup>253</sup> **CP** charge-parity symmetry
- <sup>254</sup> **CR** control region
- <sup>255</sup> **CSC** Cathode Strip Chambers
- <sup>256</sup> **CTP** Central Trigger Processor
- <sup>257</sup> **ECIDS** Electron Charge ID Selector
- <sup>258</sup> **EFT** effective field theory
- <sup>259</sup> **EM** electromagnetic
- <sup>260</sup> **EW** electroweak
- <sup>261</sup> **FASER** ForwArd Search ExpeRiment
- <sup>262</sup> **FCal** forward calorimeter
- <sup>263</sup> **FS** full detector simulation
- <sup>264</sup> **GNN** graph neural network
- <sup>265</sup> **GRL** Good Run List
- <sup>266</sup> **GSC** Global Sequential Calibration
- <sup>267</sup> **GSF** Gaussian-sum filter
- <sup>268</sup> **GUT** Grand Unified Theory
- <sup>269</sup> **HEC** hadronic endcap calorimeter
- <sup>270</sup> **HF** heavy-flavor
- <sup>271</sup> **HL-LHC** High-Luminosity Large Hadron Collider
- <sup>272</sup> **HLT** High-Level Trigger
- <sup>273</sup> **ID** Inner Detector

- <sup>274</sup> **IP** interaction point
- <sup>275</sup> **JER** jet energy resolution
- <sup>276</sup> **JES** jet energy scale
- <sup>277</sup> **JVT** Jet Vertex Tagger
- <sup>278</sup> **KATRIN** Karlsruhe Tritium Neutrino Experiment
- <sup>279</sup> **L1** Level 1
- <sup>280</sup> **LAr** liquid argon
- <sup>281</sup> **LF** light-flavor
- <sup>282</sup> **LH** likelihood
- <sup>283</sup> **LHC** Large Hadron Collider
- <sup>284</sup> **LHCb** Large Hadron Collider beauty
- <sup>285</sup> **LINAC** linear accelerator
- <sup>286</sup> **LLH** log-likelihood
- <sup>287</sup> **LO** leading order
- <sup>288</sup> **MC** Monte Carlo simulation
- <sup>289</sup> **ME** matrix element
- <sup>290</sup> **ML** multilepton
- <sup>291</sup> **MS** Muon Spectrometer
- <sup>292</sup> **MDT** Monitored Drift Tubes
- <sup>293</sup> **MET** missing transverse energy
- <sup>294</sup> **NF** normalization factor
- <sup>295</sup> **NNJvt** Neural Network-based Jet Vertex Tagger
- <sup>296</sup> **NLO** next-to-leading order
- <sup>297</sup> **NNLO** next-to-next-to-leading order
- <sup>298</sup> **NP** nuisance parameter
- <sup>299</sup> **OP** operating point (also working point)
- <sup>300</sup> **OS** opposite-sign

- <sup>301</sup> **PCBT** pseudo-continuous  $b$ -tagging
- <sup>302</sup> **PDF** parton distribution function
- <sup>303</sup> **POI** parameter of interest
- <sup>304</sup> **PS** parton shower
- <sup>305</sup> **PV** primary vertex
- <sup>306</sup> **QCD** quantum chromodynamics
- <sup>307</sup> **QED** quantum electrodynamics
- <sup>308</sup> **QFT** quantum field theory
- <sup>309</sup> **QmisID** charge mis-identification
- <sup>310</sup> **RPC** Resistive Plate Chamber
- <sup>311</sup> **SCT** Semiconductor Tracker
- <sup>312</sup> **SF** scale factor
- <sup>313</sup> **SM** Standard Model
- <sup>314</sup> **SR** signal region
- <sup>315</sup> **SS** same-sign
- <sup>316</sup> **SSB** spontaneous symmetry breaking
- <sup>317</sup> **SS2L** same-sign dilepton
- <sup>318</sup> **SSML** same-sign dilepton, or more than two leptons of any charges
- <sup>319</sup> **TDAQ** Trigger and Data Acquisition
- <sup>320</sup> **TGC** Thin-Gap Chamber
- <sup>321</sup> **TRT** Transition Radiation Tracker
- <sup>322</sup> **VEV** vacuum expectation value
- <sup>323</sup> **VR** validation region
- <sup>324</sup> **UE** underlying-event

# 325 Chapter 1. Introduction

326     The 20<sup>th</sup> century ushered in a revolutionary period for mankind's understanding of the  
327     fundamental nature of matter and the forces that govern our universe with the development  
328     of special relativity and quantum mechanics, which redefined our understanding of space,  
329     time, energy and matter at the furthest extremes of scale from the vast reaches of the cosmos  
330     to the tiniest constituents of matter. Building on these principles, Quantum Electrodynamics  
331     (QED) [1–3] was developed as the first successful quantum field theory (QFT) describing  
332     electromagnetism. The discovery of beta decay [4] and its paradoxical behaviors within the  
333     framework of QED prompted the prediction of neutrinos and development of the theory of  
334     weak interaction.

335     At around the same time, a spectrum of strongly interacting particles was discovered  
336     [5] as particle accelerators probed deeper into atomic nuclei, leading to the formation of  
337     the quark model in the 1960s and with it a hypothesized new binding force, the strong  
338     force. However, the QFT framework remained incapable of describing the weak and strong  
339     interactions until advancements in gauge theory and the quantization of non-Abelian gauge  
340     via QFT resulted in the formation of Yang-Mills theory [6, 7]. This sparked a renaissance  
341     in modern physics with the unification of electromagnetism and weak force in 1967 under  
342     the framework of electroweak (EW) [8] theory, as well as the development of Quantum  
343     Chromodynamics (QCD) [9, 10] to describe the strong force binding quarks.

344     At this point, the prediction of massless bosons within EW formalism remained a contra-  
345     diction to the predicted massive  $W^\pm$  and  $Z$  bosons that mediate the weak force. This was  
346     resolved by the introduction of EW spontaneous symmetry breaking and the Higgs mech-  
347     anism in 1964 [11–13], which explained the generation of masses for both the EW bosons

348 and fermions. Together, these developments culminated in the Standard Model of parti-  
349 cle physics SM [14], a comprehensive theory that described the electromagnetic, weak, and  
350 strong interactions, classified all known fundamental particles and predicted mathematically  
351 consistent but not yet observed particles. Following its inception, particles predicted by the  
352 Standard Model were gradually observed experimentally, starting with the gluon in 1979  
353 [15], then the  $W^\pm$  and  $Z$  bosons [16, 17], and finally the top quark in 1995 [18, 19]. The  
354 final missing piece was confirmed as the Higgs boson was observed in 2012 independently  
355 by the ATLAS [20] and CMS [21] detectors at the Large Hadron Collider, completing the  
356 Standard Model after a 40-year search and cementing it as the most successful framework  
357 so far describing fundamental constituents of matter and their governing forces.

358 Despite its successes, the Standard Model remains incomplete. Key unanswered questions  
359 include the nature of dark matter [22], which makes up about 27% of the universes energy  
360 content but has no explanation within the Standard Model; the origin of neutrino masses and  
361 their oscillations [23]; the observed matter-antimatter asymmetry in the universe; possible  
362 unification of the EW and strong interaction into a Grand Unified Theory (GUT); and the  
363 hierarchy problem describing the large discrepancy in scales between forces and the apparent  
364 lightness of the Higgs boson compared to values predicted from quantum corrections.

365 After the discovery of the Higgs boson, efforts have been underway to construct new  
366 hypotheses and models in search of beyond the Standard Model (BSM) physics via different  
367 avenues, one of which being direct searches at colliders for new resonances or particles not  
368 predicted by the SM. In particular, the top quark possesses large mass and strong coupling to  
369 the Higgs boson [24] which gives it a special role in many proposed BSM models as a possible  
370 connection with strong coupling to new particles and heavy resonances. In addition, the  
371 top quark has a clean decay signature with well-understood final states and is produced in

abundance at the LHC from  $pp$  collisions in the form of top pairs  $t\bar{t}$  [25, 26]. This dissertation presents a search for the production of a heavy resonance that couples preferentially to top quark (top-philic) in association with a top pair ( $t\bar{t}$ ) in the final state with either two leptons of the same electric charge or at least three leptons (SSML). The search is performed in proton-proton collisions at  $\sqrt{s} = 13$  TeV with the ATLAS detector [27] via the four-top ( $t\bar{t}t\bar{t}$ ) production channel.

A similar search for top-philic heavy resonances was performed using a  $t\bar{t}t\bar{t}$  final state containing either one lepton or two opposite-sign leptons (1LOS) [28] with a much larger branching ratio of 56% and larger irreducible background of SM processes. Despite the small cross-section within the SM, the  $t\bar{t}t\bar{t}$  SSML final state provides heightened sensitivity to BSM physics and higher signal-to-background ratio than inclusive resonance searches (e.g. in dijet or dilepton final states) due to the distinctive signal signature and suppression of large SM background processes present in  $t\bar{t}$ -associated production i.e. diboson ( $VV$ ),  $t\bar{t}$  production with an additional boson ( $t\bar{t}V/ttH+jets$ ) or with additional light leptons from heavy-flavor decays ( $t\bar{t} + HF$ ). The cross-section for  $t\bar{t}t\bar{t}$  production can be enhanced by many proposed BSM models including supersymmetric gluino pair-production [29, 30], scalar gluon pair-production [31, 32], top-quark-compositeness models [33, 34], effective field theory (EFT) operators [26, 35–38] and two-Higgs-doublet models (2HDM) [39–43]. Searching within this channel is particularly motivated by the recent observed excess in the measurement of four-top production in the SSML final state at the LHC by the ATLAS detector [44] with a measured cross-section of  $24^{+7}_{-6}$  fb, almost double the SM prediction of  $13.4^{+1.0}_{-1.8}$  fb.

The search attempts to reconstruct the top-philic resonance directly to search for new physics with minimal dependency on the model choice. In addition, a simplified color-singlet vector boson model [45] is employed for model-dependent interpretations, including

396 setting exclusion limits on the production cross-section and model parameters. Data-driven  
397 background estimation methods are implemented for  $t\bar{t}W$ - one of the dominant irreducible  
398 backgrounds in the analysis - and the charge misidentification background to rectify mis-  
399 modeling related to jet multiplicity in simulated background that were not covered in the  
400 previous 1LOS search [28]. These methods are employed similarly to that in previous SM  
401  $t\bar{t}t\bar{t}$  analyses [44, 46].

402 This dissertation is organized as follows. Chapter 2 presents the formalism of the SM and  
403 relevant BSM concepts. Chapter 3 provides an introduction to the LHC and ATLAS detector.  
404 Chapter 4 describes the reconstruction and identification of physics object from detector  
405 signals. Chapter 5 defines the data and simulated samples used in the analysis. Chapter 6  
406 describes the analysis strategy, including object definition, analysis region description and  
407 background estimation methods. Chapter 7 summarizes the uncertainties involved in the  
408 analysis. Chapter 8 presents the statistical interpretation and analysis results. Finally,  
409 Chapter 9 discusses a summary of the analysis and future outlook.

# 410 Chapter 2. Theoretical Overview

## 411 2.1 The Standard Model

412 The Standard Model of Physics (SM) [47] is currently the most successful formalism to  
413 describe the physical world at a microscopic scale by providing descriptions for all currently  
414 known elementary particles, along with three out of four fundamental forces (electromag-  
415 netism, weak force, strong force) with the exception of gravity. The SM is however not  
416 perfect, and there remains unanswered questions that require development and discovery  
417 of new physics beyond the Standard Model (BSM). This chapter describes an overview of  
418 important components within the SM and relevant BSM aspects for this analysis.

### 419 2.1.1 Elementary particles

420 Elementary particles in the SM can be classified into two groups: bosons consisting  
421 of particles following Bose-Einstein statistics with integer spin, and fermions consisting of  
422 particles following Fermi-Dirac statistics with half-integer spin. Fermions are the building  
423 blocks of composite particles and consequently all known matter, and can be further classified  
424 into quarks & leptons. Bosons act as force mediators for all fundamental forces described by  
425 the SM, and can either be a scalar boson with spin 0 or vector gauge bosons with spin 1. For  
426 each elementary particle, there also exists a corresponding antiparticle with identical mass  
427 and opposite charge (electric or color). Figure 2.1 shows all known elementary particles in  
428 the SM.

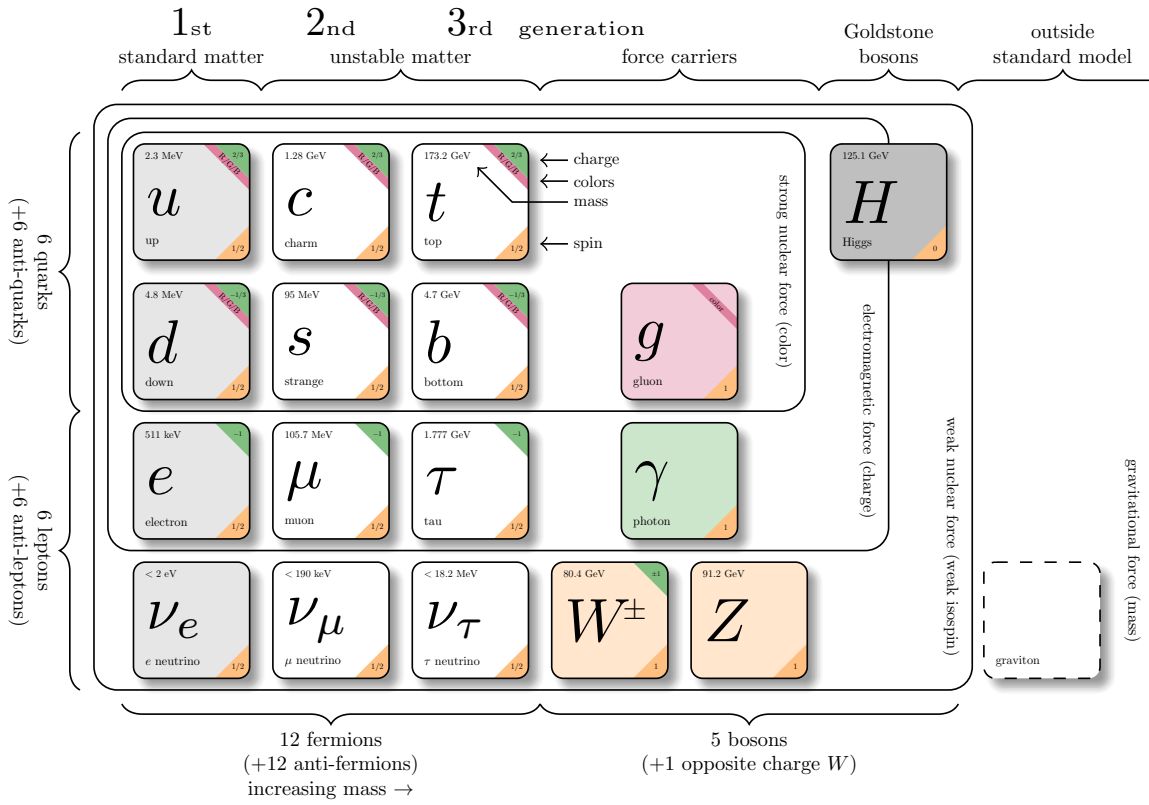


Figure 2.1: Particles within the SM and their properties [48].

## 429 Fermions

430 Fermions consist of quarks and leptons with six flavors each, grouped into three genera-  
 431 tions of doublets. The six quark flavors are up ( $u$ ), down ( $d$ ), charm ( $c$ ), strange ( $s$ ), bottom  
 432 ( $b$ ) and top ( $t$ ), arranged in increasing order of mass. The quark flavors form three doublets  
 433 ( $u, d$ ), ( $c, s$ ) and ( $t, b$ ), with each doublet containing one quark with electric charge of  $+2/3$   
 434 ( $u, s, t$ ), and the other with charge of  $-1/3$  ( $d, c, b$ ). Each quark also possesses a property  
 435 known as color charge, with possible values of red ( $R$ ), green ( $G$ ), blue ( $B$ ) or their corre-  
 436 sponding anticolor ( $\bar{R}, \bar{G}, \bar{B}$ ). Color charge follows color confinement rules, which allows  
 437 only configurations of quarks with total neutral color charge to exist in isolation. Neutral

438 charge configurations can be formed from either a set of three colors ( $R, G, B$ ), a set of a  
439 color and its anticolor, or any combination of the two. Consequently, quarks can only exist  
440 in bound states called hadrons and no isolated quark can be found in a vacuum. Quarks are  
441 the only elementary particles in the SM that can interact with all four fundamental forces.

442 The three leptons doublets consist of three charged leptons: electron ( $e$ ), muon ( $\mu$ ), tau  
443 ( $\tau$ ), and their respective neutrino flavors: electron neutrino ( $\nu_e$ ), muon neutrino ( $\nu_\mu$ ), tau  
444 neutrino ( $\nu_\tau$ ). Charged leptons carry an electric charge of  $-1$ , while their antiparticles carry  
445 the opposite charge ( $+1$ ) and their corresponding neutrino flavors carry no charge. Charged  
446 leptons interact with all fundamental forces except the strong force, while neutrinos only  
447 interact with the weak force and gravity.

## 448 Bosons

449 The SM classifies bosons into two types: one scalar boson with spin 0 known as the  
450 Higgs ( $H$ ) boson, and vector gauge bosons with spin 1 known as gluons ( $g$ ), photon ( $\gamma$ ),  
451  $W^\pm$  and  $Z$  bosons. Gluons and photon are massless, while the  $W^\pm$ ,  $Z$  and  $H$  bosons are  
452 massive. Each vector gauge boson serves as the mediator for a fundamental force described  
453 by the SM. Gluons are massless particles mediating the strong interaction by carrying color  
454 charges between quarks following quantum chromodynamics (QCD). Each gluon carries a  
455 non-neutral color charge out of eight linearly independent color states in the gluon color  
456 octet [49]. The photon ([citation](#)) is the massless and charge-neutral mediator particle for  
457 the electromagnetic interaction following quantum electrodynamics (QED). The  $W^\pm$  and  
458  $Z$  bosons ([citation](#)) are massive mediator particles for the weak interaction, with the  $W^\pm$   
459 boson carrying an electric charge of  $\pm 1$  while the  $Z$  boson is charge neutral.

460 Other than the vector gauge boson, the only scalar boson in the SM is the massive and

461 charge neutral Higgs boson ([citation](#)). The Higgs boson does not mediate any fundamental  
 462 force like vector bosons, but serve to provide the rest mass for all massive elementary particles  
 463 in the SM through the Higgs mechanism described in section 2.1.2.3.

464 **Top quark**

465 As of now, the top quark ( $t$ ) is the heaviest particle in the SM with mass of about 173 GeV  
 466 [[50](#)], approaching the EW symmetry breaking scale. Its high mass gives the top quark the  
 467 strongest Yukawa coupling to the Higgs boson ( $y_t \approx 1$ ) [[24](#)] and exotic resonances in many  
 468 proposed BSM models [[51–54](#)], making the top quark and its processes attractive vehicles  
 469 with which to probe new physics.

470 Due to its mass, the top quark has a

471 very short lifetime of  $10^{-24}$  s [[22](#)] and de-  
 472 cays before it can hadronize following color  
 473 confinement. The top quark decays to a  $W$   
 474 boson and a  $b$ -quark with a branching ratio  
 475 of almost 100%. The  $W$  boson can subse-  
 476 quently decay to a quark-antiquark pair or  
 477 to a lepton-neutrino pair (Figure 2.2), with  
 478 branching ratios of approximately 68% and  
 479 32% respectively. All lepton flavors have  
 480 similar branching ratios during a leptonic  $W$   
 481 decay, assuming lepton universality.

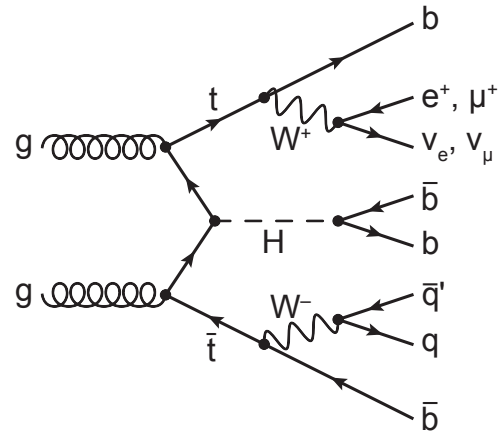


Figure 2.2: Feynman diagram for  $t\bar{t}$  production and subsequent decay processes [[55](#)]. Top quark decays into a  $W$ -boson and  $b$ -quarks, and  $W$ -boson can decay to a  $q\bar{q}$  or a  $\ell\nu_\ell$  pair.

## 482 2.1.2 Mathematical formalism

483 The SM can be described within the formalism of quantum field theory (QFT) with the  
484 Lagrangian [56]

$$\mathcal{L}_{\text{SM}} = \mathcal{L}_{\text{QCD}} + \underbrace{(\mathcal{L}_{\text{gauge}} + \mathcal{L}_{\text{fermion}} + \mathcal{L}_{\text{Higgs}} + \mathcal{L}_{\text{Yukawa}})}_{\mathcal{L}_{\text{EW}}} \quad (2.1)$$

485 where  $\mathcal{L}_{\text{QCD}}$  is the QCD term and  $\mathcal{L}_{\text{EW}}$  is the electroweak (EW) term of the Lagrangian.  
486 Formalism of QFT within the SM treats particles as excitations [57] of their corresponding  
487 quantum fields i.e. fermion field  $\psi$ , electroweak boson fields  $W_{1,2,3}$  &  $B$ , gluon fields  $G_\alpha$  and  
488 Higgs field  $\phi$ .

489 The foundation of modern QFT involves gauge theory. A quantum field has gauge sym-  
490 metry if there exists a continuous gauge transformation that when applied to every point in  
491 a field (local gauge transformation) leaves the field Lagrangian unchanged. The set of gauge  
492 transformations of a gauge symmetry is the symmetry group of the field which comes with  
493 a set of generators, each with a corresponding gauge field. Under QFT, the quanta of these  
494 gauge fields are called gauge bosons.

495 The SM Lagrangian is gauge invariant under global Poincaré symmetry and local  $SU(3)_C \times$   
496  $SU(2)_L \times U(1)_Y$  gauge symmetry, with the  $SU(3)_C$  symmetry group corresponding to the  
497 strong interaction and  $SU(2)_L \times U(1)_Y$  to the EW interaction. Global Poincaré symmetry  
498 ensures that  $\mathcal{L}_{\text{SM}}$  satisfies translational symmetry, rotational symmetry and Lorentz boost  
499 frame invariance [58]. These symmetries give rise to corresponding conservation laws, which  
500 lead to conservation of momentum, angular momentum and energy in the SM as a result of  
501 Noether's theorem [59].

502    **2.1.2.1    Quantum chromodynamics**

503    Quantum chromodynamics is a non-Abelian gauge theory i.e. Yang-Mills theory [6, 7]  
 504    describing the strong interaction between quarks in the SM with the gauge group  $SU(3)_C$ ,  
 505    where  $C$  represents conservation of color charge under  $SU(3)_C$  symmetry. According to  
 506    QFT, quarks can be treated as excitations of the corresponding quark fields  $\psi$ . The free Dirac  
 507    Lagrangian for the quark fields  $\mathcal{L}_0 = \bar{\psi}(i\gamma^\mu\partial_\mu - m)\psi$  is invariant under global  $SU(3)$  sym-  
 508    metry, but not under local  $SU(3)_C$  symmetry. To establish invariance under local  $SU(3)_C$   
 509    symmetry, the gauge covariant derivative  $D_\mu$  is defined so that

$$D_\mu\psi = (\partial_\mu - ig_s G_\mu^a T_a)\psi, \quad (2.2)$$

510    where  $g_s = \sqrt{4\pi\alpha_s}$  is the QCD coupling constant,  $G_\mu^a(x)$  are the eight gluon fields, and  
 511     $T_a$  are generators of  $SU(3)_C$ , represented as  $T_a = \lambda_a/2$  with  $\lambda_a$  being the eight Gell-Mann  
 512    matrices [49]. Let the gluon field strength tensors  $G_{\mu\nu}^a$  be

$$G_{\mu\nu}^a \equiv \partial_\mu G_\nu^a - \partial_\nu G_\mu^a - g_s f^{abc} G_\mu^b G_\nu^c, \quad (2.3)$$

513    where  $f^{abc}$  are the structure constants of  $SU(3)_C$ . The gauge invariant QCD Lagrangian  
 514    can then be written as

$$\begin{aligned} \mathcal{L}_{\text{QCD}} &= \bar{\psi}(i\gamma^\mu D_\mu - m)\psi - \frac{1}{4}G_{\mu\nu}^a G_a^{\mu\nu} \\ &= \underbrace{-\frac{1}{4}G_{\mu\nu}^a G_a^{\mu\nu}}_{\text{gluon kinematics}} + \underbrace{\bar{\psi}(i\gamma^\mu\partial_\mu - m)\psi}_{\text{quark kinematics}} + \underbrace{\bar{\psi}^i(g_s\gamma^\mu(T_a)_{ij}G_\mu^a)\bar{\psi}^j}_{\text{quark-gluon interaction}} \end{aligned} \quad (2.4)$$

<sub>515</sub> where  $i, j$  are color indices with integer values from 1 to 3. Gluons are forced to be massless  
<sub>516</sub> from the lack of a gluon mass term to maintain gauge invariance for the Lagrangian.

### <sub>517</sub> 2.1.2.2 Electroweak theory

<sub>518</sub> The electroweak interaction is the unified description of the weak interaction and electro-  
<sub>519</sub> magnetism under the  $SU(2)_L \times U(1)_Y$  symmetry group, where  $L$  represents the left-handed  
<sub>520</sub> chirality of the weak interaction and  $Y$  represents the weak hypercharge quantum number.  
<sub>521</sub> Fermions can have either left-handed or right-handed chirality with the exception of neutrili-  
<sub>522</sub> nos which can only have left-handed chirality in the SM, and can be divided into left-handed  
<sub>523</sub> doublets and right-handed singlets

$$\psi_L = \begin{pmatrix} \nu_e \\ e_L \end{pmatrix}, \begin{pmatrix} \nu_\mu \\ \mu_L \end{pmatrix}, \begin{pmatrix} \nu_\tau \\ \tau_L \end{pmatrix}, \begin{pmatrix} u_L \\ d_L \end{pmatrix}, \begin{pmatrix} c_L \\ s_L \end{pmatrix}, \begin{pmatrix} t_L \\ b_L \end{pmatrix} \quad (2.5)$$

$$\psi_R = e_R, \mu_R, \tau_R, u_R, d_R, c_R, s_R, t_R, b_R.$$

<sub>524</sub> where  $g'$  is the  $B_\mu$  coupling constant and  $B_\mu(x)$  is a vector gauge field that transforms under  
<sub>525</sub>  $U(1)_Y$  as

$$B_\mu \rightarrow B_\mu + \frac{1}{g'} \partial_\mu \theta(x). \quad (2.6)$$

<sub>526</sub> Right-handed fermion singlets are not affected by  $SU(2)_L$  transformation, so the fermion  
<sub>527</sub> fields  $\psi$  transform under  $SU(2)_L$  as

$$\psi_L \rightarrow e^{iI_3\vec{\theta}(x)\cdot\vec{\sigma}/2}\psi_L \quad (2.7)$$

$$\psi_R \rightarrow \psi_R.$$

<sub>528</sub> where  $\vec{\sigma}/2$  are generators of  $SU(2)_L$  with  $\vec{\sigma}$  being the Pauli matrices. In order to preserve  
<sub>529</sub> local symmetry, the gauge covariant derivative for  $SU(2)_L$  and  $U(1)_Y$  can be defined [60] so

<sup>530</sup> that the gauge covariant derivative for  $SU(2)_L \times U(1)_Y$  can be written as

$$\begin{aligned} D_\mu \psi_L &= \left( \partial_\mu - ig' \frac{Y_L}{2} B_\mu - ig \frac{\sigma_i}{2} W_\mu^i \right) \psi_L \\ D_\mu \psi_R &= \left( \partial_\mu - ig' \frac{Y_R}{2} B_\mu \right) \psi_R. \end{aligned} \quad (2.8)$$

<sup>531</sup> where  $B_\mu(x)$  is a vector gauge field associated with  $U(1)_Y$  and  $W_\mu^i(x)$  ( $i = 1, 2, 3$ ) are three  
<sup>532</sup> vector gauge fields associated with  $SU(2)_L$ . The  $B_\mu$  and  $W_\mu^i$  gauge fields transform under  
<sup>533</sup> their corresponding symmetry groups  $U(1)_Y$  and  $SU(2)_L$  as

$$\begin{aligned} B_\mu &\rightarrow B_\mu + \frac{1}{g'} \partial_\mu \theta(x) \\ W_\mu^i &\rightarrow W_\mu^i + \frac{2}{g} \partial_\mu \theta_a(x) + \epsilon^{ijk} \theta_j(x) W_\mu^k, \end{aligned} \quad (2.9)$$

<sup>534</sup> where  $g'$  is the  $B_\mu$  gauge coupling constant,  $g$  is the  $W_\mu^i$  gauge coupling constants and  $\epsilon^{ijk}$   
<sup>535</sup> is the  $SU(2)_L$  structure constant. Similar to section 2.1.2.1, the kinetic term is added by  
<sup>536</sup> defining field strengths for the four gauge fields

$$\begin{aligned} B_{\mu\nu} &\equiv \partial_\mu B_\nu - \partial_\nu B_\mu \\ W_{\mu\nu}^i &\equiv \partial_\mu W_\nu^i - \partial_\nu W_\mu^i - g e^{ijk} W_\mu^j W_\nu^k. \end{aligned} \quad (2.10)$$

<sup>537</sup> The local  $SU(2)_L \times U(1)_Y$  invariant EW Lagrangian [60] is then

$$\begin{aligned} \mathcal{L}_{\text{EW}} &= i\bar{\psi}(\gamma^\mu D_\mu)\psi - \frac{1}{4}W_{\mu\nu}^i W_i^{\mu\nu} - \frac{1}{4}B_{\mu\nu} B^{\mu\nu} \\ &= \underbrace{i\bar{\psi}(\gamma^\mu \partial_\mu)\psi}_{\text{fermion kinematics}} - \underbrace{\bar{\psi}\left(\gamma^\mu g' \frac{Y}{2} B_\mu\right)\psi}_{\text{fermion-gauge boson interaction}} - \underbrace{\bar{\psi}_L\left(\gamma^\mu g \frac{\sigma_i}{2} W_\mu^i\right)\psi_L}_{\text{boson kinematics \& self-interaction}} - \underbrace{\frac{1}{4}W_{\mu\nu}^i W_i^{\mu\nu} - \frac{1}{4}B_{\mu\nu} B^{\mu\nu}}_{\text{boson kinematics \& self-interaction}}. \end{aligned} \quad (2.11)$$

538 Under  $\approx 159.5$  GeV, the EW symmetry  $SU(2)_L \times U(1)_Y$  undergoes spontaneous symmetry  
 539 breaking [61] into  $U(1)_{\text{QED}}$  symmetry, which corresponds to a separation of the weak and  
 540 electrodynamic forces. Electroweak spontaneous symmetry breaking replaces the four mass-  
 541 less and similarly-behaved EW gauge bosons  $B_\mu$  and  $W_\mu^i$  with the EM boson  $\gamma$  and the weak  
 542 bosons  $Z/W^\pm$ , as well as giving the  $Z$  and  $W^\pm$  bosons masses via the Higgs mechanism.  
 543 This is due to a specific choice of gauge for the Higgs field leading to the reparameterization  
 544 of the EW bosons  $B_\mu$  and  $W_\mu^i$  to  $W^\pm/Z/\gamma$  using the relations

$$\begin{aligned}
 W_\mu^\pm &\equiv \frac{1}{\sqrt{2}} (W_\mu^1 \mp iW_\mu^2) \\
 \begin{pmatrix} A_\mu \\ Z_\mu \end{pmatrix} &\equiv \begin{pmatrix} \cos \theta_W & \sin \theta_W \\ -\sin \theta_W & \cos \theta_W \end{pmatrix} \begin{pmatrix} B_\mu \\ W_\mu^3 \end{pmatrix}
 \end{aligned} \tag{2.12}$$

545 where  $\theta_W \equiv \cos^{-1} (g/\sqrt{g^2 + g'^2})$  is the weak mixing angle. The boson kinetic term can also  
 546 be refactorized to extract cubic (three vertices) and quartic (four vertices) self-interactions  
 547 among the gauge bosons [60]. The Lagrangian can then be rewritten as

$$\begin{aligned}
 \mathcal{L} = & \underbrace{eA_\mu \bar{\psi} (\gamma^\mu Q) \psi}_{\text{electromagnetism}} + \underbrace{\frac{e}{2\sin \theta_W \cos \theta_W} \bar{\psi} \gamma^\mu (v_f - a_f \gamma_5) \psi Z_\mu}_{\text{neutral current interaction}} \\
 & + \underbrace{\frac{g}{2\sqrt{2}} \sum_{\psi_L} [\bar{f}_2 \gamma^\mu (1 - \gamma_5) f_1 W_\mu^+ + \bar{f}_1 \gamma^\mu (1 - \gamma_5) f_2 W_\mu^-]}_{\text{charged current interaction}} \\
 & + \underbrace{\mathcal{L}_{\text{kinetic}} + \mathcal{L}_{\text{cubic}} + \mathcal{L}_{\text{quartic}}}_{\text{boson self-interaction}}
 \end{aligned} \tag{2.13}$$

548 where  $\gamma_5 = i\gamma^0\gamma^1\gamma^2\gamma^3$  is the chirality projection operator,  $a_f = I_3$ ,  $v_f = I_3(1 - 4|Q| \sin^2 \theta_W)$   
 549 and  $f_1, f_2$  are up and down type fermions of a left-handed doublet.

550    **2.1.2.3 Higgs mechanism**

551    So far, the EW bosons are massless since the mass terms  $-m\bar{\psi}\psi$  for fermions and  
 552     $-mA^\mu A_\mu$  for bosons are not invariant under the EW Lagrangian symmetries. The parti-  
 553    cles must then acquire mass under another mechanism. The Brout-Engler-Higgs mechanism  
 554    [11–13] was introduced in 1964 to rectify this issue and verified in 2012 with the discovery  
 555    of the Higgs boson [20, 21].

556    The Higgs potential is expressed as

$$V(\phi^\dagger \phi) = \mu^2 \phi^\dagger \phi + \lambda (\phi^\dagger \phi)^2 \quad (2.14)$$

557    where  $\mu^2$  and  $\lambda > 0$  are arbitrary parameters, and the  $SU(2)_L$  doublet  $\phi = \begin{pmatrix} \phi^+ \\ \phi^0 \end{pmatrix}$  is the Higgs  
 558    field with complex scalar fields  $\phi^+$  and  $\phi^0$  carrying +1 and 0 electric charge respectively.

559    The Lagrangian for the scalar Higgs field is

$$\mathcal{L}_H = (\partial_\mu \phi)^\dagger (\partial^\mu \phi) - V(\phi^\dagger \phi). \quad (2.15)$$

560    Since the potential  $V(\phi^\dagger \phi)$  is constrained by  $\lambda > 0$ , the ground state is solely controlled by  
 561     $\mu$ . If  $\mu^2 > 0$ , the ground state energy is  $\phi = 0$ , and the EW bosons would remain massless.  
 562    If  $\mu^2 < 0$ , the ground state is

$$|\phi|^2 = -\frac{\mu^2}{2\lambda} \equiv \frac{v^2}{\sqrt{2}}, \quad (2.16)$$

563    where  $v$  is defined as the vacuum expectation value (VEV). The standard ground state for  
 564    the Higgs potential without loss of generality can be chosen as  $\phi(0) = 1/\sqrt{2}(0)_v$ .

565    Having  $U(1)$  symmetry allows any  $-e^{i\theta} \sqrt{\mu^2/\lambda}$  to be a ground state energy for the Higgs

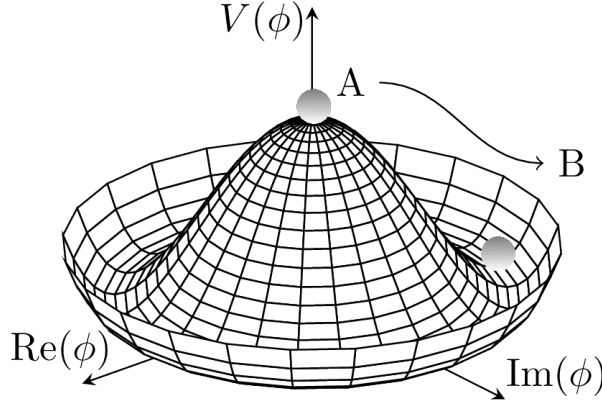


Figure 2.3: Illustration of a common representation of the Higgs potential [62]. Before SSB, the ground state  $\phi(0)$  is located at A which is symmetric with respect to the potential. A perturbation to this state fixes the ground state energy  $|\phi(0)|^2$  to a particular value at B, "spontaneously" breaking the symmetry and degeneracy in  $|\phi(0)|^2$ .

566 Lagrangian. This degeneracy results in spontaneous symmetry breaking of the  $SU(2)_L \times$   
 567  $U(1)_Y$  symmetry into  $U(1)_{\text{EM}}$  symmetry when the Higgs field settles on a specific vacuum  
 568 state as a result of a perturbation or excitation (Figure 2.3). The spontaneous symmetry  
 569 breaking introduces three massless (Nambu-Goldstone [63]) vector gauge boson  $\xi$  and a  
 570 massive scalar boson  $\eta$ , each corresponds to a generator of the gauge group. The vector field  
 571 for  $\xi$  and  $\eta$  are real fields parameterized as  $\xi \equiv \phi^+ \sqrt{2}$  and  $\eta \equiv \phi^0 \sqrt{2} - v$  [64]. The Higgs  
 572 field now becomes

$$\phi = \frac{v + \eta + i\xi}{\sqrt{2}} = \frac{1}{\sqrt{2}} e^{i\xi} \begin{pmatrix} 0 \\ v + \eta \end{pmatrix}. \quad (2.17)$$

573 Due to  $U(1)_{\text{EM}}$  invariance, a unitary gauge with the transformation  $\phi \rightarrow \exp(-i\xi \cdot) \frac{\sigma}{2v}$  can  
 574 be chosen for the Higgs field to eliminate the massless bosons and incorporate them into the  
 575 EM/weak bosons via Equation 2.12. This leaves the massive  $\eta$  which can now be observed as  
 576 an excitation of the Higgs field from the standard ground state and must be the Higgs boson  
 577  $h$ . Using the EW covariant derivative from Equation 2.8, the Higgs Lagrangian around the

578 vacuum state becomes

$$\begin{aligned}\mathcal{L}_H &= (D_\mu \phi)^\dagger (D^\mu \phi) - \mu^2 \left( \frac{v+h}{\sqrt{2}} \right)^2 - \lambda \left( \frac{v+h}{\sqrt{2}} \right)^4 \\ &= (D_\mu \phi)^\dagger (D^\mu \phi) - \frac{1}{2} \mu^2 h^2 - \lambda v h^3 - \frac{\lambda}{4} h^4 - \dots\end{aligned}\tag{2.18}$$

579 The Higgs mass can be extracted from the quadratic term as  $m_H = \sqrt{-2\mu^2}$ . The kinetic

580 term in the Lagrangian can be written as

$$\begin{aligned}(D_\mu \phi)^\dagger (D^\mu \phi) &= \frac{1}{2} (\partial_\mu h)^2 + \frac{g^2}{8} (v+h)^2 \left| W_\mu^1 - i W_\mu^2 \right|^2 + \frac{1}{8} (v+h)^2 (g' W_\mu - g B_\mu) \\ &= \frac{1}{2} (\partial_\mu h)^2 + (v+h)^2 \left( \frac{g^2}{4} W_\mu^+ W^{-\mu} + \frac{1}{8} (g^2 + g'^2) Z_\mu^0 Z^{0\mu} \right).\end{aligned}\tag{2.19}$$

581 Masses for the EW bosons can be extracted from the quadratic terms

$$m_{W^\pm} = \frac{v}{2} g, \quad m_Z = \frac{v}{2} \sqrt{g^2 + g'^2}, \quad m_\gamma = 0.\tag{2.20}$$

582 However, the fermion mass term  $-m\bar{\psi}\psi$  still breaks EW invariance after spontaneous sym-  
583 metry breaking. Instead, fermions acquire mass by replacing the mass term with a gauge  
584 invariant Yukawa term in the EW Lagrangian representing fermions' interactions with the  
585 Higgs field [64]

$$\begin{aligned}\mathcal{L}_{\text{Yukawa}} &= -c_f \frac{v+h}{\sqrt{2}} (\bar{\psi}_R \psi_L + \bar{\psi}_L \psi_R) \\ &= -\underbrace{\frac{c_f}{\sqrt{2}} v (\bar{\psi} \psi)}_{\text{fermion mass}} - \underbrace{\frac{c_f}{\sqrt{2}} (h \bar{\psi} \psi)}_{\text{fermion-Higgs interaction}},\end{aligned}\tag{2.21}$$

586 where  $c_f$  is the fermion-Higgs Yukawa coupling. The fermion mass is then  $m_f = c_f v / \sqrt{2}$ .

587 **2.2 Beyond the Standard Model**

588 **2.2.1 Top-philic vector resonance**

589 Many BSM models extend the SM by adding to the SM gauge group additional  $U(1)'$   
590 gauge symmetries [65, 66], each with an associated vector gauge boson nominally called  $Z'$ .  
591 In the case of a BSM global symmetry group with rank larger than the SM gauge group, the  
592 symmetry group can spontaneously break into  $G_{\text{SM}} \times U(1)'^n$ , where  $G_{\text{SM}}$  is the SM gauge  
593 group  $SU(3)_C \times SU(2)_L \times U(1)_Y$  and  $U(1)'^n$  is any  $n \geq 1$  number of  $U(1)'$  symmetries. The  
594 existence of additional vector bosons  $Z'$  would open up many avenues of new physics e.g.  
595 extended Higgs sectors from  $U(1)'$  symmetry breaking [67, 68], existence of flavor-changing  
596 neutral current (FCNC) mediated by  $Z'$  [69], and possible exotic production from heavy  $Z'$   
597 decays [70].

598 Due to the top quark having the largest mass out of all known elementary particles in  
599 the SM, many BSM models [38–43, 71, 72] predict ‘top-philic’ vector resonances that have  
600 much stronger coupling to the top quark compared to other quarks. The analysis in this  
601 dissertation attempts to reconstruct a top-philic  $Z'$  resonance directly to avoid dependency  
602 on model choice. Previous model-independent BSM  $t\bar{t}t\bar{t}$  search for top-philic resonances [28]  
603 in the single-lepton final state and similar mass ranges set upper limits on observed (expected)  
604  $Z'$  production cross section between 21 (14) fb to 119 (86) fb depending on parameter choice.  
605 This analysis is also motivated by the recent observation of SM  $t\bar{t}t\bar{t}$  production in the same-  
606 sign multilepton (SSML) channel by ATLAS [44] and CMS [73] at  $6.1\sigma$  and  $5.6\sigma$  discovery  
607 significance respectively.

608 A simplified color-singlet vector particle model [45, 71] is employed to study model-

dependent interpretations. The interaction Lagrangian assumes only  $Z'$  to top coupling and has the form

$$\begin{aligned}\mathcal{L}_{Z'} &= \bar{t}\gamma_\mu (c_L P_L + c_R P_R) t Z'^\mu \\ &= c_t \bar{t}\gamma_\mu (\cos \theta P_L + \sin \theta P_R) t Z'^\mu,\end{aligned}\tag{2.22}$$

where  $c_t = \sqrt{c_L^2 + c_R^2}$  is the  $Z'$ -top coupling strength,  $P_{L/R} = (1 \mp \gamma_5)/2$  are the chirality projection operators, and  $\theta = \tan^{-1}(c_R/c_L)$  is the chirality mixing angle. Expanding the Lagrangian results in

$$\mathcal{L}_{Z'} = \frac{1}{\sqrt{2}} \bar{t}\gamma_\mu \left[ \sin \left( \theta + \frac{\pi}{4} \right) - \left( \sqrt{2} \cos \left( \theta + \frac{\pi}{4} \right) \right) \gamma_5 \right] t Z'^\mu,\tag{2.23}$$

which bears striking resemblance to the EW Lagrangian neutral current interaction term in Equation 2.13, showing the similarity between the  $Z'$  and the  $Z$  boson that acquires mass from  $SU(2)_L \times U(1)_Y$  spontaneous symmetry breaking. Assuming the  $Z'$  mass  $m_{Z'}$  is much larger than the top mass ( $m_t^2/m_{Z'}^2 \approx 0$ ), the  $Z'$  decay width at leading-order (LO) can be approximated as

$$\Gamma(Z' \rightarrow t\bar{t}) \approx \frac{c_t^2 m_{Z'}}{8\pi}.\tag{2.24}$$

It can be observed that  $\Gamma/m_{Z'} \approx c_t^2/8\pi \ll 1$  for  $c_t \approx 1$ , which suggests a very narrow and well-defined resonance peak. This validates the narrow-width approximation for the choice of  $c_t = 1$  and supports efforts to directly reconstruct the resonance.

The main production channels for the aforementioned heavy topophilic color singlet  $Z'$  are at tree level and loop level, with the one-loop level being the dominant processes [45]. Loop level processes are dependent on the chirality angle  $\theta$ , where  $\theta = \pi/4$  suppresses all but gluon-initiated box sub-processes. To minimize model dependence, only the tree level

626 production was considered for this analysis by choosing  $\theta = \pi/4$ . Figure 2.4 illustrates  
 627 several tree level  $Z'$  production processes.

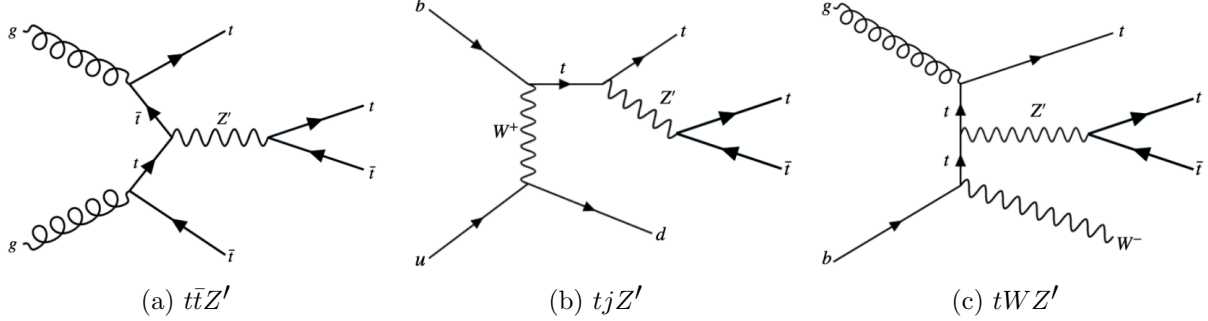


Figure 2.4: Feynman diagrams for tree level  $Z'$  production in association with (a)  $t\bar{t}$ , (b)  $tj$  (light quark) and (c)  $tW$ , decaying to final states containing (a)  $t\bar{t}\bar{t}\bar{t}$  or (b)(c)  $t\bar{t}t\bar{t}$  [45].

628 The single-top-associated channels  $tjZ'$  and  $tWZ'$  are suppressed by three-body phase  
 629 space [45], resulting in smaller cross sections by a factor of two compared to the  $t\bar{t}$ -associated  
 630 process  $t\bar{t}Z'$ . Unlike  $tjZ'$  and  $tWZ'$  which are produced via EW and mixed QCD-EW  
 631 interactions respectively,  $t\bar{t}t\bar{t}$  production is governed by the strong interaction which can  
 632 overpower phase space suppression. Additionally,  $t\bar{t}t\bar{t}$  production is independent of  $\theta$  while  
 633  $tjZ'$  and  $tWZ'$  are minimally suppressed under pure left-handed interactions ( $\theta = 0$ ) and  
 634 maximally suppressed under pure right-handed interactions ( $\theta = \pi/2$ ).

### 635 2.2.2 BSM $t\bar{t}Z' \rightarrow t\bar{t}t\bar{t}$

636 This analysis uses the  $t\bar{t}t\bar{t}$  final state signal signature to search for the existence of a heavy  
 637 BSM resonance that couples strongly to the top quark. Cross section for  $t\bar{t}t\bar{t}$  production  
 638 can be enhanced by many possible BSM models, in particular production of heavy scalars  
 639 and pseudoscalar bosons predicted in Type-II two-Higgs-doublet models (2HDM) [39–43] or  
 640 possible production of a heavy neutral resonance boson  $Z'(\rightarrow t\bar{t})$  in association with a  $t\bar{t}$   
 641 pair [74, 75]. The  $t\bar{t}Z'$  production mode and consequently  $t\bar{t}t\bar{t}$  signal signature can provide

642 a more sensitive channel for searches by avoiding contamination from the large SM  $gg \rightarrow t\bar{t}$   
643 background in an inclusive  $Z' \rightarrow t\bar{t}$  search.

## 644 Decay modes

645 The different  $W$  boson decay modes

646 shown in Figure 2.2 result in many differ-  
647 ent final states for  $t\bar{t}Z'/t\bar{t}t\bar{t}$  decay, which  
648 can each be classified into one of three chan-

649 nels shown in Figure 2.5: all hadronic de-  
650 cays; exactly one lepton or two opposite-sign  
651 leptons (1LOS); exactly two same-sign lep-

652 tons or three or more leptons (SSML). The  
653 branching ratio for each channel is shown  
654 in Figure 2.5. The all hadronic and 1LOS

655 channels have much larger branching ratios  
656 compared to SSML channel but suffer heavily from  $gg \rightarrow t\bar{t}$  background contamination,  
657 giving the SSML channel better sensitivity at the cost of lower statistics. This is also the  
658 targeted channel for this analysis.

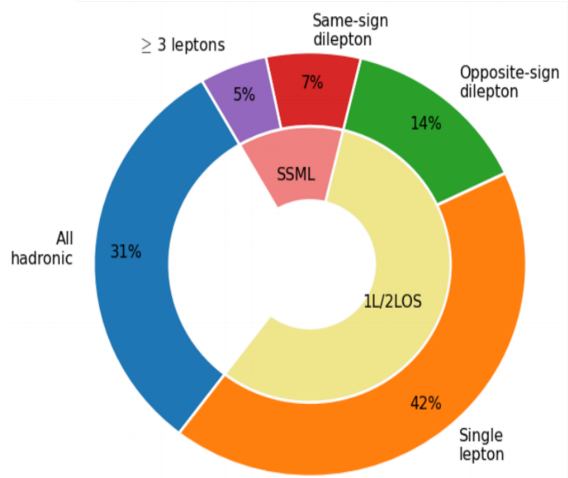


Figure 2.5: Branching ratios for  $t\bar{t}t\bar{t}$  decay [76]. The same-sign dilepton and multilepton chan-  
nels together forms the SSML channel.

# 659 Chapter 3. LHC & ATLAS Experiment

## 660 3.1 The Large Hadron Collider

661 Predictions from theoretical models are evaluated against experimental data collected  
662 from particle detectors. This chapter provides a detailed overview of the Large Hadron  
663 Collider (LHC) and the ATLAS detector, one of the key experiments designed to study  
664 high-energy collisions at the LHC.

### 665 3.1.1 Overview

666 The Large Hadron Collider [77] (LHC) is currently the world's largest particle collider  
667 with a circumference of almost 27 km. Built by CERN on the border of Switzerland and  
668 France, the LHC is designed as a particle collider for proton-proton ( $pp$ ), sometimes heavy  
669 ions i.e. lead-lead (PbPb) and proton-lead ( $pPb$ ) beams at TeV-scale energies. Two beams  
670 of particles are injected into the LHC in opposite directions and allowed to collide at the  
671 center of four major experiments:

- 672 • **A Toroidal LHC ApparatuS** (ATLAS) [27] and **Compact Muon Solenoid** (CMS)  
673 [78]: multi-purpose detectors, designed to target a variety of phenomena including SM,  
674 BSM and heavy-ion physics.
- 675 • **Large Ion Collider Experiment** (ALICE) [79]: specialized detector to record ion  
676 collisions and study heavy-ion physics.
- 677 • **Large Hadron Collider beauty** (LHCb) [80]: detector dedicated to study properties  
678 of  $b$ -quarks and  $b$ -hadrons.

679      Aside from the four major experiments, the LHC also houses smaller experiments e.g.  
 680     AWAKE [81], FASER [82], KATRIN [83], that either share an interaction point with one of  
 681     the above experiments or make use of particle beams pre-LHC injection.

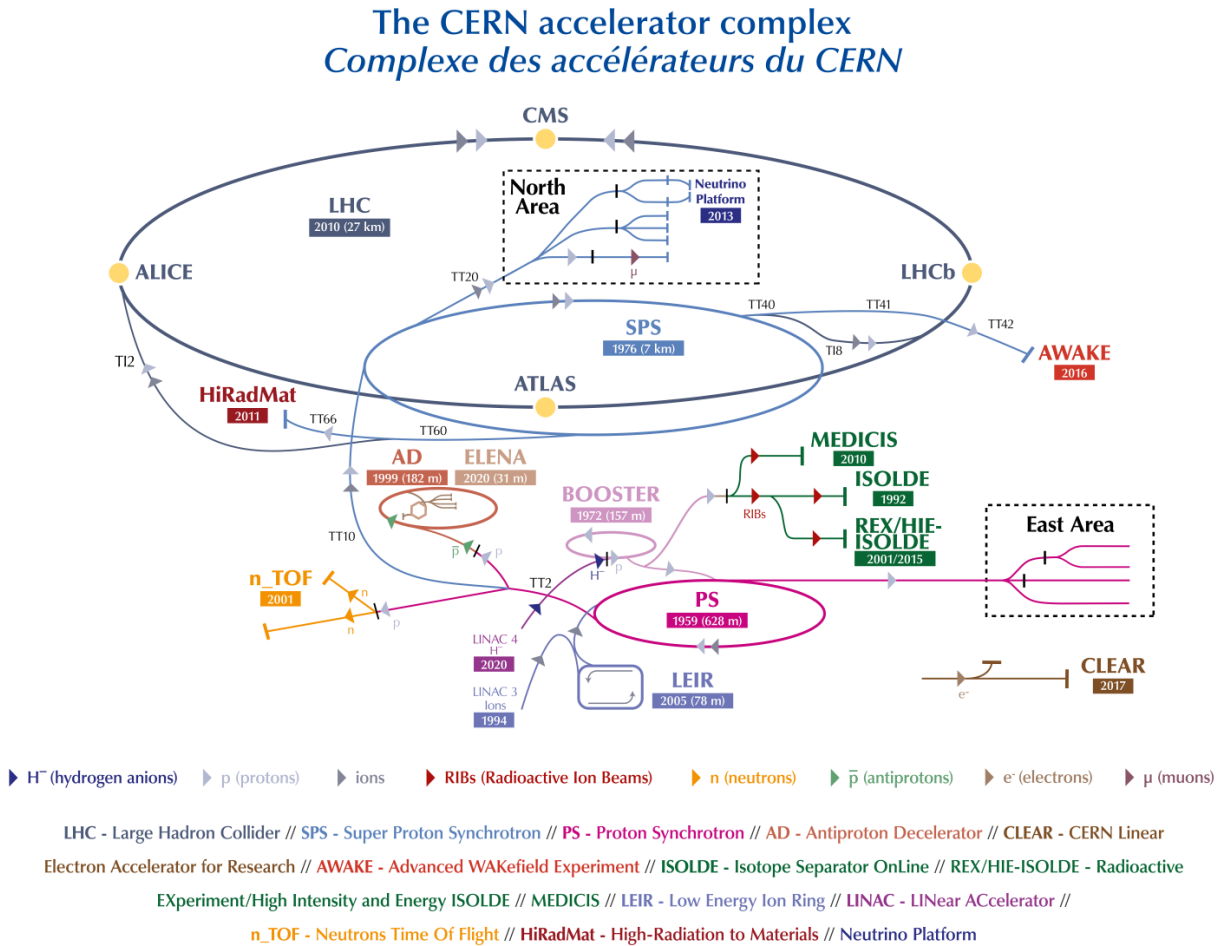


Figure 3.1: The full CERN accelerator complex as of 2022 [84].

682      The majority of the LHC operational time is dedicated to studying  $pp$  collisions of up to  
 683      $\sim 13$  TeV center-of-mass energy, denoted as  $\sqrt{s}$ . Reaching collision energy requires a sequence  
 684     of accelerators within the CERN accelerator complex, shown in Figure 3.1. Proton produc-  
 685     tion starts at LINAC 4, where hydrogen atoms are accelerated to 160 MeV then stripped  
 686     of electrons. The leftover proton beams are injected into the Proton Synchrotron Booster

687 (PSB) and accelerated to 2 GeV before being transferred into the Proton Synchrotron (PS).  
 688 Here, the beams are ramped up to 26 GeV then injected into the Super Proton Synchrotron  
 689 (SPS) to further raise the energy threshold to 450 GeV. The beams are finally injected into  
 690 the LHC in opposite directions, continuously increasing in energy up to 6.5 TeV per beam,  
 691 reaching the 13 TeV center-of-mass energy threshold necessary for collision during Run 2.  
 692 As of the start of Run 3 in 2022, proton beams can now be ramped up to 6.8 TeV per beam  
 693 for a total of  $\sqrt{s} = 13.6$  TeV.

### 694 3.1.2 LHC operations

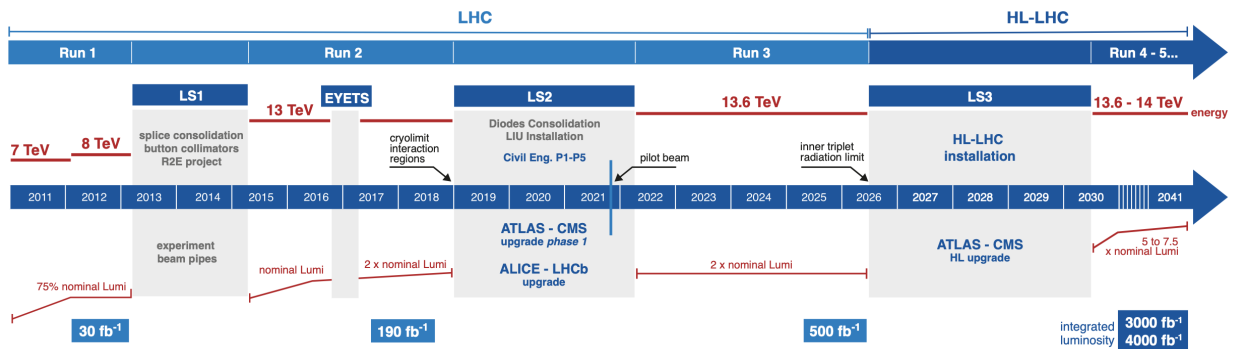


Figure 3.2: Current and future timeline of LHC operations with corresponding center-of-mass energies and projected integrated luminosities. [85].

695 Operations at the LHC are defined in periods of data-taking and shut-down known as  
 696 runs and long shutdowns respectively; the first period (Run 1) started with first collisions  
 697 at the LHC in 2010 at  $\sqrt{s} = 7$  TeV [86]. Upgrades are usually carried out for detectors and  
 698 accelerators during long shutdowns, raising the maximum energy threshold in preparation  
 699 for the next run. An overview of the LHC runtime and corresponding center-of-mass energies  
 700 are summarized in Figure 3.2. During Run 2 from 2015-2018, the ATLAS detector recorded  
 701 a total of  $1.1 \times 10^{16}$   $pp$  collisions at  $\sqrt{s} = 13$  TeV, which corresponds to an integrated

702 luminosity of  $140 \pm 0.83\% \text{ fb}^{-1}$  that passed data quality control and are usable for analyses  
703 [87]. This is also the data set used for the analysis in this dissertation.

### 704 3.1.3 Physics at the LHC

705 The majority of physics studied at the LHC focus primarily on QCD proton-proton hard  
706 scattering processes and the resulting products. Hard scattering processes involve large  
707 momentum transfer compared to the proton mass e.g. top pair production ( $gg \rightarrow t\bar{t}$ ) and  
708 Higgs production ( $gg \rightarrow H$ ), and can be predicted using perturbative QCD [88]. Hard  
709 processes probe distance scales much lower than the proton radius and can be considered  
710 collisions between the constituent quarks and gluons i.e. partons. Soft processes involve  
711 lower momentum transfer between partons and are dominated by less well-understood non-  
712 perturbative QCD effects. The hard interaction between two partons are represented by a  
713 parton distribution function (PDF)  $f_i(x, Q^2)$ , which describes the probability of interacting  
714 with a constituent parton  $i$  that carries a fraction  $x$  of the external hadron's momentum  
715 when probed at a momentum scale of  $Q^2$  [89]. Other partons within the hadron that did  
716 not participate in the collision can still interact via lower momentum underlying-events  
717 (UE). The probability of a particular interaction occurring is defined as its cross-section  
718  $\sigma[b]$ . Figure 3.3 gives an overview of SM processes produced within the LHC and their  
719 cross-sections.

## 720 3.2 The ATLAS detector

721 One of the four main experiments at the LHC is ATLAS [27], designed as a multi-purpose  
722 detector for the role of studying high-energy physics in  $pp$  and heavy-ion collisions. ATLAS

## Standard Model Production Cross Section Measurements

Status: October 2023

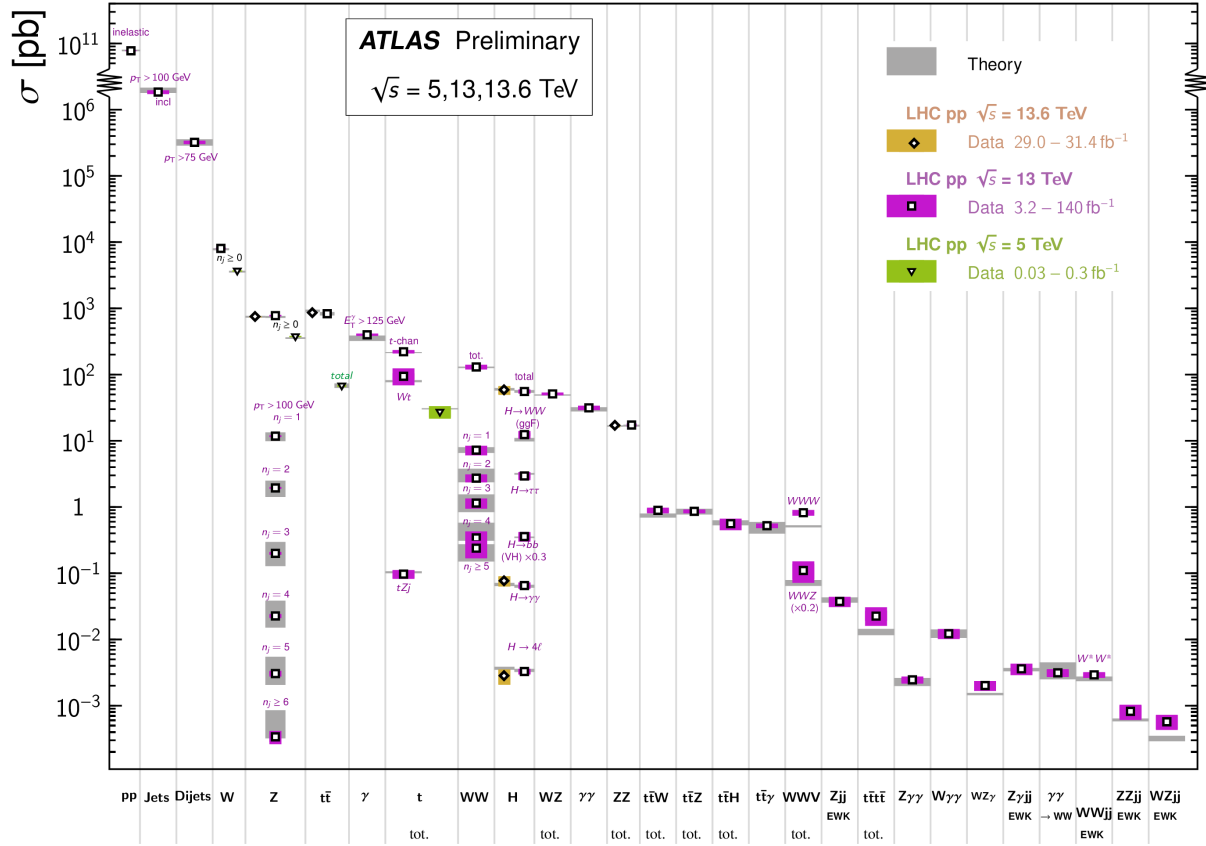


Figure 3.3: Summary of predicted and measured cross-section for SM processes at the LHC at different center-of-mass energies [90].

723 is a detector with symmetric cylindrical geometry with dimensions of 44 m in length and 25  
 724 m in diameter, covering a solid angle of almost  $4\pi$  around the collision point. The detector is  
 725 built concentrically around the beamline with the collision point at the center to maximally  
 726 capture signals produced by interactions. Figure 3.4 shows a slice of the ATLAS detector.  
 727 From the inside out, the main ATLAS subdetector system consists of the inner detector  
 728 (ID), calorimeter systems (electromagnetic and hadronic) and the muon spectrometer (MS).  
 729 The ATLAS detector uses a right-handed coordinate system [27] designed to align with  
 730 the geometry of a collision interaction, with the origin set at the interaction point, the  $z$ -axis

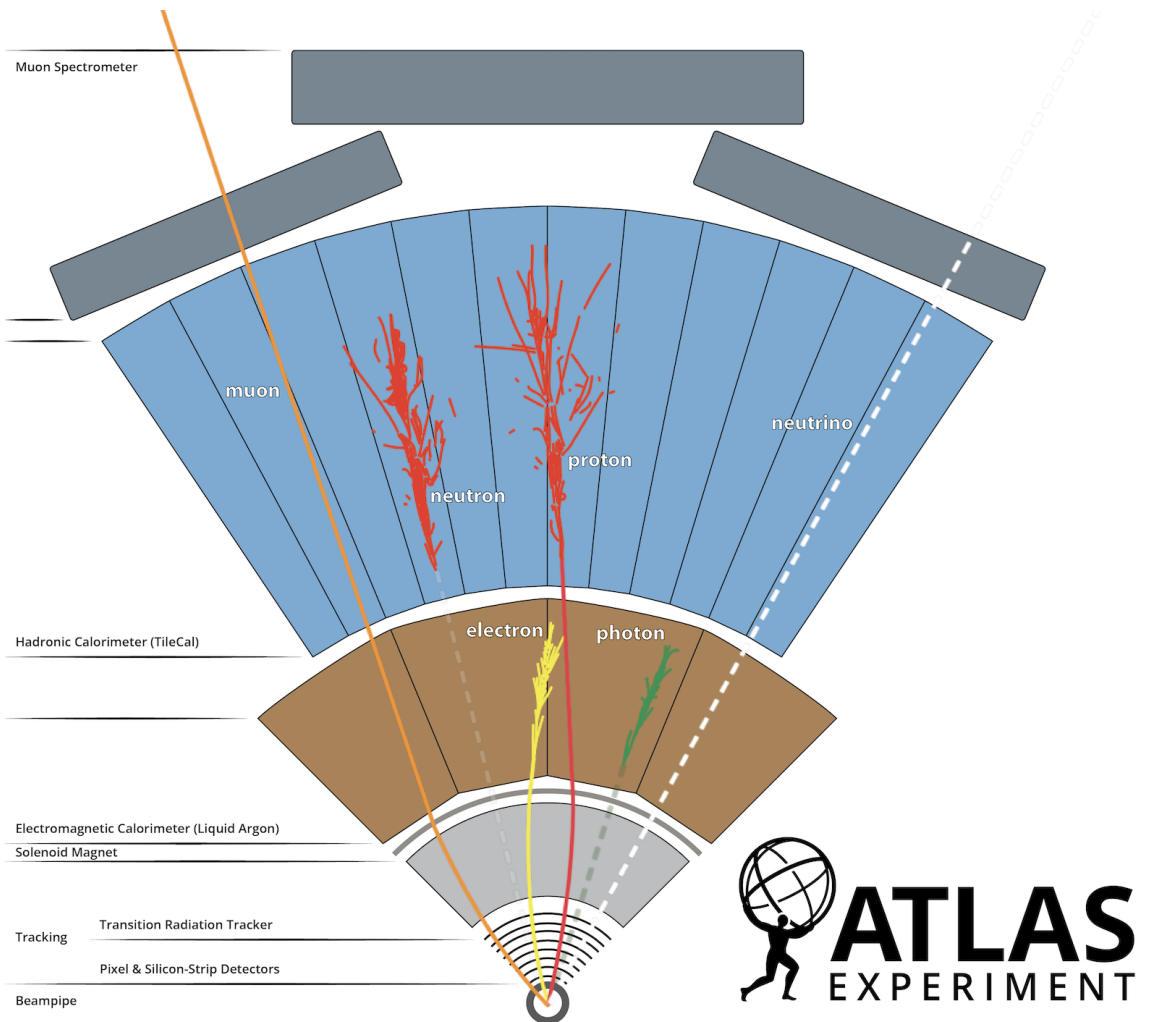


Figure 3.4: A cross section slice of the ATLAS detector showing different subsystems along with visualization of different types of particles traveling through the detector [91].

731 following (either of) the beamline and the  $x$ -axis pointing towards the center of the LHC  
 732 ring. In cylindrical coordinates, the polar angle  $\theta$  is measured from the beam axis, and  
 733 the azimuthal angle  $\phi$  is measured along the transverse plane ( $xy$ -plane) starting at the  $x$ -  
 734 axis. Additional observables are defined for physics purposes: the pseudorapidity defined as  
 735  $\eta = -\ln \tan(\theta/2)$ ; angular distance within the detector defined as  $\Delta R = \sqrt{\Delta\eta^2 + \Delta\phi^2}$ ; and  
 736 transverse momentum  $p_T$  (transverse energy  $E_T$ ) defined as the component of the particle's  
 737 momentum (energy) projected onto the transverse plane.

### 738 3.2.1 Inner detector

739 The innermost part of ATLAS is the inner detector (ID) [27], constructed primarily for  
740 the purpose of measuring and reconstructing charged tracks within the  $|\eta| < 2.5$  region with  
741 high momentum resolution ( $\sigma_{p_T}/p_T = 0.05\% \pm 1\%$ ). Figure 3.5 shows the composition of  
742 the ID with three subsystems, the innermost being the pixel detector, then Semiconductor  
743 Tracker (SCT), and the Transition Radiation Tracker (TRT) on the outermost layer; all of  
744 which are surrounded by a solenoid magnet providing a magnetic field of 2 T.

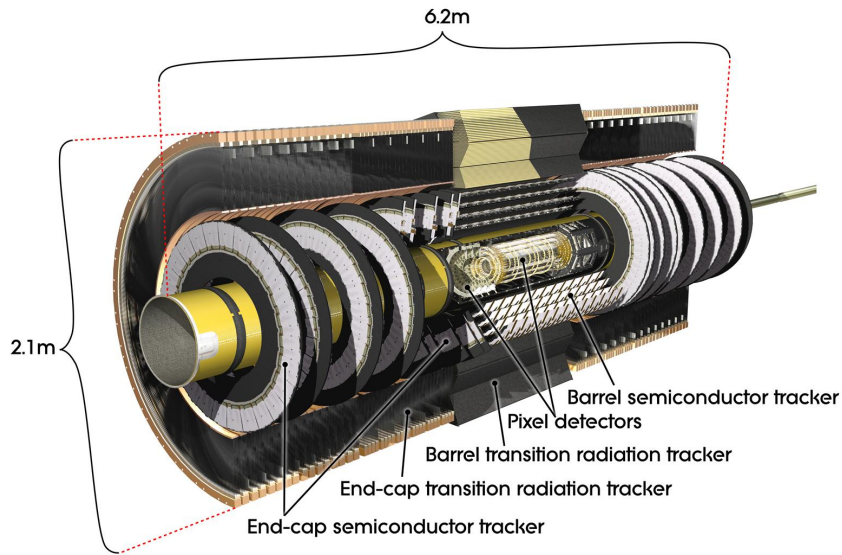


Figure 3.5: Cutaway illustration of the inner detector along with its subsystems [92].

### 745 Pixel detector

746 The pixel detector subsystem [27] consists of 250  $\mu\text{m}$  silicon semiconductor pixel layers  
747 with about 80.4 million readout channels, reaching a spatial resolution of 10  $\mu\text{m}$  in the  
748  $R - \phi$  (transverse) plane and 115  $\mu\text{m}$  in the  $z$ -direction for charged tracks. Charged particles  
749 passing through the pixel detector ionize the silicon layers and produce electron-hole pairs;

750 the electrons drift towards the detector's electrode under an applied electric field and the  
751 resulting electric signals are collected in read-out regions. The pixel detector is used primarily  
752 for impact parameter measurement, pile-up suppression, vertex finding and seeding for track  
753 reconstruction.

#### 754 Semiconductor Tracker

755 The Semiconductor Tracker (SCT) [27] functions similarly to the pixel detector, using  
756 silicon semiconductor microstrips totaling about 6.3 million read-out channels, reaching a  
757 per layer resolution of 17  $\mu\text{m}$  in the  $R\text{-}\phi$  plane and 580  $\mu\text{m}$  in the  $z$ -direction [27]. The  
758 SCT plays an important role in precise  $p_{\text{T}}$  measurement of charged particles as well as track  
759 reconstruction.

#### 760 Transition Radiation Tracker

761 The outermost layer of the ID, the Transition Radiation Tracker (TRT) [27], consists of  
762 layers of 4 mm diameter straw tubes filled with a xenon-based gas mixture and a 30  $\mu\text{m}$   
763 gold-plated wire in the center. The TRT contains a total of about 351 thousand readout  
764 channels with a resolution of 130  $\mu\text{m}$  for each straw tube in the  $R\text{-}\phi$  plane, and provides  
765 extended track measurement, particularly estimation of track curvature under the solenoidal  
766 magnetic field. Importantly, the TRT also serves to identify electrons through absorption of  
767 emitted transition-radiation within the Xe-based gas mixture.

### 768 3.2.2 Calorimeter systems

769 Surrounding the ID is the ATLAS calorimeter system [27] with electromagnetic (EM) and  
770 hadronic calorimeters, covering a range of  $|\eta| < 4.9$ . The calorimeters are sampling calorime-

771 ters with alternating absorbing layers to stop incoming particles and active layers to collect  
 772 read-out signals from energy deposits. Incoming particles passing through the calorimeters  
 773 interact with the absorbing layers, producing EM or hadronic showers of secondary particles.  
 774 The particle showers deposit energy in the corresponding layer of the calorimeters, which  
 775 are collected and aggregated to identify and reconstruct the original particle's energy and  
 776 direction. Figure 3.6 shows a schematic overview of the ATLAS calorimeter system.

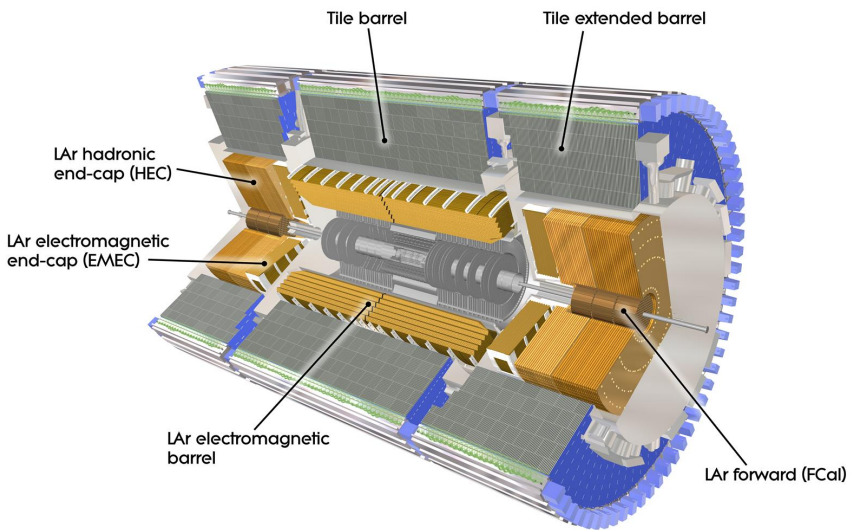


Figure 3.6: Cutaway illustration of the calorimeter system including the EM, hadronic and LAr forward calorimeters [93].

### 777 Electromagnetic calorimeter

778 The EM calorimeter [27] covers the innermost part of the calorimeter system, with lead  
 779 (Pb) absorbing layers and liquid argon (LAr) active layers to capture the majority of electrons  
 780 and photons exiting the ID. The EM calorimeter is divided into regions depending on  $\eta$   
 781 coverage: a barrel region ( $|\eta| < 1.475$ ), two endcap regions ( $1.375 < |\eta| < 3.2$ ) and a  
 782 transition region ( $1.372 < |\eta| < 1.52$ ). The endcap calorimeters are further divided into an

783 outer wheel region ( $1.372 < |\eta| < 2.5$ ) and an inner wheel region ( $2.5 < |\eta| < 3.2$ ) in order  
784 to provide precise coverage within the same  $\eta$  range as the ID. Overlap between the barrel  
785 and endcap regions compensates for the lower material density in the transition region.

786 **Hadronic calorimeter**

787 The hadronic calorimeter [27] covers up to  $|\eta| < 4.9$  and is comprised of three parts: the  
788 tile calorimeter with a barrel region ( $|\eta| < 1.0$ ) and extended barrel regions ( $0.8 < |\eta| < 1.7$ );  
789 the hadronic endcap calorimeter (HEC) covering  $1.5 < |\eta| < 3.2$ ; and the forward calorimeter  
790 (FCal) covering  $3.2 < |\eta| < 4.9$ . The tile calorimeter covers the EM calorimeter barrel region  
791 and uses steel as material for the absorbing layers with scintillating tiles for the active layers.  
792 Signals captured by scintillating tiles are read out from both sides using photomultiplier  
793 tubes. The HEC calorimeter covers the endcap regions of the EM calorimeter and uses a  
794 copper-LAr calorimeter layer scheme. The FCal is located close to the beamline providing  
795 coverage for particles traveling close to parallel with the beam axis. The subdetector contains  
796 three modules: one with copper absorbing layers optimized for EM measurements, and two  
797 with tungsten absorbing layers targeting hadronic cascades. All modules in the FCal use  
798 LAr as the active layer.

799 **3.2.3 Muon spectrometer**

800 Generally, the only particles that penetrate past the calorimeter layer are muons and  
801 neutrinos. The muon spectrometer (MS) [27] is situated on the outermost of the ATLAS  
802 detector and aims to track and measure muons within  $|\eta| < 2.7$ . The MS utilizes an array of  
803 toroid magnets to provide a magnetic field perpendicular to the muon trajectory, bending  
804 the track in order to measure its curvature. The magnetic field is powered by a large barrel

805 toroid ( $|\eta| < 1.4$ ) with strength of 0.5 T and two endcap toroid magnets ( $1.6 < |\eta| < 2.7$ ) of  
806 1 T. Both types contribute to the magnetic field in the transition region ( $1.4 < |\eta| < 1.6$ ).

807 To measure the muon itself, four types of large gas-filled chambers known as muon cham-  
808 bers [27] are designed and constructed for two main goals: triggering on potential muon  
809 candidates entering the MS and tracking their trajectories through the detector with high  
810 precision. The tracking system include Monitored Drift Tubes (MDTs), which record muon  
811 track information over the entire MS  $\eta$  range ( $|\eta| < 2.7$ ). The MDTs are built with multi-  
812 ple layers of drift tubes and filled with a mixture of 93% Ar and 7% CO<sub>2</sub>. Muons passing  
813 through drift tubes in the MDT ionize the gas within each tube; signals are then recorded  
814 as freed electrons drift to read-out channels under an applied electric field. In the forward  
815 region ( $2.0 < |\eta| < 2.7$ ), Cathode Strip Chambers (CSCs) are included along with MDTs.  
816 The CSCs are multiwire proportional chambers built with higher granularity and shorter  
817 drift time than the MDTs to handle tracking in an environment with high background rates

818 .

819 The MS trigger system includes Resistive Plate Chambers (RPCs) [27], which provide  
820 triggering in the barrel region ( $|\eta| < 1.05$ ) using parallel electrode plates made of resistive  
821 materials with a gas mixture inbetween. High voltage is applied to the plates, accelerat-  
822 ing the electrons freed from ionized gas and creating a fast avalanche of charge, which is  
823 collected on external read-out strips almost instantaneously. Triggering and coarse position  
824 measurements in the endcap region ( $1.05 < |\eta| < 2.5$ ) is handled by Thin-Gap Chambers  
825 (TGCs). Similar to CSCs, TGCs are multiwire proportional chambers with a small wire gap  
826 ("thin-gap") and high applied voltage across the gap, resulting in fast response time giving  
827 TGCs the capabilities to identify muon candidates in real time.

828    **3.2.4 Trigger & data acquisition**

829    The LHC produces a colossal amount of collision data at a bunch crossing rate of 40 MHz  
830    with bunch spacing of 25 ns. The ATLAS Trigger and Data Acquisition (TDAQ) system [94]  
831    synchronously identifies and records interesting events for in-depth analysis. The ATLAS  
832    trigger system in Run 2 consists of two steps: Level-1 (L1) trigger and High-Level Trigger  
833    (HLT). Events failing any step in the trigger chain are permanently lost.

834    The L1 trigger hardware is divided into L1 calorimeter triggers (L1Calo) and L1 muon  
835    triggers (L1Muon) [94]. L1Calo trigger uses information from ATLAS calorimeter system  
836    to quickly identify signs of high  $p_T$  objects e.g. EM clusters, jets and missing transverse  
837    energy  $E_T^{\text{miss}}$  (section 4.4). Similarly, L1Muon uses information from the RPCs and TGCs  
838    of the MS to make quick decisions on potentially interesting muon candidates. Outputs  
839    from L1Calo and L1Muon are fed into the L1 topological trigger (L1Topo) for additional  
840    filtering based on event topology and multi-object correlation, allowing for more selective  
841    and physics-motivated triggering. Decisions from all three types of L1 triggers are provided  
842    as inputs for the Central Trigger Processor (CTP) for a final Level-1 Accept (L1A) decision.

843    The entire L1 trigger chain results in a 2.5  $\mu\text{s}$  latency and reduces the event rate to 100 kHz.

844    Events passing L1 triggers are sent to HLTs before being saved to offline storage at  
845    CERN data centers. HLTs are software-based triggers used for more complex and specific  
846    selections on physics objects required by targeted analysis goals, in turn requiring more  
847    computing power with longer latency. After HLT selections, the event rate is reduced to 1  
848    kHz on average [94]. Overall, the full trigger chain reduces the event rate for ATLAS by  
849    approximately a factor of  $4 \times 10^4$ .

# 850 Chapter 4. Particle Reconstruction & Identifi- 851 fication

852 Activity within the ATLAS detector is recorded as raw electronic signals, which can  
853 be utilized by ATLAS reconstruction software to derive physics objects for analysis. This  
854 chapter describes the reconstruction and identification of basic objects (e.g. interaction  
855 vertices, tracks, topological clusters of energy deposits) and subsequently of complex physics  
856 objects i.e. particles and particle signatures.

## 857 4.1 Primary reconstruction

### 858 4.1.1 Tracks

859 Charged particles traveling through the ATLAS detector deposit energy in different layers  
860 of the ID and MS. The ID track reconstruction software consists of two algorithm chains:  
861 inside-out and outside-in track reconstruction [95–97].

862 The inside-out algorithm is primarily used for the reconstruction of primary particles  
863 i.e. particles directly produced from  $pp$  collisions or decay products of short-lived particles.

864 The process starts by forming space points from seeded hits in the silicon detectors within  
865 the pixel & SCT detectors. Hits further away from the interaction vertex are added to  
866 the track candidate using a combinatorial Kalman filter [98] pattern recognition algorithm.

867 Track candidates are then fitted with a  $\chi^2$  filter [99] and loosely matched to a fixed-sized  
868 EM cluster. Successfully matched track candidates are re-fitted with a Gaussian-sum filter  
869 (GSF) [100], followed by a track scoring strategy to resolve fake tracks & hit ambiguity

870 between different tracks [101]. The track candidate is then extended to the TRT to form  
871 final tracks satisfying  $p_T > 400$  MeV. The outside-in algorithm handles secondary tracks  
872 mainly produced from long-lives particles or decays of primary particles by back-tracking  
873 from TRT segments, which are then extended inward to match silicon hits in the pixel and  
874 SCT detectors to form track reconstruction objects.

### 875 4.1.2 Vertices

876 Vertices represent the point of interaction or decay for particles within the ATLAS de-  
877 tector. Primary vertices (PVs) are defined as the point of collision for hard-scattering  $pp$   
878 interactions, while secondary or displaced vertices result from particle decays occurring at a  
879 distance from its production point.

880 Reconstruction of PVs is crucial to accurately profile the kinematic information of an  
881 event and form a basis for subsequent reconstruction procedures. Primary vertex recon-  
882 struction occurs in two stages: vertex finding and vertex fitting [102]. The vertex finding  
883 algorithm uses the spatial coordinates of reconstructed tracks to form the seed for a vertex  
884 candidate. An adaptive vertex fitting algorithm [103] then iteratively evaluates track-vertex  
885 compatibility to estimate a new best vertex position. Less compatible tracks are down-  
886 weighted in each subsequent iteration, and incompatible tracks are removed and can be  
887 used for another vertex seed; the process is repeated until no further PV can be found.  
888 All reconstructed vertices without at least two matched tracks are considered invalid and  
889 discarded.

890 Secondary vertex reconstruction uses the Secondary Vertex Finder (SVF) algorithm [104]  
891 which is primarily designed to reconstruct  $b$ - and  $c$ -hadrons for flavor tagging purposes. The  
892 SVF aims to reconstruct one secondary vertex per jet and only considers tracks that are

893 matched to a two-track vertex and contained within a  $p_T$ -dependent cone around the jet  
894 axis. The tracks are then used to reconstruct a secondary vertex candidate using an iterative  
895 process similar to the PV vertex fitting procedure.

896 **Pile-up**

897 At high luminosities, multiple interactions can be associated with one bunch crossing,  
898 resulting in many PVs. The effect is called pile-up [105], and usually result from soft QCD  
899 interactions. Pile-up can be categorized into two types: in-time pile-up, stemming from  
900 additional  $pp$  collisions in the same bunch crossing that is not the hard-scatter process; out-  
901 of-time pile-up, resulting from leftover energy deposits in the calorimeters from other bunch  
902 crossings.

903 **4.1.3 Topological clusters**

904 Topological clusters (topo-clusters) [106] consist of clusters of spatially related calorimeter  
905 cell signals. Topo-clusters are primarily used to reconstruct hadron- and jet-related objects  
906 in an effort to extract signal while minimizing electronic effects and physical fluctuations, and  
907 also allow for recovery of energy lost through bremsstrahlung or photon conversions. Cells  
908 with signal-to-noise ratio  $\zeta_{\text{cell}}^{\text{EM}}$  passing a primary seed threshold are seeded into a dynamic  
909 topological cell clustering algorithm as part of a proto-cluster. Neighboring cells satisfying a  
910 cluster growth threshold are collected into the proto-cluster. If a cell is matched to two proto-  
911 clusters, the clusters are merged. Two or more local signal maxima in a cluster satisfying  
912  $E_{\text{cell}}^{\text{EM}} > 500 \text{ MeV}$  suggest the presence of multiple particles in close proximity, and the cluster  
913 is split accordingly to maintain good resolution of the energy flow. The process continues  
914 iteratively until all cells with  $\zeta_{\text{cell}}^{\text{EM}}$  above a principal cell filter level have been matched to a

915 cluster.

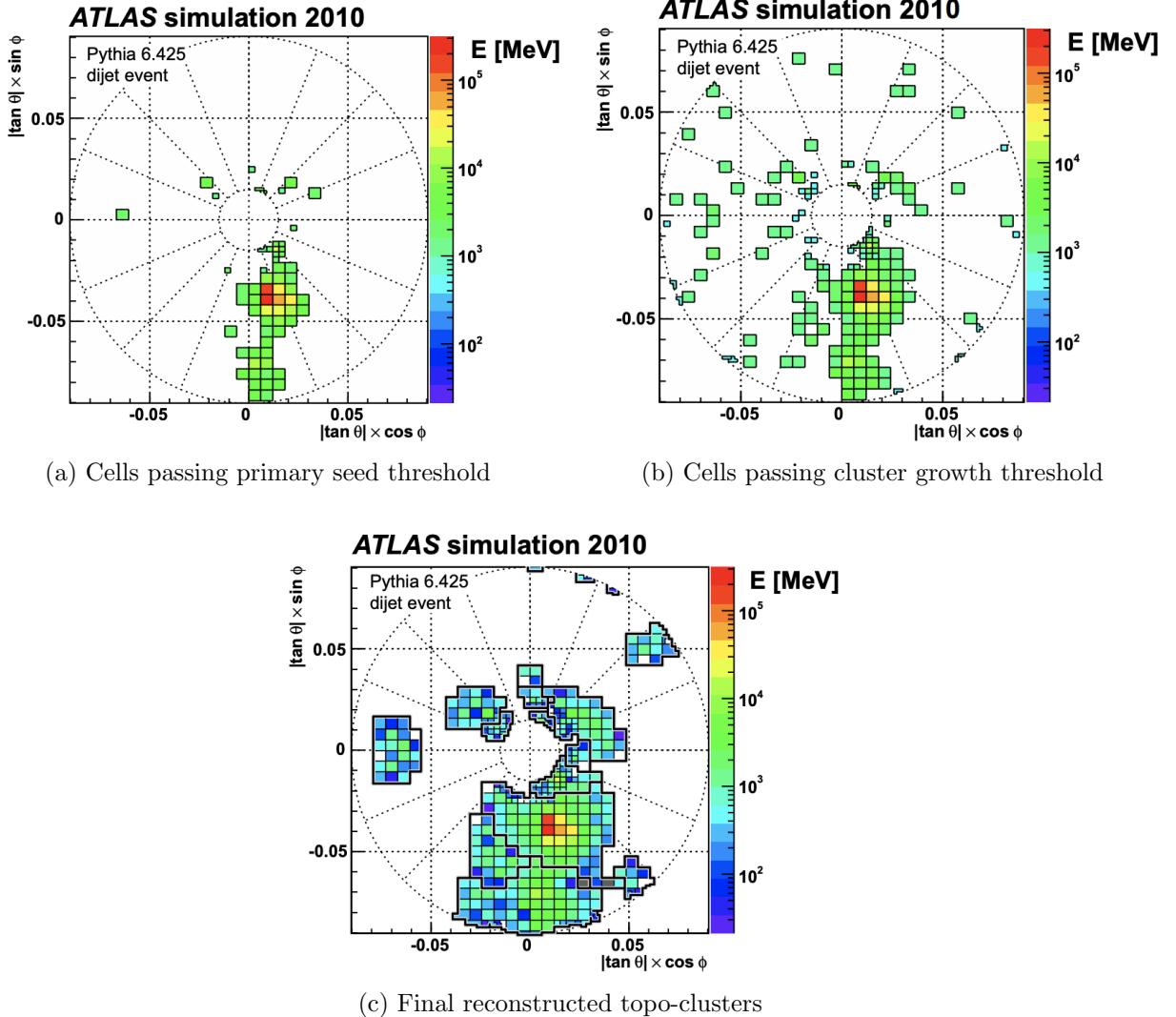


Figure 4.1: Stages of topo-cluster formation corresponding to each threshold. In (a), proto-clusters are seeded from cells with adequate signal significance  $\zeta_{\text{cell}}^{\text{EM}}$ . The clusters are further merged and split in (b) following a predefined cluster growth threshold. The process stops in (c) when all sufficiently significant signal hits have been matched to a cluster [106].

## 916 4.2 Jets

917 Quarks, gluons and other hadrons with non-neutral color charge cannot be observed  
918 individually due to QCD color confinement, which forces a non-color-neutral hadron to

919 almost immediately undergo hadronization, producing a collimated cone of color-neutral  
920 hadrons defined as a jet. Jet signals can be used to reconstruct and indirectly observe the  
921 quarks or gluons from which the jet originated in the original hard-scattering process.

### 922 4.2.1 Jet reconstruction

923 The ATLAS jet reconstruction pipeline is largely carried out using a particle flow (PFlow)  
924 algorithm combined with an anti- $k_t$  jet clustering algorithm. The PFlow algorithm [107]  
925 utilizes topo-clusters along with information from both the calorimeter systems and the ID in  
926 order to make use of the tracker system’s advantages in low-energy momentum resolution and  
927 angular resolution. First, the energy from charged particles is removed from the calorimeter  
928 topo-clusters; then, it is replaced by particle objects created using the remaining energy in  
929 the calorimeter and tracks matched to topo-clusters. The ensemble of ”particle flow objects”  
930 and corresponding matched tracks are used as inputs for the iterative anti- $k_t$  algorithm [108].

931 The main components of the anti- $k_t$  algorithm involve the distance  $d_{ij}$  between two  
932 jet candidates  $i$  and  $j$ , and the distance  $d_{iB}$  between the harder jet candidate of the two  
933 (defined as  $i$ ) and the beamline  $B$ . If  $d_{ij} < d_{iB}$ , then the two jet candidates are combined  
934 and returned to the pool of candidates; otherwise, jet candidate  $i$  is considered a jet and  
935 removed from the pool. The distance  $d_{ij}$  is inversely proportional to a predefined radius  
936 parameter  $\Delta R$  in order to control reconstruction quality for small- $R$  and large- $R$  jets. This  
937 analysis uses  $\Delta R = 0.4$  to better handle heavily collimated small- $R$  jets resulting from parton  
938 showers.

939 The anti- $k_t$  jets so far have only been reconstructed at the EM level and need to be  
940 calibrated to match the energy scale of jets reconstructed at particle level. This is done  
941 via a MC-based jet energy scale (JES) calibration sequence, along with further calibrations

942 to account for pile-up effects and energy leakage. The full JES calibration sequence is  
 943 shown in Figure 4.2. All calibrations except origin correction are applied to the jet's four-  
 944 momentum i.e. jet  $p_T$ , energy and mass. Afterwards, a jet energy resolution (JER) [109]  
 945 calibration step is carried out in a similar manner to JES to match the resolution of jets in  
 946 dijet events. To further suppress pile-up effects, a neural-network based jet vertex tagger  
 947 (NNJvt) discriminant was developed based on the previous jet vertex tagger (JVT) algorithm  
 948 [105] and applied to low- $p_T$  reconstructed jets.

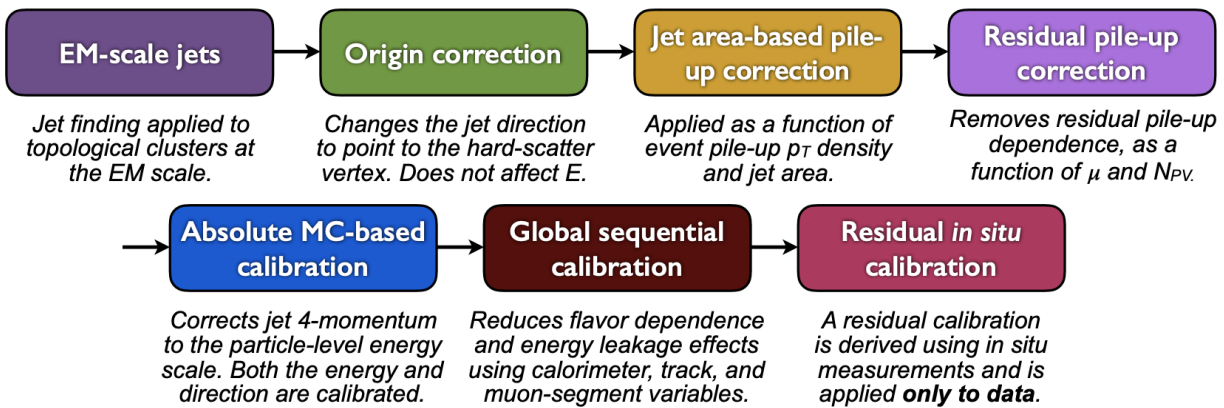


Figure 4.2: Jet energy scale calibration sequence for EM-scale jets [110].

### 949 4.2.2 Flavor tagging

950 Identifying and classifying hadronic jets are important tasks for ATLAS physics, for  
 951 example analyses involving Higgs decays  $H \rightarrow b\bar{b}$  or top quarks. Flavor tagging or  $b$ -tagging  
 952 is the process of identifying jets containing  $b$ -hadrons,  $c$ -hadrons, light-hadrons ( $uds$ -hadrons)  
 953 or jets from hadronically decaying  $\tau$  leptons. Distinguishing  $b$ -jets is possible due to their  
 954 characteristically long lifetime ( $\tau \approx 1.5$  ps), displaced secondary decay vertex and high decay  
 955 multiplicity.

956 Usage of  $b$ -tagging in this analysis is done via five operating points (OPs), corresponding

957 to 65%, 70%, 77%, 85% and 90%  $b$ -jet tagging efficiency  $\varepsilon_b$  in simulated  $t\bar{t}$  events, in order  
958 from the tightest to loosest discriminant cut point. The OPs are defined by placing selections  
959 on the tagger output to provide a predefined  $\varepsilon_b$  level; the selection cuts act as a variable  
960 trade-off between  $b$ -tagging efficiency and  $b$ -jet purity i.e.  $c$ - or light-jet rejection. For this  
961 analysis, a jet is considered  $b$ -tagged if it passes the 85% OP. The  $b$ -tagged jet is then  
962 assigned a pseudo-continuous  $b$ -tagging (PCBT) score, which quantifies a jet's ability to  
963 satisfy different OPs. The score can take integer values between 1 and 6, where a score of 6  
964 is assigned to jets passing all OP thresholds; a score of 2 for jets that pass only the tightest  
965 OP (90%); and a score of 1 for jets that pass no OP. A value of -1 is also defined for any jet  
966 that does not satisfy  $b$ -tagging criteria. Since the targeted  $t\bar{t}t\bar{t}$  final states contain at least  
967 four  $b$ -hadrons from top and  $W$  decays, a  $b$ -tagging OP of 85% is used to maintain high  
968 purity during  $b$ -tagged jet selections in the signal region.

969 **GN2  $b$ -tagging algorithm**

970 For this analysis,  $b$ -jets are identified and tagged with the GN2v01  $b$ -tagger [111]. The  
971 GN2 algorithm uses a Transformer-based model [112] modified to incorporate domain knowl-  
972 edge and additional auxiliary physics objectives: grouping tracks with a common vertex and  
973 predicting the underlying physics process for a track. The network structure is shown in  
974 Figure 4.3. The GN2  $b$ -tagger form the input vector by concatenating 2 jet variables and  
975 19 track reconstruction variables (for up to 40 tracks), normalized to zero mean and unit  
976 variance. The output consists of a track-pairing output layer of size 2, a track origin clas-  
977 sification layer of 7 categories, and a jet classification layer of size 4 for the probability of  
978 each jet being a  $b$ -,  $c$ -, light- or  $\tau$ -jet respectively. For  $b$ -tagging purpose, a discriminant is

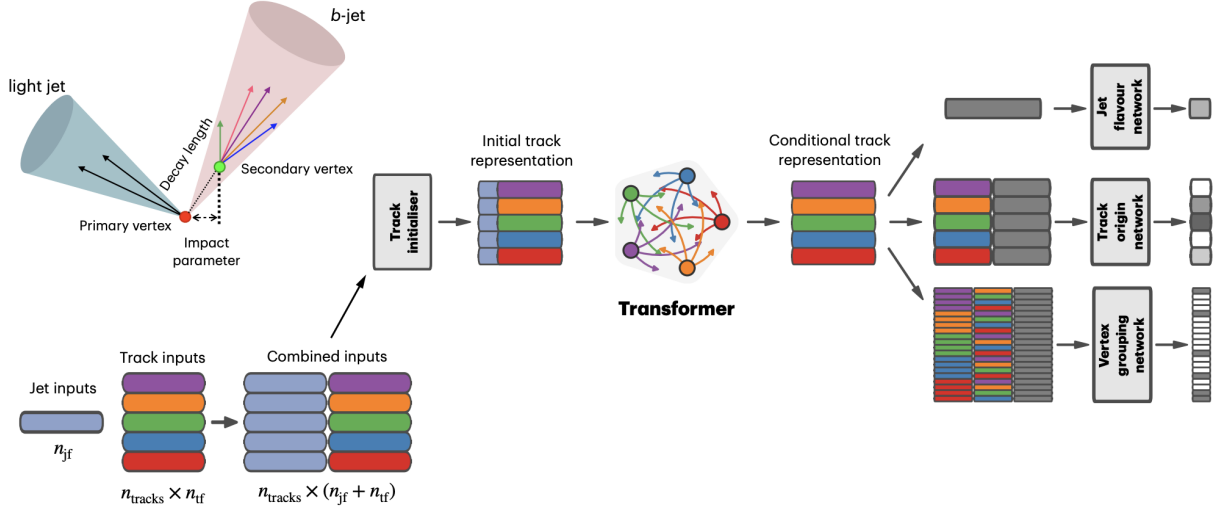


Figure 4.3: Overview of the GN2 architecture. The number of jet and track features are represented by  $n_{jf}$  and  $n_{tf}$  respectively. The global jet representation and track embeddings output by the Transformer encoder are used as inputs for three task-specific networks [111].

979 defined using these four outputs

$$D_b = \ln \left( \frac{p_b}{f_c p_c + f_\tau p_\tau + (1 - f_c - f_\tau)p_{\text{light}}} \right) \quad (4.1)$$

980 where  $p_x$  is the probability of the jet being an  $x$ -jet as predicted by GN2, and  $f_c$ ,  $f_\tau$  are tun-  
 981 able free parameters controlling balance between  $c$ - and light-jet rejection. Simulated SM  $t\bar{t}$   
 982 and BSM  $Z'$  events from  $pp$  collisions were used as training and evaluation samples. In order  
 983 to minimize bias, both  $b$ - and light-jet samples are re-sampled to match  $c$ -jet distributions.  
 984 Figure 4.4 shows the performance of GN2 compared to the previous convolutional neural  
 985 network-based standard  $b$ -tagging algorithm DL1d, in terms of  $c$ -, light- and  $\tau$ -jet rejection  
 986 as a function of  $b$ -tagging efficiency. The network gives a factor of 1.5-4 improvement in  
 987 experimental applications compared to DL1d [111], without dependence on the choice of  
 988 MC event generator or inputs from low-level flavor tagging algorithm.

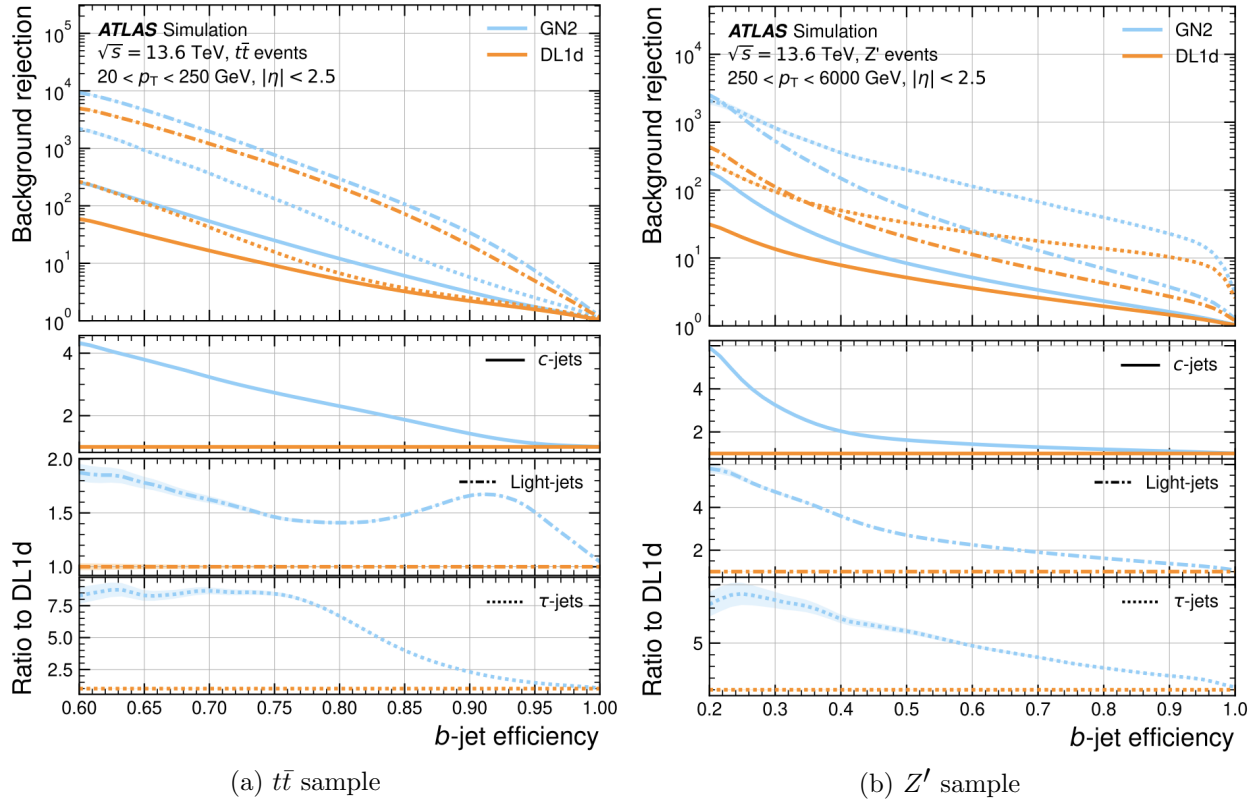


Figure 4.4: The  $c$ -, light- and  $\tau$ -jet rejection rate as a function of  $b$ -tagging efficiency for GN2 and DL1d using (a) jets in the  $t\bar{t}$  sample, and (b) jets in the  $Z'$  sample. The performance ratios of GN2 to DL1d are shown in the bottom panels [111].

## 989 Efficiency calibration

Due to imperfect description of detector response and physics modeling effects in simulation,  
 the  $b$ -tagging efficiency predicted by MC simulation  $\varepsilon_b^{\text{sim}}$  requires a correction factor  
 to match the efficiency measured in collision data  $\varepsilon_b^{\text{data}}$ . The correction scale factors (SFs)  
 are defined as  $\text{SF} = \varepsilon_b^{\text{data}} / \varepsilon_b^{\text{sim}}$  and are determined by data-to-MC calibration using samples  
 enriched in dileptonic  $t\bar{t}$  decays [113]. The resulting SFs are applied to MC simulated jets  
 individually.

## 996 4.3 Leptons

997 Lepton reconstruction in ATLAS involves electron and muon reconstruction since tau  
998 decays quickly, and depending on decay mode can be reconstructed using either jets or light  
999 leptons. From here on out within this dissertation, leptons will be used exclusively to refer to  
1000 electrons and muons. Leptons can be classified into two categories: prompt leptons resulting  
1001 from heavy particle decays and non-prompt leptons resulting from detector or reconstruction  
1002 effects, or from heavy-flavor hadron decays.

### 1003 4.3.1 Electrons

1004 Electrons leave energy signature in the detector by interacting with the detector materials  
1005 and losing energy in the form of bremsstrahlung photons. A bremsstrahlung photon can  
1006 produce an electron-positron pair which can itself deposit signals in the detector, creating a  
1007 cascade of particles that can leave multiple of either tracks in the ID or EM showers in the  
1008 calorimeters, all of which are considered part of the same EM topo-cluster. Electron signal  
1009 signature has three characteristic components: localized energy deposits in the calorimeters,  
1010 multiple tracks in the ID and compatibility between the above tracks and energy clusters in  
1011 the  $\eta \times \phi$  plane [114]. Electron reconstruction in ATLAS follows these steps accordingly.

1012 Seed-cluster reconstruction and track reconstruction are performed sequentially in ac-  
1013 cordance with the iterative topo-clustering algorithm and track reconstruction method de-  
1014 scribed in section 4.1. The seed-cluster and GSF-refitted track candidate not associated  
1015 with a conversion vertex are matched to form an electron candidate. The cluster energy is  
1016 then calibrated using multivariate techniques on data and simulation to match the original  
1017 electron energy.

1018 **Electron identification**

1019 Additional LH-based identification selections using ID and EM calorimeter information  
1020 are implemented to further improve the purity of reconstructed electrons in the  $|\eta| < 2.47$  re-  
1021 gion of the detector [114]. The electron LH function is built with the signal being prompt elec-  
1022 trons and background being objects with similar signature to prompt electrons i.e. hadronic  
1023 jet deposits, photon conversions or heavy-flavor hadron decays. Three identification OPs  
1024 are defined for physics analyses: *Loose*, *Medium* and *Tight*, optimized for 9 bins in  $|\eta|$  and  
1025 12 bins in  $E_T$  with each OP corresponding to a fixed efficiency requirement for each bin.  
1026 For typical EW processes, the target efficiencies for *Loose*, *Medium* and *Tight* start at 93%,  
1027 88% and 80% respectively and increase with  $E_T$ . Similar to  $b$ -tagging OPs, the electron  
1028 identification OPs represent a trade-off in signal efficiency and background rejection. The  
1029 electron efficiency are estimated using tag-and-probe method on samples of  $J/\Psi \rightarrow ee$  and  
1030  $Z \rightarrow ee$  [114]. The *Tight* electron identification OP is used for this analysis.

1031 **Electron isolation**

1032 A characteristic distinction between prompt electrons and electrons from background  
1033 processes is the relative lack of activity in both the ID and calorimeters within an  $\Delta\eta \times \Delta\phi$   
1034 area surrounding the reconstruction candidate. Calorimeter-based and track-based electron  
1035 isolation variables [114] are defined to quantify the amount of activity around the electron  
1036 candidate using topo-clusters and reconstructed tracks respectively.

1037 Calorimeter-based isolation variables  $E_T^{\text{cone}XX}$  are computed by first summing the energy  
1038 of topo-clusters with barycenters falling within a cone of radius  $\Delta R = \sqrt{(\Delta\eta)^2 + (\Delta\phi)^2} =$   
1039  $XX/100$  around the direction of the electron candidate. The final isolation variables are

obtained by subtracting from the sum the energy belonging to the candidate electron at the core of the cone, then applying corrections for pile-up effects and energy leakage outside of the core. Similar to calorimeter-based variables, track-based isolation variables  $p_T^{\text{varcone}XX}$  are calculated by summing all track  $p_T$  within a cone of radius  $\Delta R$  around the electron candidate, minus the candidate's contribution. The cone radius is variable as a function of  $p_T$  and is described as

$$\Delta R \equiv \min \left( \frac{10}{p_T}, \Delta R_{\max} \right), \quad (4.2)$$

where  $p_T$  is expressed in GeV and  $\Delta R_{\max}$  is the maximum cone size, defined to account for closer proximity of decay products to the electron in high-momentum heavy particle decays. Four isolation operating points are implemented to satisfy specific needs by physics analyses: *Loose*, *Tight*, *HighPtCaloOnly* and *Gradient* [114]. For this analysis, electrons isolation uses *Tight* requirements.

## 1051 Electron charge misidentification

Charge misidentification is a crucial irreducible background, particularly for analyses with electron charge selection criteria. Electron charge is determined by the curvature of the associated reconstructed track, and misidentification of charge can occur via either an incorrect curvature measurement or an incorrectly matched track. Inaccurate measurement is more likely for high energy electrons due to the small curvature in track trajectories at high  $p_T$ , while track matching error usually results from bremsstrahlung pair-production generating secondary tracks in close proximity [114]. Suppression of charge misidentification background in Run 2 is additionally assisted by a boosted decision tree discriminant known

1060 as the Electron Charge ID Selector (ECIDS). For this analysis, all electrons are required to  
1061 pass the ECIDS criterion.

1062 **4.3.2 Muons**

1063 Muons act as minimum-ionizing particles, leaving tracks in the MS or characteristics  
1064 energy deposits in the calorimeter and can be reconstructed globally using information from  
1065 the ID, MS and calorimeters. Five reconstruction strategies corresponding to five muon  
1066 types [116] are utilized in ATLAS:

- Combined (CB): the primary ATLAS muon reconstruction method. Combined muons  
1067 are first reconstructed using MS tracks then extrapolated to include ID tracks (outside-in strategy). A global combined track fit is performed on both MS and ID tracks.
- Inside-out combined (IO): complementary to CB reconstruction. IO muon tracks are  
1070 extrapolated from ID to MS, then fitted with MS hits and calorimeter energy loss in a  
1071 combined track fit.
- MS extrapolated (ME): ME muons are defined as muons with a MS track that cannot  
1073 be matched to an ID track using CB reconstruction. ME muons allow extension of  
1074 muon reconstruction acceptance to regions not covered by the ID ( $2.5 < |\eta| < 2.7$ )
- Segment-tagged (ST): ST muons are defined as a successfully matched ID track that  
1076 satisfies tight angular matching criteria to at least one reconstructed MDT or CSC  
1077 segment when extrapolated to the MS. MS reconstruction is used primarily when  
1078 muons only crossed one layer of MS chambers.
- Calorimeter-tagged (CT): CT muons are defined as an ID track that can be matched to  
1080

1081 energy deposits consistent with those of a minimum-ionizing particle when extrapolated  
1082 through the calorimeter. CT reconstruction extends acceptance range to regions in the  
1083 MS with sparse instrumentation ( $|\eta| < 0.1$ ) with a higher  $p_T$  threshold of 5 GeV,  
1084 compared to the 2 GeV threshold used by other muon reconstruction algorithms due  
1085 to large background contamination at the low  $p_T$  range of  $15 < p_T < 100$  GeV [117].

## 1086 Muon identification

1087 Reconstructed muons are further filtered by identification criteria to select for high-  
1088 quality prompt muons. Requirements include number of hits in the MS and ID, track fit  
1089 properties and compatibility between measurements of the two systems. Three standard  
1090 OPs (*Loose*, *Medium*, *Tight*) are defined to better match the needs of different physics  
1091 analyses concerning prompt muon  $p_T$  resolution, identification efficiency and non-prompt  
1092 muon rejection. The default identification OP for ATLAS physics and also the OP used in  
1093 this analysis is *Medium*, which provides efficiency and purity suitable for a wide range of  
1094 studies while minimizing systematic uncertainties [116].

## 1095 Muon isolation

1096 Muons from heavy particle decays are often produced in an isolated manner compared to  
1097 muons from semileptonic decays, and is therefore an important tool for background rejection  
1098 in many physics analyses. Muon isolation strategies are similar to that of electron in section  
1099 4.3.1, with track-based and calorimeter-based isolation variables. Seven isolation OPs are  
1100 defined using either or both types of isolation variables, balancing between prompt muon  
1101 acceptance and non-prompt muon rejection. The full definition and description for the muon  
1102 isolation OPs are detailed in Ref. [116].

## 1103 4.4 Missing transverse momentum

1104 Collisions at the LHC happen along the  $z$ -axis of the ATLAS coordination system between  
1105 two particle beam of equal center-of-mass energy. By conservation of momentum, the sum of  
1106 transverse momenta of outgoing particles should be zero. A discrepancy between measured  
1107 momentum and zero would then suggest the presence of undetectable particles, which would  
1108 consist of either SM neutrinos or some unknown BSM particles, making missing transverse  
1109 momentum ( $E_T^{\text{miss}}$ ) an important observable to reconstruct.

1110 Reconstructing  $E_T^{\text{miss}}$  utilizes information from fully reconstructed leptons, photons, jets  
1111 and other matched track-vertex objects not associated with a prompt object (soft signals),  
1112 defined with respect to the  $x(y)$ -axis as

$$E_{x(y)}^{\text{miss}} = - \sum_{i \in \{\text{hard objects}\}} p_{x(y),i} - \sum_{j \in \{\text{soft signals}\}} p_{x(y),j}, \quad (4.3)$$

1113 where  $p_{x(y)}$  is the  $x(y)$ -component of  $p_T$  for each particle [118]. The following observables  
1114 can then be defined:

$$\begin{aligned} \mathbf{E}_T^{\text{miss}} &= (E_x^{\text{miss}}, E_y^{\text{miss}}), \\ E_T^{\text{miss}} &= |\mathbf{E}_T^{\text{miss}}| = \sqrt{(E_x^{\text{miss}})^2 + (E_y^{\text{miss}})^2}, \\ \phi^{\text{miss}} &= \tan^{-1}(E_y^{\text{miss}}/E_x^{\text{miss}}), \end{aligned} \quad (4.4)$$

1115 where  $E_T^{\text{miss}}$  represents the magnitude of the missing transverse energy vector  $\mathbf{E}_T^{\text{miss}}$ , and  
 1116  $\phi^{\text{miss}}$  its direction in the transverse plane. The vectorial sum  $\mathbf{E}_T^{\text{miss}}$  can be broken down into

$$\mathbf{E}_T^{\text{miss}} = - \underbrace{\sum_{\text{selected electrons}} \mathbf{p}_T^e - \sum_{\text{selected muons}} \mathbf{p}_T^\mu - \sum_{\text{accepted photons}} \mathbf{p}_T^\gamma - \sum_{\text{accepted } \tau\text{-leptons}} \mathbf{p}_T^\tau}_{\text{hard term}} - \underbrace{\sum_{\text{accepted jets}} \mathbf{p}_T^{\text{jet}} - \sum_{\text{unused tracks}} \mathbf{p}_T^{\text{track}}}_{\text{soft term}}. \quad (4.5)$$

1117 Two OPs are defined for  $E_T^{\text{miss}}$ , *Loose* and *Tight*, with selections on jet  $p_T$  and JVT criteria  
 1118 [119]. The *Tight* OP is used in this analysis; *Tight* reduces pile-up dependence of  $E_T^{\text{miss}}$   
 1119 by removing the phase space region containing more pile-up than hard-scatter jets, at the  
 1120 expense of resolution and scale at low pile-up,

## 1121 4.5 Overlap removal

1122 Since different objects are reconstructed independently, it is possible for the same de-  
 1123 tector signals to be used to reconstruct multiple objects. An overlap removal strategy is  
 1124 implemented to resolve ambiguities; the overlap removal process for this analysis applies  
 1125 selections in Table 4.1 sequentially, from top to bottom.

Table 4.1: Overlap removal process for this analysis, applied sequentially from top to bottom.

Remove	Keep	Matching criteria
Electron	Electron	Shared ID track, $p_{T,1}^e < p_{T,2}^e$
Muon	Electron	Shared ID track, CT muon
Electron	Muon	Shared ID track
Jet	Electron	$\Delta R < 0.2$
Electron	Jet	$\Delta R < 0.4$
Jet	Muon	( $\Delta R < 0.2$ or ghost-associated) & $N_{\text{track}} < 3$
Muon	Jet	$\Delta R < \min(0.4, 0.04 + 10\text{GeV}/p_T^\mu)$

## 1126 4.6 Object definition

1127 Table 4.2 summarizes the selections on physics objects used in this analysis. Each se-  
1128 lection comes with associated calibration scale factors (SFs) to account for discrepancies  
1129 between data and MC simulation, and are applied multiplicatively to MC event weights.

Table 4.2: Summary of object selection criteria used in this analysis.  $\ell_0$  refers to the leading lepton in the event.

Selection	Electrons	Muons	Jets
$p_T$ [GeV]	$> 15$ $p_T(\ell_0) > 28$	$> 15$	$> 20$
$ \eta $	$1.52 \leq  \eta  < 2.47$ $< 1.37$	$< 2.5$	$< 2.5$
Identification	<i>TightLH</i> pass ECIDS ( $ee/e\mu$ )	<i>Medium</i>	NNJvt <i>FixedEffPt</i> ( $p_T < 60$ , $ \eta  < 2.4$ )
Isolation	<i>Tight_VarRad</i>	<i>PflowTight_VarRad</i>	
Track-vertex assoc.			
$ d_0^{\text{BL}}(\sigma) $	$< 5$	$< 3$	
$ \Delta z_0^{\text{BL}} \sin \theta $ [mm]	$< 0.5$	$< 0.5$	

# 1130 Chapter 5. Data & Simulated Samples

## 1131 5.1 Data samples

1132 Data samples used in this analysis were collected by the ATLAS detector during Run  
1133 2 data-taking campaign between 2015-2018. The samples contain  $pp$  collisions at center-of-  
1134 mass energy of  $\sqrt{s} = 13$  TeV with 25 ns bunch-spacing, which corresponds to an integrated  
1135 luminosity of  $140 \text{ fb}^{-1}$  with an uncertainty of 0.83% [87]. The HLT trigger strategy is similar  
1136 to that of previous  $t\bar{t}t\bar{t}$  observation analysis [44] and include single lepton and dilepton  
1137 triggers. Calibration for di-muon and electron-muon triggers were not ready for the samples  
1138 used in this analysis, and are therefore not included. Events are also required to contain at  
1139 least one lepton matched to the corresponding object firing the trigger. Triggers used are  
1140 summarized in Table 5.1.

## 1141 5.2 Monte Carlo samples

1142 Monte Carlo simulated samples are used to estimate signal acceptance before unblinding,  
1143 profile the physics background for the analysis and to study object optimizations. Simulated  
1144 samples for this analysis use are generated from ATLAS generalized MC20a/d/e samples for  
1145 Run 2, using full detector simulation (FS) and fast simulation (AF3) to simulate detector  
1146 response. MC samples used and simulation processes are summarized in Table 5.2

Table 5.1: Summary of all HLT triggers used in this analysis. Events are required to pass at least one trigger.

Trigger	Data period			
	2015	2016	2017	2018
Single electron triggers				
HLT_e24_lhmedium_L1EM20VH	✓	-	-	-
HLT_e60_lhmedium	✓	-	-	-
HLT_e120_lhloose	✓	-	-	-
HLT_e26_lhtight_nod0_ivarloose	-	✓	✓	✓
HLT_e60_lhmedium_nod0	-	✓	✓	✓
HLT_e140_lhloose_nod0	-	✓	✓	✓
Di-electron triggers				
HLT_2e12_lhloose_L12EM10VH	✓	-	-	-
HLT_2e17_lhvloose_nod0	-	✓	-	-
HLT_2e24_lhvloose_nod0	-	-	✓	✓
HLT_2e17_lhvloose_nod0_L12EM15VHI	-	-	-	✓
Single muon trigger				
HLT_mu20_iloose_L1MU15	✓	-	-	-
HLT_mu40	✓	-	-	-
HLT_mu26_ivarmedium	-	✓	✓	✓
HLT_mu50	-	✓	✓	✓

### <sup>1147</sup> 5.2.1 $t\bar{t}Z'$ signal samples

<sup>1148</sup> Signal  $t\bar{t}Z'$  samples were generated based on the simplified topophilic resonance model in  
<sup>1149</sup> section 2.2.1 where a color singlet vector resonance couples strongly to only top and antitop.  
<sup>1150</sup> Six  $Z'$  mass points were utilized for the generation of the signal sample: 1000, 1250, 1500,  
<sup>1151</sup> 2000, 2500 and 3000 GeV. The top- $Z'$  coupling  $c_t$  is chosen to be 1 for a narrow resonance  
<sup>1152</sup> peak, and the chirality angle  $\theta$  is chosen to be  $\pi/4$  to suppress loop production of  $Z'$ . The  
<sup>1153</sup> samples were then generated with MADGRAPH5\_AMC@NLO v.3.5.0 [120] at LO with the  
<sup>1154</sup> NNPDF3.1LO [121] PDF set interfaced with PYTHIA8 [122] using A14 tune and NNPDF2.3lo  
<sup>1155</sup> PDF set for parton showering and hadronization. The resonance width is calculated to be

Table 5.2: Summary of all Monte-Carlo samples used in this analysis.  $V$  refers to an EW ( $W^\pm/Z/\gamma^*$ ) or Higgs boson. Matrix element (ME) order refers to the order in QCD of the perturbative calculation. Tune refers to the underlying-event tune of the parton shower (PS) generator.

Process	ME Generator	ME Order	ME PDF	PS	Tune	Sim.
<b>Signals</b>						
$t\bar{t}Z'$	MADGRAPH5_AMC@NLO LO		NNPDF3.1LO	PYTHIA8	A14	FS
<b><math>t\bar{t}\bar{t}</math> and <math>t\bar{t}t</math></b>						
$t\bar{t}\bar{t}$	MADGRAPH5_AMC@NLO NLO		NNPDF3.0nlo	PYTHIA8	A14	AF3
	MADGRAPH5_AMC@NLO NLO		MMHT2014 LO	HERWIG7	H7-UE-MMHT	AF3
	SHERPA	NLO	NNPDF3.0nnlo	HERWIG7	SHERPA	FS
$t\bar{t}t$	MADGRAPH5_AMC@NLO LO		NNPDF2.3lo	PYTHIA8	A14	AF3
<b><math>t\bar{t}V</math></b>						
$t\bar{t}H$	POWHEGBOX v2	NLO	NNPDF3.0nlo	PYTHIA8	A14	FS
	POWHEGBOX v2	NLO	NNPDF3.0nlo	HERWIG7	H7.2-Default	FS
$t\bar{t}(Z/\gamma^*)$	MADGRAPH5_AMC@NLO NLO		NNPDF3.0nlo	PYTHIA8	A14	FS
	SHERPA	NLO	NNPDF3.0nnlo	SHERPA	SHERPA	FS
$t\bar{t}W$	SHERPA	NLO	NNPDF3.0nnlo	SHERPA	SHERPA	FS
	SHERPA	LO	NNPDF3.0nnlo	SHERPA	SHERPA	FS
<b><math>t\bar{t}</math> and Single-Top</b>						
$t\bar{t}$	POWHEGBOX v2	NLO	NNPDF3.0nlo	PYTHIA8	A14	FS
$tW$	POWHEGBOX v2	NLO	NNPDF3.0nlo	PYTHIA8	A14	FS
$t(q)b$	POWHEGBOX v2	NLO	NNPDF3.0nlo (s)	PYTHIA8	A14	FS
			NNPDF3.0nlo 4f (t)			FS
$tWZ$	MADGRAPH5_AMC@NLO NLO		NNPDF3.0nlo	PYTHIA8	A14	FS
$tZ$	MADGRAPH5_AMC@NLO LO		NNPDF3.0nlo 4f	PYTHIA8	A14	FS
<b><math>t\bar{t}VV</math></b>						
$t\bar{t}WW$	MADGRAPH5_AMC@NLO LO		NNPDF3.0nlo	PYTHIA8	A14	FS
$t\bar{t}WZ$	MADGRAPH	LO	NNPDF3.0nlo	PYTHIA8	A14	AF3
$t\bar{t}HH$	MADGRAPH	LO	NNPDF3.0nlo	PYTHIA8	A14	AF3
$t\bar{t}WH$	MADGRAPH	LO	NNPDF3.0nlo	PYTHIA8	A14	AF3
$t\bar{t}ZZ$	MADGRAPH	LO	NNPDF3.0nlo	PYTHIA8	A14	AF3
<b><math>V(VV)+\text{jets}</math> and <math>VH</math></b>						
$V+\text{jets}$	SHERPA	NLO	NNPDF3.0nnlo	SHERPA	SHERPA	FS
$VV+\text{jets}$	SHERPA	NLO	NNPDF3.0nnlo	SHERPA	SHERPA	FS
		LO ( $gg \rightarrow VV$ )				FS
$VVV+\text{jets}$	SHERPA	NLO	NNPDF3.0nnlo	SHERPA	SHERPA	FS
$VH$	POWHEGBOX v2	NLO	NNPDF3.0aznlo	PYTHIA8	A14	FS

<sub>1156</sub> 4% for  $c_t = 1$ .

## <sub>1157</sub> 5.2.2 Background samples

### <sub>1158</sub> SM $t\bar{t}t\bar{t}$ background

<sub>1159</sub> The nominal SM  $t\bar{t}t\bar{t}$  sample was generated with MADGRAPH5\_AMC@NLO [120] at  
<sub>1160</sub> NLO in QCD with the NNPDF3.0nlo [121] PDF set and interfaced with PYTHIA8.230 [122]  
<sub>1161</sub> using A14 tune [123]. Decays for top quarks are simulated at LO with MADSPIN [124,  
<sub>1162</sub> 125] to preserve spin information, while decays for  $b$ - and  $c$ -hadrons are simulated with  
<sub>1163</sub> EVTGEN v1.6.0 [126]. The renormalization and factorization scales  $\mu_R$  and  $\mu_F$  are set  
<sub>1164</sub> to  $\sqrt{m^2 + p_T^2}/4$ , which represents the sum of transverse mass of all particles generated  
<sub>1165</sub> from the ME calculation [127]. The ATLAS detector response was simulated with AF3.  
<sub>1166</sub> Additional auxiliary  $t\bar{t}t\bar{t}$  samples are also generated to evaluate the impact of generator and  
<sub>1167</sub> PS uncertainties as shown in 5.2.

### <sub>1168</sub> $t\bar{t}W$ background

<sub>1169</sub> Nominal  $t\bar{t}W$  sample was generated using SHERPA v2.2.10 [128] at NLO in QCD with  
<sub>1170</sub> the NNPDF3.0nnlo [121] PDF with up to one extra parton at NLO and two at LO, which  
<sub>1171</sub> are matched and merged with SHERPA PS based on Catani-Seymour dipole factorization  
<sub>1172</sub> [129] using the MEPS@NLO prescription [130–133] and a merging scale of 30 GeV. Higher-  
<sub>1173</sub> order ME corrections are provided in QCD by the OpenLoops 2 library [134–136] and in  
<sub>1174</sub> EW from  $\mathcal{O}(\alpha^3) + \mathcal{O}(\alpha_S^2\alpha^2)$  (LO3 & NLO2) via two sets of internal event weights. An  
<sub>1175</sub> alternative sample with only EW corrections at LO from  $\mathcal{O}(\alpha_S\alpha^3)$  (NLO3) diagrams were  
<sub>1176</sub> also simulated with the same settings.

<sub>1177</sub>  **$t\bar{t}(Z/\gamma^*)$  background**

<sub>1178</sub> Nominal  $t\bar{t}(Z/\gamma^*)$  samples were generated separately for different ranges of dilepton in-  
<sub>1179</sub> variant mass  $m_{\ell\ell}$  to account for on-shell and off-shell  $Z/\gamma^*$  production. Sample for  $m_{\ell\ell}$   
<sub>1180</sub> between 1 and 5 GeV was produced using MADGRAPH5\_AMC@NLO [120] at NLO with  
<sub>1181</sub> the NNPDF3.0nlo [121] PDF set, interfaced with PYTHIA8.230 [122] using A14 tune [123] and  
<sub>1182</sub> NNPDF2.3l0 PDF set. Sample for  $m_{\ell\ell} < 5$  GeV was produced with SHERPA v2.2.10 [128]  
<sub>1183</sub> at NLO using NNPDF3.0nnlo PDF set. To account for generator uncertainty, an alternative  
<sub>1184</sub>  $m_{\ell\ell} > 5$  GeV sample was generated with identical settings to the low  $m_{\ell\ell}$  sample. The  
<sub>1185</sub> ATLAS detector response was simulated with full detector simulation (FS).

<sub>1186</sub> **Chapter 6. Analysis Strategy**

<sub>1187</sub> **6.1 Event selection**

<sub>1188</sub> Events for the analysis first are preselected following a list of criteria to optimize for event  
<sub>1189</sub> quality and background rejection. The following criteria are applied sequentially from top  
<sub>1190</sub> to bottom along with cleaning and veto cuts

- <sub>1191</sub> 1. **Good Run List (GRL)**: data events must be part of a predefined list of suitable  
<sub>1192</sub> runs and luminosity blocks [[137](#)].
- <sub>1193</sub> 2. **Primary vertex**: events must have at least one reconstructed vertex matched to 2 or  
<sub>1194</sub> more associated tracks with  $p_T > 500$  MeV.
- <sub>1195</sub> 3. **Trigger**: events must be selected by at least one trigger in Table 5.1.
- <sub>1196</sub> 4. **Kinematic selection**: events must have exactly two *Tight* leptons with the same  
<sub>1197</sub> electric charge, or at least three *Tight* leptons of any charge. The leading lepton must  
<sub>1198</sub> have  $p_T > 28$  GeV, and all leptons must satisfy  $p_T > 15$  GeV.

<sub>1199</sub> Events are separated into two channels based on the number of leptons: same-sign di-  
<sub>1200</sub> lepton (SS2L) for events with exactly two leptons of the same charge, or multilepton (ML)  
<sub>1201</sub> for events with three or more leptons. The channels are further separated into regions defined  
<sub>1202</sub> in section 6.2 to prepare for analysis.

<sub>1203</sub> Additional selections are applied based on the lepton flavors present. In the SS2L channel,  
<sub>1204</sub> if both leptons are electrons, the invariant mass  $m_{ll}$  must satisfy  $m_{ll} < 81$  GeV and  $m_{ll} > 101$   
<sub>1205</sub> GeV to suppress background involving  $Z$ -bosons. In the ML channel, the same criteria must  
<sub>1206</sub> be satisfied for every opposite-sign same-flavor pair of leptons in an event.

### 1207 6.1.1 Event categorization

1208 Simulated events are categorized using truth information of leptons ( $e/\mu$ ) and their orig-  
1209 inating MC particle (mother-particle). Each lepton can be classified as either prompt or  
1210 non-prompt, with non-prompt leptons further categorized for background estimation pur-  
1211 poses. If an event contains only prompt leptons, the event is classified as its correspond-  
1212 ing process. If the event contains one non-prompt lepton, the event is classified as the corre-  
1213 sponding type of the non-prompt lepton. If the event contains more than one non-prompt  
1214 lepton, the event is classified as other.

1215 • **Prompt:** if the lepton originates from  $W/Z/H$  boson decays, or from a mother-  
1216 particle created by a final state photon.

1217 • **Non-prompt:**

1218 – **Charge-flip ( $e$  only):** if the reconstructed charge of the lepton differs from that  
1219 of the first mother-particle.

1220 – **Material conversion ( $e$  only):** if the lepton originated from a photon conversion  
1221 and the mother-particle is an isolated prompt photon, non-isolated final state  
1222 photon, or heavy boson.

1223 –  **$\gamma^*$ -conversion ( $e$  only):** if the lepton originated from a photon conversion and  
1224 the mother-particle is a background electron.

1225 – **Heavy flavor decay:** if the lepton originated from a  $b$ - or  $c$ -hadron.

1226 – **Fake:** if the lepton originated from a light- or  $s$ -hadron, or if the truth type of  
1227 the lepton is hadron.

1228 – **Other:** any lepton that does not belong to one of the above categories.

## 1229 6.2 Analysis regions

1230 Events are selected and categorized into analysis regions belonging to one of two types:  
1231 control regions (CRs) enriched in background events, and signal regions (SRs) enriched in  
1232 signal events. This allows for the examination and control of backgrounds and systematic  
1233 uncertainties, as well as study of signal sensitivities. The signal is then extracted from  
1234 the SRs with a profile LH fit using all regions. The full selection criteria for each region are  
1235 summarized in Table 6.1. The background compositions in different CRs and SR sub-regions  
1236 are shown in Figure 6.1.

### 1237 6.2.1 Signal regions

1238 All events selected for the SR must satisfy the following criteria:

- 1239 • Contains 6 or more jets, with at least 2 jets  $b$ -tagged at the 85% OP.
- 1240 • Scalar sum of the transverse momenta of all leptons and jets  $H_T > 500$  GeV.
- 1241 • Dilepton invariant mass  $m_{\ell\ell}$  does not coincide with the  $Z$ -boson mass range of 81 – 101  
1242 GeV

1243 The SR is further divided into sub-regions by the number of  $b$ -tagged jets and leptons  
1244 present to study signal behavior and sensitivity with respect to the selection variables.

### 1245 Signal extraction

1246 Signal extraction in the SR is performed via a binned profile likelihood (LH) fit as de-  
1247 scribed in section 8.1 using  $H_T$  as the discriminant observable. The discriminant observable

Table 6.1: Definitions of signal, control and validation regions (VR) used in this analysis.  $N_{\text{jets}}$  and  $N_b$  refers to the number of jets and number of  $b$ -tagged jets respectively.  $\ell_1$  refers to the leading lepton,  $\ell_2$  refers to the subleading lepton and so on.  $H_T$  refers to the  $p_T$  scalar sum of all leptons and jets in the event.  $m_{\ell\ell}$  refers to the dilepton invariant mass, which must not coincide with the  $Z$ -boson mass range of 81-101 GeV for SS2L+3L events.

Region	Channel	$N_{\text{jets}}$	$N_b$	Other selections	Fitted variable
CR Low $m_{\gamma^*}$	SS $e\ell$	[4, 6)	$\geq 1$	$\ell_1/\ell_2$ is from virtual photon decay $\ell_1 + \ell_2$ not from material conversion	event yield
CR Mat. Conv.	SS $e\ell$	[4, 6)	$\geq 1$	$\ell_1/\ell_2$ is from material conversion $\ell_1 + \ell_2$ not conversion candidates	event yield
CR HF $\mu$	$\ell\mu\mu$	$\geq 1$	1	$100 < H_T < 300$ GeV $E_T^{\text{miss}} > 35$ GeV total charge = $\pm 1$	$p_T(\ell_3)$
CR HF $e$	$e\ell\ell$	$\geq 1$	1	$\ell_1 + \ell_2$ not conversion candidates $100 < H_T < 275$ GeV $E_T^{\text{miss}} > 35$ GeV total charge = $\pm 1$	$p_T(\ell_3)$
CR $t\bar{t}W^+$	SS $\ell\mu$	$\geq 4$	$\geq 2$	$ \eta(e)  < 1.5$ for $N_b = 2$ : $H_T < 500$ GeV or $N_{\text{jets}} < 6$ for $N_b \geq 3$ : $H_T < 500$ GeV total charge > 0	$N_{\text{jets}}$
CR $t\bar{t}W^-$	SS $\ell\mu$	$\geq 4$	$\geq 2$	$ \eta(e)  < 1.5$ for $N_b = 2$ : $H_T < 500$ GeV or $N_{\text{jets}} < 6$ for $N_b \geq 3$ : $H_T < 500$ GeV total charge < 0	$N_{\text{jets}}$
CR 1b(+)	SS2L+3L	$\geq 4$	1	$\ell_1 + \ell_2$ not from material conversion $H_T > 500$ GeV total charge > 0	$N_{\text{jets}}$
CR 1b(-)	SS2L+3L	$\geq 4$	1	$\ell_1 + \ell_2$ not from material conversion $H_T > 500$ GeV total charge < 0	$N_{\text{jets}}$
VR $t\bar{t}Z$	3L $\ell^\pm\ell^\mp$	$\geq 4$	$\geq 2$	$m_{\ell\ell} \in [81, 101]$ GeV	$N_{\text{jets}}, m_{\ell\ell}$
VR $t\bar{t}W +1b$	SS2L+3L			CR $t\bar{t}W^\pm$    CR 1b( $\pm$ )	$N_{\text{jets}}$
VR $t\bar{t}W +1b+SR$	SS2L+3L			CR $t\bar{t}W^\pm$    CR 1b( $\pm$ )    SR	$N_{\text{jets}}$
SR	SS2L+3L	$\geq 6$	$\geq 2$	$H_T > 500$ GeV $m_{\ell\ell} \notin [81, 101]$ GeV	$H_T$

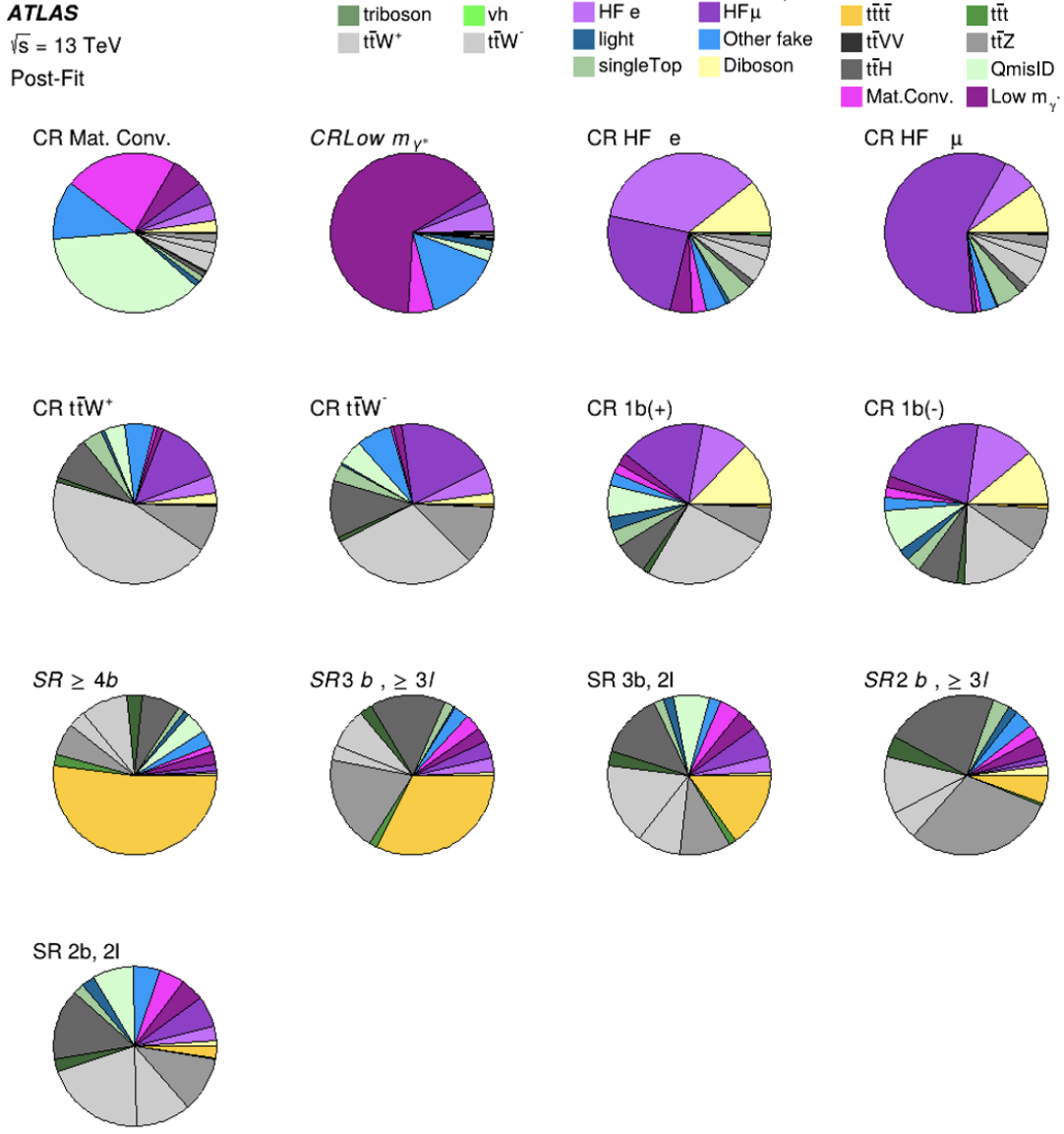


Figure 6.1: Post-fit background composition in each analysis region and sub-region. The fit was performed using ideal pseudo-datasets (Asimov data) in the SR.

<sub>1248</sub> for a LH fit serves as the set of observed data upon which the LH function is constructed.  
<sub>1249</sub> Ideally, the chosen observable shows significant separation between the functional forms of  
<sub>1250</sub> the signal and background distributions, allowing for effective separation of the two. Fig-  
<sub>1251</sub> ure 6.2 shows several pre-fit kinematic distributions in the inclusive SR. From empirical  
<sub>1252</sub> optimization studies,  $H_T$  possesses good discriminating power compared to other observ-

Table 6.2: Definitions of SR sub-regions. Events are sorted into different sub-regions based on the number of  $b$ -tagged jets and leptons present.

Sub-region	Selection criteria	
	$b$ -jets	leptons
SR 2b2l	$N_b = 2$	$N_l = 2$
SR 2b3l4l	$N_b = 2$	$N_l \geq 3$
SR 3b2l	$N_b = 3$	$N_l = 2$
SR 3b3l4l	$N_b = 3$	$N_l \geq 3$
SR 4b	$N_b \geq 4$	

1253 ables constructed using event-level information.

## 1254 6.2.2 Control regions

1255 Control regions are defined for each background to be enriched in the targeted process, in  
1256 order to maximize the background's purity and minimize contamination from other sources  
1257 within the region. This helps to constrain and reduce correlation between background nor-  
1258 malization factors in the final fit. Fit variables and selection criteria are determined via  
1259 optimization studies performed on CRs that aimed to achieve the largest discriminating  
1260 power possible between the target background and other event types.

### 1261 $t\bar{t}W$ background CRs

1262 Theoretical modeling for  $t\bar{t}W +$  jets background in the phase space of this analysis suffers  
1263 from large uncertainties, especially at high jet multiplicities [138]. A data-driven method was  
1264 employed in a similar manner to the SM  $t\bar{t}t\bar{t}$  observation analysis [44] to mitigate this effect,  
1265 and are described in further details in section 6.3.3. The method necessitates the definition  
1266 of two groups of dedicated CRs to estimate the flavor composition and normalization of  $t\bar{t}W$   
1267 + jets background: CR  $t\bar{t}W +$  jets to constrain flavor composition, and CR 1b to constrain

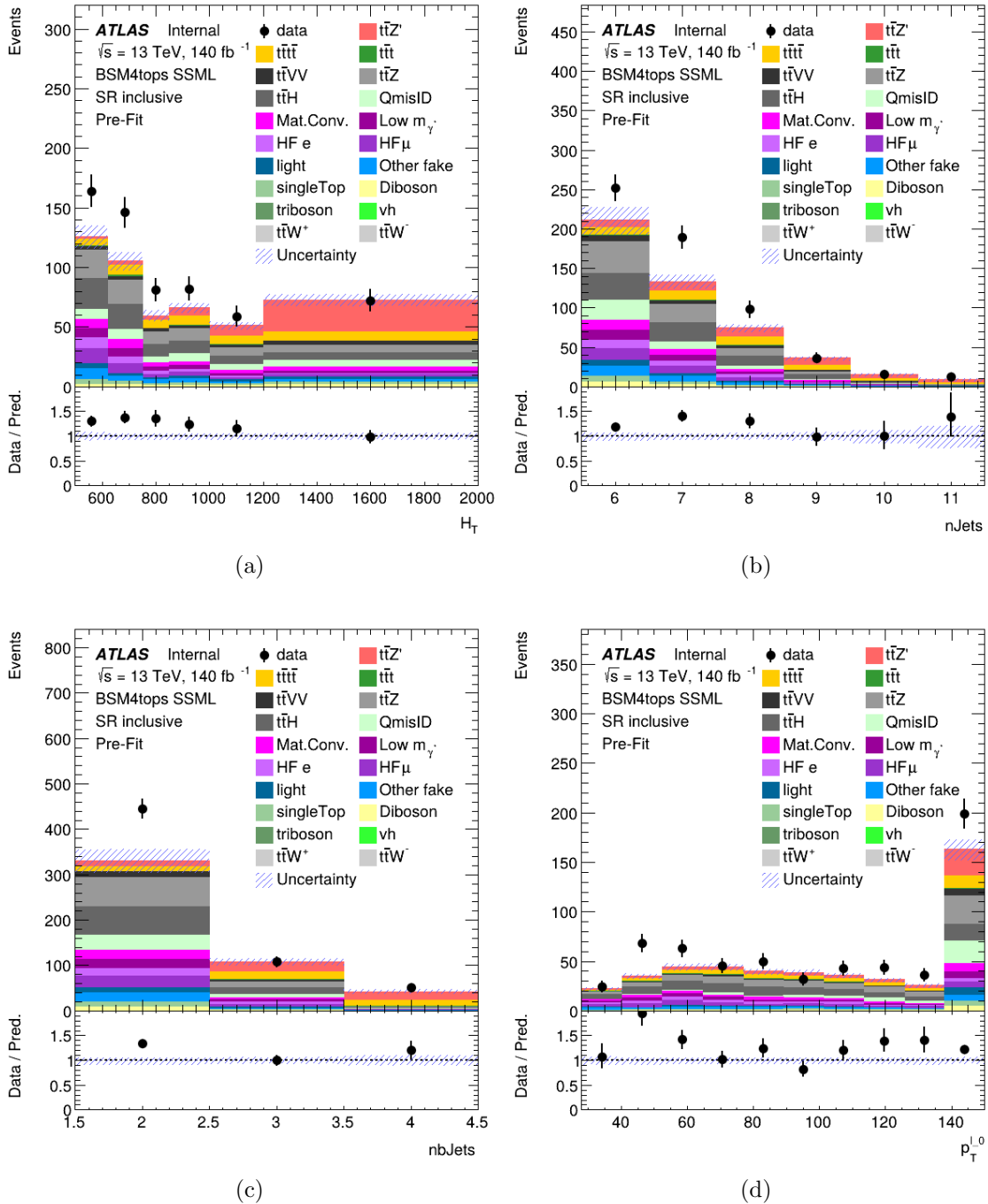


Figure 6.2: Pre-fit kinematic distributions and event compositions for several observables in the inclusive SR. The shaded band represents the uncertainty in the total distribution. The first and last bins of each distribution contain underflow and overflow events respectively.

- 1268 the jet multiplicity spectrum. These are further split into CR  $t\bar{t}W^\pm$  and CR 1b( $\pm$ ) due to  
 1269 the pronounced asymmetry in  $t\bar{t}W$  production from  $pp$  collisions, with  $t\bar{t}W^+$  being produced

1270 at approximately twice the rate of  $t\bar{t}W^-$  [139].

1271 Events in CR  $t\bar{t}W^\pm$  are required to contain at least two  $b$ -tagged jets similar to the SR  
1272 to determine the  $t\bar{t}W$  normalization within an SR-related phase space. Orthogonality with  
1273 SR is ensured by requiring  $H_T < 500$  GeV or  $N_{\text{jets}} < 6$  when  $N_b = 2$ , and  $H_T < 500$   
1274 GeV when  $N_b \geq 3$ . Events in CR 1b( $\pm$ ) are required to have  $H_T > 500$  GeV and at least  
1275 four jets to encompass events with high  $N_{\text{jets}}$ , which can be used to determine the  $t\bar{t}W$  jet  
1276 multiplicity spectrum for fitting  $a_{0,1}$ . The selection criteria also include exactly one  $b$ -tagged  
1277 jet to maintain orthogonality with the SR.

### 1278 **Fake/non-prompt background CRs**

1279 Selection for fake/non-prompt CRs are determined using the `DFCommonAddAmbiguity`  
1280 (DFCAA) variable for reconstructed leptons.

Table 6.3: List of possible assigned values for DFCAA.

DFCAA	Description
-1	No 2nd track found
0	2nd track found, no conversion found
1	Virtual photon conversion candidate
2	Material conversion candidate

1281 Four CRs are defined for the three main types of fake/non-prompt backgrounds in the  
1282 analysis - virtual photon ( $\gamma^*$ ) conversion, photon conversion in detector material (Mat.  
1283 Conv.) and heavy flavor decays (HF). The full selection criteria for fake/non-prompt CRs  
1284 are shown in Table 6.1.

1285 • **Low  $m_\gamma^*$ :** events with an  $e^+e^-$  pair produced from a virtual photon.

1286 Events are selected if there are two same-sign leptons with at least one electron recon-

1287       structured as an internal conversion candidate, and neither reconstructed as a material  
1288       conversion candidate.

- 1289     • **Mat. Conv.:** events with an electron originating from photon conversion within the  
1290       detector material.

1291       Events are selected if there are two same-sign leptons with at least one electron recon-  
1292       structed as a material conversion candidate.

- 1293     • **HF  $e(\mu)$ :** events with a reconstructed non-prompt lepton from semi-leptonic decays of  
1294        $b$ - and  $c$ -hadrons (heavy flavor decays).

1295       Events are selected if there are three leptons with at least two electrons (muons), with  
1296       no lepton reconstructed as a conversion candidate.

## 1297     6.3 Background estimation

1298       Background in this analysis consist of SM processes that can result in a signal signature  
1299       similar to a  $t\bar{t}t\bar{t}$  SSML final state and can be divided into two types, reducible and irre-  
1300       ducible. Reducible background consists of processes that do not result in a SSML final state  
1301       physically, but are reconstructed as such due to detector and reconstruction effects. Three  
1302       main types of reducible background are considered: charge misidentification (QmisID) and  
1303       fake/non-prompt leptons. Fake/non-prompt lepton backgrounds are estimated using tem-  
1304       plate fitting method, where MC simulations are normalized to their theoretical SM cross  
1305       section via floating normalization factors (NFs) constrained by the corresponding CRs. Lep-  
1306       ton charge misidentification background contaminates the SR with opposite-sign events, and  
1307       are estimated using a data-driven method described in section 6.3.2 along with ECIDS de-  
1308       scribed in section 4.3.1.

1309 Irreducible background consists of SM processes that result in SSML final states physi-  
1310 cally with all leptons being prompt. The dominating background in the SR are SM  $t\bar{t}t\bar{t}$ ,  $t\bar{t}W$ ,  
1311  $t\bar{t}Z$ , and  $t\bar{t}H$  production with smaller contributions from  $VV$ ,  $VVV$ ,  $VH$  and rarer processes  
1312 like  $t\bar{t}VV$ ,  $tWZ$ ,  $tZq$  and  $t\bar{t}t$ . Most irreducible backgrounds are estimated using template  
1313 fitting method, with the exception of  $t\bar{t}W + \text{jets}$  background. The  $t\bar{t}W + \text{jets}$  background is  
1314 instead given four dedicated CRs, and estimated using a data-driven method with a fitted  
1315 function parameterized in  $N_{\text{jets}}$ . All CRs and SR are included in the final profile LH fit to  
1316 data.

### 1317 6.3.1 Template fitting for fake/non-prompt estimation

1318 Template fitting method is a semi-data-driven approach [138] that estimates fake/non-  
1319 prompt background distributions by fitting the MC kinematic profile of background processes  
1320 arising from fake/non-prompt leptons to data. Each of the four main sources of fake/non-  
1321 prompt leptons is assigned a free-floating NF constrained by a CR enriched with the corre-  
1322 sponding background resulting in four  $\text{NF}_{\text{HF } e}$ ,  $\text{NF}_{\text{HF } \mu}$ ,  $\text{NF}_{\text{Mat. Conv.}}$  and  $\text{NF}_{\text{Low } m_{\gamma^*}}$ . The  
1323 NFs are fitted simultaneously with the signal.

### 1324 6.3.2 Charge misidentification data-driven estimation

1325 The  $ee$  and  $e\mu$  channels in the SS2L region are contaminated with opposite-sign (OS)  
1326 dilepton events with one misidentified charge. Charge misidentification (QmisID) largely  
1327 affects electrons due to muons' precise curvature information using ID and MS measurements  
1328 and low bremsstrahlung rate. The charge flip rates are significant at higher  $p_T$  and varies  
1329 with  $|\eta|$  which is proportional to the amount of detector material the electron interacted

1330 with.

1331 The charge flip probability  $\epsilon$  is estimated in this analysis with a data-driven method  
1332 [140] using a sample of  $Z \rightarrow e^+e^-$  events with additional constraints on the invariant mass  
1333  $m_{ee}$  to be within 10 GeV of the  $Z$ -boson mass. The  $Z$ -boson mass window is defined to  
1334 be within  $4\sigma$  to include most events within the peak, and is determined by fitting the  $m_{ee}$   
1335 spectrum of the two leading electrons to a Breit-Wigner function, resulting in a range of  
1336 [65.57, 113.49] for SS events and [71.81, 109.89] for OS events. Background contamination  
1337 near the peak is assumed to be uniform and subtracted using a sideband method. Since the  
1338  $Z$ -boson decay products consist of a pair of opposite-sign electrons, all same-sign electron  
1339 pairs are considered affected by charge misidentification.

1340 Let  $N_{ij}^{\text{SS}}$  be the number of events with SS electrons with the leading electron in the  
1341  $i^{\text{th}}$  2D bin in  $(p_T, |\eta|)$  and the sub-leading electron in the  $j^{\text{th}}$  bin. Assuming the QmisID  
1342 probabilities of electrons in an event are uncorrelated,  $N_{ij}^{\text{SS}}$  can be estimated as

$$N_{ij}^{\text{SS}} = N_{ij}^{\text{tot}} [\epsilon_i(1 - \epsilon_j) + \epsilon_j(1 - \epsilon_i)], \quad (6.1)$$

1343 where  $N_{ij}^{\text{tot}}$  is the total number of events in the  $i^{\text{th}}$  and  $j^{\text{th}}$  bin regardless of charge, and  
1344  $\epsilon_{i(j)}$  is the QmisID rate in the  $i^{\text{th}}(j^{\text{th}})$  bin. Assuming  $N_{ij}^{\text{SS}}$  follows a Poisson distribution  
1345 around the expectation value  $\bar{N}_{ij}^{\text{SS}}$ , the  $(i, n)^{\text{th}}$  rate  $\epsilon$  can be estimated by minimizing a  
1346 negative-LLH function parameterized in  $p_T$  and  $|\eta|$ ,

$$\begin{aligned}
-\ln(\mathcal{L}(\epsilon|N_{\text{SS}})) &= -\ln \prod_{ij} \frac{(N_{ij}^{\text{tot}})^{N_{ij}^{\text{SS}}} \cdot e^{N_{ij}^{\text{tot}}}}{N_{ij}^{\text{SS}}!} \\
&= -\sum_{ij} \left[ N_{ij}^{\text{SS}} \ln(N_{ij}^{\text{tot}}(\epsilon_i(1-\epsilon_j) + \epsilon_j(1-\epsilon_i))) - N_{ij}^{\text{tot}}(\epsilon_i(1-\epsilon_j) + \epsilon_j(1-\epsilon_i)) \right]. \tag{6.2}
\end{aligned}$$

1347 The QmisID rates are then calculated separately for SR and CRs with different electron  
 1348 definitions i.e. CR Low  $m_{\gamma^*}$ , CR Mat. Conv., CR  $t\bar{t}W^\pm$ , using events from data after  
 1349 applying region-specific lepton selections and ECIDS. The events are required to satisfy  
 1350 SS2L kinematic selections but contains OS electrons. The following weight is applied to OS  
 1351 events to correct for misidentified SS events within the region,

$$w = \frac{\epsilon_i + \epsilon_j - 2\epsilon_i\epsilon_j}{1 - \epsilon_i - \epsilon_j + 2\epsilon_i\epsilon_j}. \tag{6.3}$$

1352 The QmisID rates calculated for SR and CR  $t\bar{t}W$  are shown in Figure 6.3

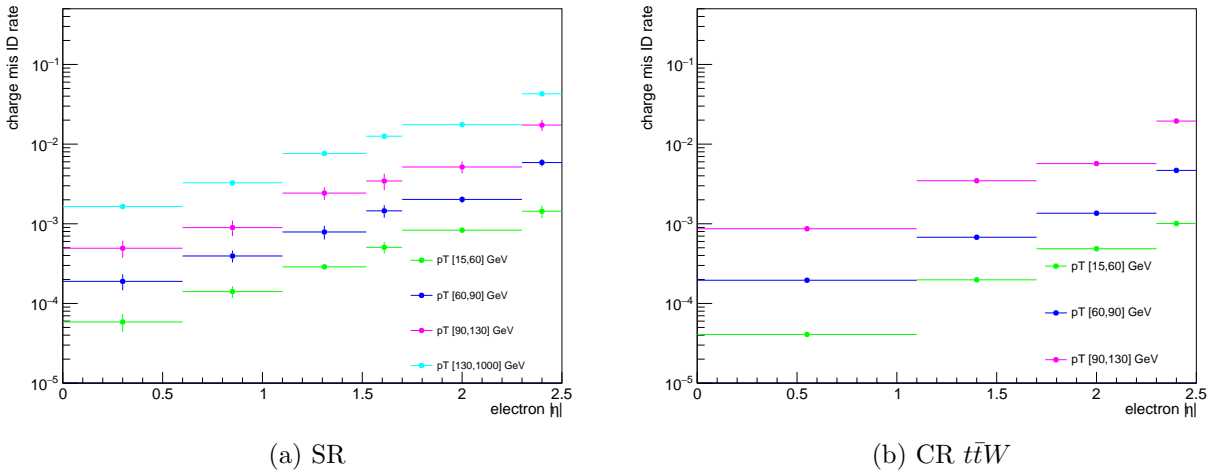


Figure 6.3: Charge flip rate calculated for SR and CR  $t\bar{t}W$  in bins of  $|\eta|$  and  $p_T$ .

1353        The QmisID rates obtained after applying  $w$  contain a dependency on jet multiplicity  
 1354        and are underestimated at higher  $N_{\text{jets}}$ . This dependency affect the SR which require events  
 1355        with  $\geq 6$  jets, and is corrected by applying a correction factor  $SF_{i,n} = \epsilon_{i,n}/\epsilon_{i,N}$  where  $N$  is  
 1356        the inclusive bin containing all  $N_{\text{jets}}$  and  $\epsilon_{i,n}$  is the QmisID rate obtained from Equation 6.2  
 1357        in the  $(i, n)^{\text{th}}$  2D bin in  $(p_{\text{T}}, N_{\text{jets}})$ . Jet multiplicity and consequently the obtained SFs are  
 1358        assumed to be independent of  $|\eta|$ .

### 1359        6.3.3 $t\bar{t}W$ background data-driven estimation

1360        Previously, the  $t\bar{t}W$  background in  $t\bar{t}t\bar{t}$  final state analysis was handled by assigning large  
 1361        ad-hoc systematic uncertainties to  $t\bar{t}W$  events with 7 or more jets [46]. A semi-data-driven  
 1362        method [141] was shown to be effective in the SM  $t\bar{t}t\bar{t}$  observation analysis [44] by improving  
 1363         $t\bar{t}W$  modeling, especially in the showering step and switching  $t\bar{t}W$  systematic uncertainties  
 1364        from predominantly modeling to statistical.

1365        The data-driven method applies correction factors obtained from a fitted function pa-  
 1366        rameterized in  $N_{\text{jets}}$  to  $t\bar{t}W$  MC kinematic distibutions. The QCD scaling patterns [142] can  
 1367        be represented by ratio of successive exclusive jet cross-sections

$$R_{(n+1)/n} = \frac{\sigma_{n+1}}{\sigma_n} = e^{-b} + \frac{\bar{n}}{n+1} = a_0 + \frac{a_1}{1+(j-4)}, \quad (6.4)$$

1368        where  $a_{0(1)}$  and  $b$  are constants,  $n$  is the number of jets in addition to the hard process,  $j$   
 1369        is the inclusive number of jets, and  $\bar{n}$  is the expectation value for the Poisson distribution  
 1370        of exclusive jet cross-section at jet multiplicity  $n$ . The  $t\bar{t}W$  ME for SS2L events gives 4 jets  
 1371        in the hard process, so  $n$  is defined starting from the 5<sup>th</sup> jets and the inclusive number of  
 1372        jets  $j = n + 4$ . The two terms in Equation 6.4 correspond to staircase and Poisson scaling

1373 in cross section between successive jet multiplicities and are sensitive to high and low jet  
 1374 multiplicity events respectively [142]. The scaling pattern can then be reparameterized in  
 1375  $a_0$  and  $a_1$  to obtain the  $t\bar{t}W$  yield at  $j' \equiv j + 1$  jets

$$\text{Yield}_{t\bar{t}W(j')} = \text{Yield}_{t\bar{t}W(N_{\text{jets}}=4)} \times \prod_{j=4}^{j'-1} \left( a_0 + \frac{a_1}{1+(j-4)} \right) \quad (6.5)$$

1376 with  $j \geq 4$ . The  $t\bar{t}W$  yield in the 4-jet bin can be represented by a NF applied to  $t\bar{t}W$  MC  
 1377 simulation

$$\text{Yield}_{t\bar{t}W(N_{\text{jets}}=4)} = \text{NF}_{t\bar{t}W(N_{\text{jets}}=4)} \times \text{MC}_{t\bar{t}W(N_{\text{jets}}=4)}. \quad (6.6)$$

1378 To account for the asymmetry in  $t\bar{t}W^+$  and  $t\bar{t}W^-$  cross-sections,  $\text{NF}_{t\bar{t}W(N_{\text{jets}}=4)}$  is further  
 1379 split into  $\text{NF}_{t\bar{t}W^\pm(N_{\text{jets}}=4)}$  assuming the scaling is the same for both processes. Both NFs  
 1380 are left free-floating to constrain  $t\bar{t}W$  yields in the 4-jet bin within CR 1b(+) and CR 1b(-).  
 1381 The final  $N_{\text{jets}}$ -parameterized function can then be represented by  $\text{NF}_{t\bar{t}W(j')}$  as

$$\text{NF}_{t\bar{t}W(j')} = \left( \text{NF}_{t\bar{t}W^+(N_{\text{jets}}=4)} + \text{NF}_{t\bar{t}W^-(N_{\text{jets}}=4)} \right) \times \prod_{j=4}^{j'-1} \left( a_0 + \frac{a_1}{1+(j-4)} \right). \quad (6.7)$$

1382 The normalization is calculated and applied separately for each sub-sample of  $t\bar{t}W^+$  and  
 1383  $t\bar{t}W^-$  in a  $N_{\text{jets}}$  bin for  $4 \leq N_{\text{jets}} < 10$ . Due to small contributions in the CRs, events  
 1384 with  $N_{\text{jets}} < 4$  and  $N_{\text{jets}} \geq 10$  are not normalized with this scheme. Instead,  $N_{\text{jets}} < 4$   
 1385 events are fitted by propagating the normalization in the 4-jet bin without additional shape  
 1386 correction. The correction factor for  $t\bar{t}W$  events with  $N_{\text{jets}} \geq 10$  is obtained by summing  
 1387 up the overflow from  $N_{\text{jets}} = 10$  to  $N_{\text{jets}} = 12$ , described as  $\sum_{j'=10}^{12} \prod_{j=4}^{j'-1} \left( a_0 + \frac{a_1}{1+(j-4)} \right)$ .  
 1388 Events with  $N_{\text{jets}} \geq 13$  are negligible and are not included in the sum.

1389      The four regions, CR  $t\bar{t}W^\pm$  and CR 1b( $\pm$ ), are constructed to fit  $NF_{t\bar{t}W^\pm(N_{\text{jets}}=4)}$  and  
1390 the scaling parameters  $a_{0(1)}$ , as well as validating the parameterization. Assuming the  $N_{\text{jets}}$   
1391 distribution of  $t\bar{t}W$  is similar across bins of  $N_b$ -jets, a fitted  $N_{\text{jets}}$  distribution in CR 1b( $\pm$ )  
1392 can be used to describe the  $t\bar{t}W$  parameterization at higher  $N_{\text{jets}}$ .

# 1393 Chapter 7. Systematic Uncertainties

1394 Physics analysis inherently incurs uncertainties in the form of statistical and systematic  
1395 uncertainties, depending on the source. Statistical uncertainties occur in this analysis from  
1396 sample size of collected data and simulated MC samples, and from the maximizing of the  
1397 LH function. Systematic uncertainties depend on identifiable sources in the analysis i.e.  
1398 from detector and reconstruction effects (experimental uncertainties) or theoretical modeling  
1399 (theoretical uncertainties). Systematic uncertainties are represented as nuisance parameters  
1400 ( $NP_x$ ) in the profile LH fit. During the fit, systematic uncertainties with negligible impact  
1401 on the final results can be pruned to simplify the statistical model and reduce computational  
1402 complexity. This section outlines all uncertainties considered in this analysis.

## 1403 7.1 Experimental uncertainties

### 1404 7.1.1 Luminosity & pile-up reweighting

1405 The uncertainty on the integrated luminosity of the 2015-2018 Run 2 data set is 0.83%  
1406 [87], obtained by the LUCID-2 detector [143] for the primary luminosity measurements and  
1407 complemented by the ID and calorimeters. Pile-up was modeled in MC and calibrated  
1408 to data through pile-up reweighting, resulting in a set of calibration SFs and associated  
1409 uncertainties.

### 1410 7.1.2 Leptons

1411 In general, calibrating MC simulations to match performance in data incurs uncertainties  
1412 associated obtaining the MC-to-data calibration SFs, which are in turn propagated to observ-

Table 7.1: Summary of the experimental systematic uncertainties considered in this analysis.

Systematic uncertainty	Components
<b>Event</b>	
Luminosity	1
Pile-up reweighting	1
<b>Electrons</b>	
Trigger efficiency	1
Reconstruction efficiency	1
Identification efficiency	1
Isolation efficiency	1
Energy scale	1
Energy resolution	1
Charge identification (ECIDS) efficiency	1
<b>Muons</b>	
Trigger efficiency	2
Track-to-vertex association efficiency	2
Reconstruction/identification efficiency	2
Low- $p_T$ ( $< 15$ GeV) reconstruction/identification efficiency	2
Isolation efficiency	2
Charge-independent momentum scale	1
Charge-dependent momentum scale	4
Energy resolution (CB)	1
Energy resolution (ID & MS)	2
<b>Jets</b>	
JES effective NP	15
JES $\eta$ intercalibration	3
JES flavor composition	2
JES flavor response	1
JES pile-up	4
JES punch-through (FS/AF3)	2
JES non-closure	1
JES high- $p_T$ single particle	1
JES $b$ -jet response	1
JER effective NP	12
JER data/MC (FS/AF3)	2
JVT efficiency	1
GN2v01 $b$ -tagging efficiency	85
GN2v01 $c$ -tagging efficiency	56
GN2v01 light-tagging efficiency	42
<b><math>E_T^{\text{miss}}</math> track-based soft terms</b>	
Transversal resolution	1
Longitudinal resolution	1
Longitudinal energy scale	1

ables in the analysis. The data-to-MC calibration of trigger, reconstruction, identification and isolation efficiencies for electrons and muons incur associated uncertainties, with separate systematic and statistical components for those related to muons. Similarly, electron energy scale, muon momentum scale and resolution are also subjected to calibration uncertainties estimated by re-simulating the events while varying the energy/momenta scale and resolution. Electron has an additional uncertainty related to ECIDS efficiency. Muon has additional uncertainties for charge-independent and charge-dependent momentum scale, as well as detector-specific track resolution. Systematic uncertainties for electron reconstruction, identification, isolation, ECIDS efficiencies and muon ID/MS energy resolution were not ready for the sample version used in this analysis, and are therefore not included.

### 7.1.3 Jets

Experimental uncertainties for jets are dominated by flavor tagging-related uncertainties, with subleading contributions from uncertainties related to JES [110], JER [109] and JVT [144] calibrations.

#### Jet energy scale

Uncertainties associated with JES are determined using data from LHC collisions along with MC simulated samples [110], decomposed into uncorrelated components:

- **Effective NPs:** 15 total  $p_T$ -dependent uncertainty components measured in situ, grouped based on their origin (2 detector-related, 4 modeling-related, 3 mixed, 6 statistical-related)
- **$\eta$  intercalibration:** 6 total components (1 modeling-related, 4 non-closure and 1

1434 statistical-related) associated with the correction of the forward jets' ( $0.8 \leq |\eta| < 4.5$ )  
1435 energy scale to that of the central jets ( $|\eta| < 0.8$ ).

1436 • **Flavor composition & response:** 2 components for relative quark-gluon flavor com-  
1437 positions in background and signal samples, and 2 components for responses to gluon-  
1438 initiated versus quark-initiated jets.

1439 • **Pile-up subtraction:** 4 components, 2 for  $\mu$  (`OffsetMu`) and  $N_{\text{PV}}$  (`OffsetNPV`) mod-  
1440 eling, 1 for residual  $p_{\text{T}}$ -dependency (`PtTerm`) and 1 for topology dependence on the  
1441 per-event  $p_{\text{T}}$  density modeling (`RhoTopology`).

1442 • **Punch-through effect treatment:** 2 terms for GSC punch-through jet response  
1443 deviation between data and MC, one for each detector response simulation method  
1444 (AF3 and FS).

1445 • **Non-closure:** 1 term applied to AF3 sample to account for the difference between  
1446 AF3 and FS simulation.

1447 • **High- $p_{\text{T}}$  single-particle response:** 1 term for the response to high- $p_{\text{T}}$  jets from  
1448 single-particle and test-beam measurements.

1449 •  **$b$ -jets response:** 1 term for the difference between  $b$ -jets and light-jets response.

## 1450 **Jet energy resolution**

1451 Measurements of JER were performed in bins of  $p_{\text{T}}$  and  $\eta$ , separately in data using in-  
1452 situ techniques and in MC simulation using dijet events [109]. This analysis uses the full  
1453 correlation JER uncertainty scheme provided for Run 2 analysis with 14 total components:

<sub>1454</sub> 12 for effective NPs and 2 for difference between data and MC, separately for AF3 and FS

<sub>1455</sub> [109].

#### <sub>1456</sub> **Jet vertex tagging**

<sub>1457</sub> The uncertainty associated with JVT is obtained by varying the JVT efficiency SFs

<sub>1458</sub> within their uncertainty range [144]. This uncertainty accounts for remaining contamination

<sub>1459</sub> from pile-up jets after applying pile-up suppression and MC generator choice.

#### <sub>1460</sub> **Flavor tagging**

<sub>1461</sub> Calibration SFs for  $b$ -tagging efficiencies and  $c$ -/light-jets mistagging rates are derived as

<sub>1462</sub> a function of  $p_T$  for  $b$ -,  $c$ -, light-jets and PCBT score. The full set of flavor tagging-related

<sub>1463</sub> uncertainties was reduced in dimensions by diagonalizing the uncertainty covariance matrix

<sub>1464</sub> via eigendecomposition [113], resulting in a compact set of orthogonal NPs for this analysis:

<sub>1465</sub> 85 for  $b$ -jets, 56 for  $c$ -jets and 42 for light-jets.

#### <sub>1466</sub> **7.1.4 Missing transverse energy**

<sub>1467</sub> Uncertainties on  $E_T^{\text{miss}}$  arise from possible mis-calibration of the soft-track component

<sub>1468</sub> and are estimated using data-to-MC comparison of the  $p_T$  scale and resolution between

<sub>1469</sub> the hard and soft  $E_T^{\text{miss}}$  components [118]. These uncertainties are represented by three

<sub>1470</sub> independent terms: 1 for scale uncertainty and 2 for resolution uncertainty of the parallel

<sub>1471</sub> and perpendicular components.

<sub>1472</sub> **7.2 Modeling uncertainties**

<sub>1473</sub> **7.2.1 Signal and irreducible background uncertainties**

<sub>1474</sub> The signal and background samples used are modeled using MC simulation. Most uncer-  
<sub>1475</sub> tainties on simulation parameters (e.g. generator choice, PS model) are estimated by varying  
<sub>1476</sub> the relevant parameters and comparing them with the nominal sample. Uncertainties in-  
<sub>1477</sub> volving PDF in particular for most processes in the analysis are set to a flat 1% uncertainty.  
<sub>1478</sub> Cross-section uncertainties were considered for all irreducible background except  $t\bar{t}W$ , which  
<sub>1479</sub> is normalized in dedicated CRs following section 6.3.3. Extra uncertainties for the produc-  
<sub>1480</sub> tion of four or more  $b$ -jets (additional  $b$ -jets) in association with  $t\bar{t}X$  and HF jets were also  
<sub>1481</sub> considered due to a lack of theoretical predictions or dedicated measurements, rendering  
<sub>1482</sub> MC modeling challenging. Uncertainties from missing higher-order QCD corrections in MC  
<sub>1483</sub> simulation are estimated by varying the renormalization scale  $\mu_R$  and factorization scale  $\mu_F$   
<sub>1484</sub> within seven different combinations

$$(\mu_R, \mu_F) = \{(0.5, 0.5), (0.5, 1), (1, 0.5), (1, 1), (1, 2), (2, 1), (2, 2)\}.$$

<sub>1485</sub> Process-specific uncertainty treatments are detailed below.

<sub>1486</sub> **SM  $t\bar{t}t\bar{t}$  background**

<sub>1487</sub> The generator uncertainty for the SM  $t\bar{t}t\bar{t}$  background was evaluated between a nominal  
<sub>1488</sub> sample of MADGRAPH5\_AMC@NLO and SHERPA. The parton shower uncertainty was  
<sub>1489</sub> evaluated between PYTHIA8 and HERWIG. The cross-section uncertainty was estimated to

1490 be 20% computed from a prediction at NLO in QCD+EW [127].

### 1491 $t\bar{t}t$ background

1492 The cross-section uncertainty for  $t\bar{t}t$  was estimated to be 30% computed from a prediction  
1493 at NLO in QCD+EW [127]. Events with additional  $b$ -jets also incur a 50% uncertainty.

### 1494 $t\bar{t}W$ , $t\bar{t}Z$ , $t\bar{t}H$ backgrounds

1495 For  $t\bar{t}W$ ,  $t\bar{t}Z$  and  $t\bar{t}H$  backgrounds, an uncertainty of 50% is assigned to events with one  
1496 additional truth  $b$ -jets that did not originate from a top quark decay, and an added 50%  
1497 uncertainty is assigned to events with two or more [145] additional  $b$ -jets. The generator  
1498 uncertainty was estimated for  $t\bar{t}Z$  using a MADGRAPH5\_AMC@NLO nominal sample and  
1499 a SHERPA sample, and for  $t\bar{t}H$  using POWHEGBOX samples interfaced with PYTHIA8 (nom-  
1500 inal) and HERWIG7. Cross-section uncertainties of 12% and 10% were applied to  $t\bar{t}Z$  and  
1501  $t\bar{t}H$  respectively [146]. No  $t\bar{t}W$  cross-section or PDF uncertainty was considered since the  
1502 normalizations and jet multiplicity spectrum for  $t\bar{t}W$  are estimated using the data-driven  
1503 method described in section 6.3.3.

### 1504 Other backgrounds

1505 Other backgrounds include processes with small overall contribution in the SR. The  
1506 cross-section uncertainty for  $tZ$  and  $tWH$  is considered to be 30% [147, 148]. A conservative  
1507 cross-section uncertainty of 50% is applied to  $t\bar{t}VV$ ,  $VVV$  and  $VH$ . For  $VV$ , the cross-  
1508 section uncertainty is dependent on jet multiplicity and is considered to be 20%/50%/60%  
1509 for events with  $\leq 3/4 \geq 5$  jets [149]. For  $VV$ ,  $t\bar{t}VV$ ,  $VVV$  and  $VH$  events with additional  
1510 truth  $b$ -jets, an uncertainty of 50% is applied.

## 1511 7.2.2 Reducible background uncertainties

1512 Reducible backgrounds consist of  $t\bar{t}/V + \text{HF}$  jets and single top events. Reducible back-  
1513 ground has small contamination within the SR, thus uncertainties related to reducible back-  
1514 ground have minor impact. Treatment for reducible background in this analysis largely  
1515 follows Ref. [44], except for QmisID.

## 1516 Charge misidentification

1517 Uncertainties on the QmisID background originate from the charge flip rates obtained  
1518 using the data-driven method described in section 6.3.2. Four sources of uncertainty were  
1519 considered: statistical uncertainty from the maximum LLH estimation using Equation 6.2;  
1520 uncertainty from choice of the  $Z$ -mass window and sidebands; non-closure uncertainty de-  
1521 fined as the relative difference between the number of SS and OS events; and statistical  
1522 uncertainty from the  $N_{\text{jets}}$  dependency correction SFs. The combined uncertainties from  
1523 all four sources are calculated separately for each region involved in section 6.3.2, and are  
1524 treated as correlated across all regions. Figure 7.1 shows the uncertainty calculated for SR.

## 1525 Internal (low $\gamma^*$ ) and material conversion

1526 The normalization for internal and material conversion backgrounds are free parameters  
1527 in the fit, as a result the only uncertainties evaluated are from the shape of the distributions  
1528 used in the template fit method (see section 6.3.1). The uncertainties on internal (material)  
1529 conversion are estimated based on the difference between data and MC prediction in a region  
1530 enriched in  $Z + \gamma \rightarrow \mu^+\mu^- + e^+e^-$  events.

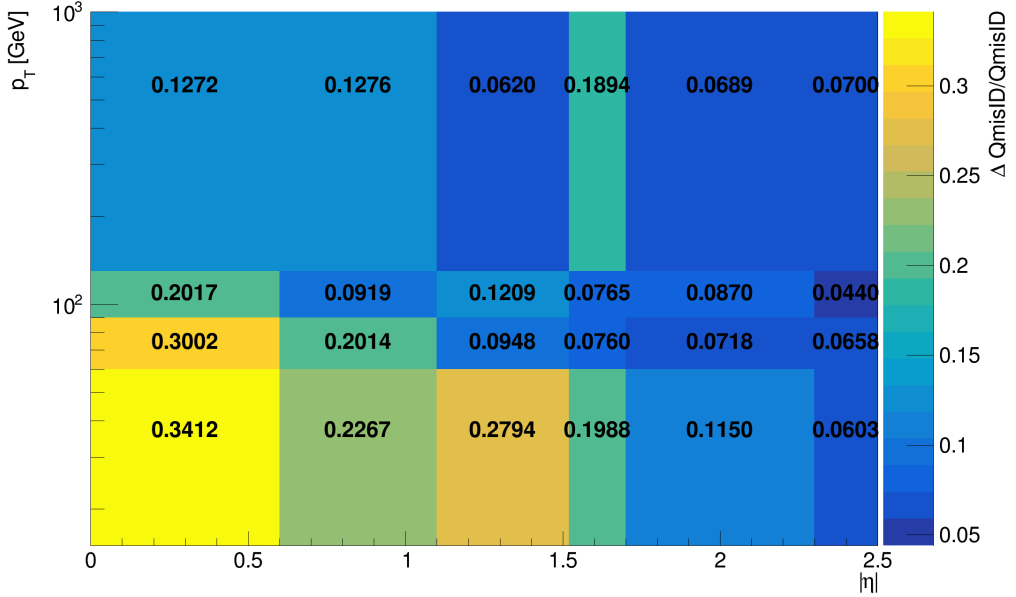


Figure 7.1: Combined QmisID uncertainty rate for SR in bins of  $|\eta|$  and  $p_T$ .

### 1531 Heavy-flavor non-prompt lepton

1532 Similar to the conversion backgrounds, the uncertainties on non-prompt HF decays come  
1533 from the shape of the distributions, and are estimated by comparing data and MC prediction  
1534 between all regions in the analysis on a per bin basis. The events used are required to  
1535 contain at least one *Loose* reconstructed lepton used in the region selection criteria detailed  
1536 in Table 6.1 to maintain orthogonality with the SR.

### 1537 Light-flavor decays and other fake/non-prompt backgrounds

1538 A conservative normalization uncertainty of 100% is assigned for light-flavor non-prompt  
1539 lepton background [138], and an ad-hoc normalization uncertainty of 30% is applied to all  
1540 other fake and non-prompt backgrounds. The shape uncertainties for these backgrounds are  
1541 negligible.

1542 **Chapter 8. Results**

1543 **8.1 Statistical interpretation**

1544 This section provides an overview of the statistical methods needed to interpret the  
1545 collected and simulated data to estimate unknown physics parameters and determine com-  
1546 patibility between data and the analysis hypothesis. For the BSM resonance search, the null  
1547 hypothesis  $H_0$  assumes only SM background contributions and none from any new BSM  
1548 resonance in the data.

1549 **8.1.1 Profile likelihood fit**

1550 Given a set of observed data points  $\mathbf{x} = [x_1, x_2, \dots]$  and unknown parameters  $\boldsymbol{\theta} =$   
1551  $[\theta_1, \theta_2, \dots, \theta_n]$ , the maximum likelihood method aims to find an estimate  $\hat{\boldsymbol{\theta}}$  that maximizes  
1552 the joint probability function  $f(\mathbf{x}, \boldsymbol{\theta})$ , or in other words the set of parameters that gives the  
1553 highest probability of observing the collected data points for a particular model. The func-  
1554 tion to be maximized for this purpose is the log-likelihood (LLH) function  $\ln \mathcal{L}(\mathbf{x}, \boldsymbol{\theta})$  where  
1555  $\mathcal{L}(\mathbf{x}, \boldsymbol{\theta}) \equiv \prod_i f(x_i, \boldsymbol{\theta})$  is defined as the likelihood (LH) function. The LLH is maximized  
1556 when  $\partial/\partial\theta_i (\ln \mathcal{L}) = 0$  for each parameter  $\theta_i$ .

1557 For an usual binned physics analysis, the above variables for the LH function  $\mathcal{L}$  can  
1558 be expressed as nuisance parameters (NP)  $\boldsymbol{\theta}$  and number of events for a model  $N_i(\mu)$  for  
1559 the  $i^{\text{th}}$  bin, where  $\mu$  is the targeted parameter of interest (POI). In this analysis,  $N_i$  is  
1560 assumed to follow a Poisson distribution and depends on the following quantities: the signal  
1561 strength  $\mu$  defined as the ratio of observed to expected cross sections  $\sigma_{\text{obs}}/\sigma_{\text{exp}}$ ; nuisance  
1562 parameters  $\boldsymbol{\theta}$  which represents the effects of systematic uncertainties, implemented in the

1563 LH function as Gaussian constraints; and normalization factors (NFs)  $\boldsymbol{\lambda}$  that control the  
 1564 normalization of background components that do not have a well-known cross section. The  
 1565 Poisson probability of observing exactly  $N_i$  events for an expected number of event  $n_i$  is

$$\mathcal{P}(N_i|n_i(\mu, \boldsymbol{\lambda})) = \frac{n_i^{N_i} e^{-n_i}}{N_i!}. \quad (8.1)$$

1566 The expected Poisson event number in a bin  $i$  can be parameterized as

$$n_i = \mu s_i(\boldsymbol{\theta}) + \sum_j \lambda_j b_{ij}(\boldsymbol{\theta}), \quad (8.2)$$

1567 where  $s_i$  is the number of signal events in bin  $i$  of every region, and  $b_{ij}$  is the number of  
 1568 events for a certain background source index  $j$  in bin  $i$ . The LH function in this analysis  
 1569 can be written as

$$\mathcal{L}(\mathbf{N}|\mu, \boldsymbol{\theta}, \boldsymbol{\lambda}) = \left( \prod_i \mathcal{P}(N_i|n_i) \right) \cdot \prod_k \mathcal{G}(\theta_k), \quad (8.3)$$

1570 where  $\mathcal{G}(\theta_k)$  is the Gaussian constraint for a NP  $k$ . The signal significance  $\mu$  and NFs  $\boldsymbol{\lambda}$  are  
 1571 left unconstrained and are fitted simultaneously in the profile LH fit. Define the profile LH  
 1572 ratio [150] as

$$\lambda(\mu) = \frac{\mathcal{L}(\mu, \hat{\boldsymbol{\theta}}_\mu, \hat{\boldsymbol{\lambda}}_\mu)}{\mathcal{L}(\hat{\mu}, \hat{\boldsymbol{\theta}}, \hat{\boldsymbol{\lambda}})}, \quad (8.4)$$

1573 where  $\hat{\mu}$ ,  $\hat{\boldsymbol{\theta}}$  and  $\hat{\boldsymbol{\lambda}}$  are parameter values that optimally maximizes the LH function, and  $\hat{\boldsymbol{\theta}}_\mu$ ,  
 1574  $\hat{\boldsymbol{\lambda}}_\mu$  are NP and NF values respectively that maximize the LH function for a given signal  
 1575 strength  $\mu$ . Using Neyman-Pearson lemma [151], the optimal test statistic for hypothesis  
 1576 testing is

$$q_\mu \equiv -2 \ln \lambda(\mu), \quad (8.5)$$

1577 where  $q_\mu = 0$  or  $\lambda(\mu) = 1$  corresponds to perfect agreement between the optimal parameter  
 1578  $\hat{\mu}$  obtained from data and the hypothesized value  $\mu$ . From Wilks' theorem [152], the test  
 1579 statistic  $q_\mu$  approaches a  $\chi^2$  distribution and can be evaluated as  $q_\mu = (\mu - \hat{\mu})^2 / \sigma_\mu^2$ .

1580 When evaluating against the background-only hypothesis ( $\mu = 0$ ), it can be assumed  
 1581 that the number of events observed under the signal hypothesis is higher than that of the  
 1582 background-only hypothesis, or  $\mu \geq 0$  according to Equation 8.2. This leads to a corre-  
 1583 sponding lower bound on the test statistic

$$q_0 = \begin{cases} -2 \ln \lambda(0), & \text{if } \hat{\mu} \geq 0, \\ 0, & \text{if } \hat{\mu} < 0. \end{cases} \quad (8.6)$$

### 1584 ***p*-value**

1585 To quantify the incompatibility between the observed data and the background-only hy-  
 1586 pothesis, the *p*-value is defined as  $p = P(q_\mu \geq q_{\mu, \text{obs}} | H_0)$  or in other words, the probability  
 1587 of observing data with a test statistic  $q_\mu$  under the null hypothesis  $H_0$  that is less compat-  
 1588 ible with  $H_0$  than the actual observed data with test statistic  $q_{\mu, \text{obs}}$ . The *p*-value can be  
 1589 expressed in terms of  $q_\mu$  as

$$p_\mu = \int_{q_{\mu, \text{obs}}}^{\infty} f(q_\mu | \mu) dq_\mu, \quad (8.7)$$

1590 where  $f(q_\mu | \mu) dq_\mu$  is the conditional probability density function of  $q_\mu$  given  $\mu$ .

1591 In some cases, it is more convenient to evaluate compatibility using the *Z*-value, defined  
 1592 as the number of standard deviations between the observed data and the mean in a Gaussian

1593 distribution. The  $p$ -value can be converted to  $Z$ -value via the relation

$$Z = \Phi^{-1}(1 - p), \quad (8.8)$$

1594 where  $\Phi$  is the quantile of the standard Gaussian. Rejecting the signal hypothesis usually  
1595 requires a 95% confidence level (CL) which corresponds to a  $p$ -value of 0.05 or a  $Z$ -value of  
1596 1.64, while rejecting the background-only hypothesis generally requires a  $Z$ -value of 5 or a  
1597  $p$ -value of  $2.84 \times 10^{-7}$ .

### 1598 8.1.2 Exclusion limit

1599 If the signal hypothesis is rejected, the exclusion upper limits can still be computed at  
1600 a certain CL (usually 95%) to establish the maximum value of  $\mu$  that is not excluded by  
1601 the observed data. The exclusion limits are calculated based on the  $\text{CL}_s$  method [153, 154]  
1602 under which the test statistic is defined as  $q_\mu = -2 \ln \frac{\mathcal{L}_{s+b}}{\mathcal{L}_b}$  with  $\mathcal{L}_{s+b}$  being the LH function  
1603 for the signal and background hypothesis ( $\mu > 0$ ) and  $\mathcal{L}_b$  being the LH function for the  
1604 background-only hypothesis ( $\mu = 0$ ). The  $p$ -value for both hypotheses can then be expressed  
1605 as

$$\begin{aligned} p_{s+b} &= P(q \geq q_{\text{obs}} | s + b) = \int_{q_{\text{obs}}}^{\infty} f(q | s + b) dq \\ p_b &= P(q \geq q_{\text{obs}} | b) = \int_{-\infty}^{q_{\text{obs}}} f(q | b) dq. \end{aligned} \quad (8.9)$$

1606 The signal hypothesis is excluded for a CL  $\alpha$  when the following condition is satisfied

$$\text{CL}_s \equiv \frac{p_{s+b}}{p_b} \geq 1 - \alpha. \quad (8.10)$$

<sub>1607</sub> The value of  $\mu$  such that the signal hypothesis leads to  $\text{CL}_s = 1 - \alpha = 0.05$  is then the  
<sub>1608</sub> exclusio upper limit at a 95% CL.

## <sub>1609</sub> 8.2 Fit results

<sub>1610</sub> The signal strength  $\mu$ , background NFs,  $t\bar{t}W$  scaling factors and uncertainty NPs are  
<sub>1611</sub> simultaneously fitted using a binned profile LLH fit under the background-only hypothesis  
<sub>1612</sub> to the  $H_T$  distribution in the SR and to corresponding distributions shown in Table 6.1 for  
<sub>1613</sub> CRs.

<sub>1614</sub> Before fitting to real data (unblinded fit), the fit was first performed in both the SR  
<sub>1615</sub> and CRs using Asimov pseudo-datasets, in which the simulated data match exactly to MC  
<sub>1616</sub> prediction with nominal  $\mu$  set to 0. This is done for the purpose of optimizing object selection  
<sub>1617</sub> criteria and region definition, refining background estimation techniques and testing the  
<sub>1618</sub> statistical interpretation model for signal extraction described in section 8.1. The fit is then  
<sub>1619</sub> performed with Asimov data in the SR and real data in CRs to validate background modeling,  
<sub>1620</sub> estimate sensitivity and assess the influence of statistical effects on fitted parameters. Finally,  
<sub>1621</sub> the fully unblinded fit is performed with real data in all regions.

<sub>1622</sub> The unblinded fit results are presented below. No significant excess over SM predictions  
<sub>1623</sub> is observed, and the fitted signal strength  $\mu$  is compatible with zero for all  $Z'$  mass points.  
<sub>1624</sub> Figure 8.1 shows the observed and expected upper limits at 95% confidence level on the  
<sub>1625</sub> cross-section of  $pp \rightarrow t\bar{t}Z'$  production times the branching ratio of  $Z' \rightarrow t\bar{t}$  as a function of  
<sub>1626</sub> the  $Z'$  resonance mass. The exclusion limits range from 7.9 fb to 9.44 fb depending on  $m_{Z'}$ .

<sub>1627</sub> The background modeling is evaluated under the background-only hypothesis. The fitted  
<sub>1628</sub> background NFs are shown in Table 8.1 and are consistent with their nominal values within

one standard deviation, or two standard deviations in the case of  $\text{NF}_{\text{HF } e}$  and  $\text{NF}_{t\bar{t}W^+(4j)}$ .  
 Figure 8.2 shows good agreement between data and post-fit background distributions in  
 non-prompt background CRs and  $t\bar{t}W$  CRs. The pre-fit and post-fit background yields  
 are shown in Table 8.2. **Discuss differences between pre and post-fit yields. Which one  
 increased/decreased? Why, NFs/NPs? Consistent with data within 1-2 stdev?**

Table 8.1: Normalization factors for backgrounds with dedicated CRs, obtained from a simultaneous fit in all CRs and SR under the background-only hypothesis. The nominal pre-fit value is 1 for all NFs and 0 for the scaling factors  $a_0$  and  $a_1$ . Uncertainties shown include both statistical and systematic uncertainties.

Parameter	$\text{NF}_{\text{HF } e}$	$\text{NF}_{\text{HF } \mu}$	$\text{NF}_{\text{Mat. Conv.}}$	$\text{NF}_{\text{Low } m_{\gamma^*}}$	$a_0$	$a_1$	$\text{NF}_{t\bar{t}W^+(4j)}$	$\text{NF}_{t\bar{t}W^-(4j)}$
Fit value	$0.68^{+0.23}_{-0.22}$	$0.97^{+0.17}_{-0.16}$	$0.97^{+0.31}_{-0.28}$	$0.97^{+0.23}_{-0.20}$	$0.39^{+0.11}_{-0.11}$	$0.42^{+0.25}_{-0.24}$	$1.21^{+0.18}_{-0.18}$	$1.10^{+0.26}_{-0.26}$

Table 8.3 shows the impact of various sources of uncertainty grouped by their corresponding category on the signal strength. **Largest sources of uncertainty? Why?**

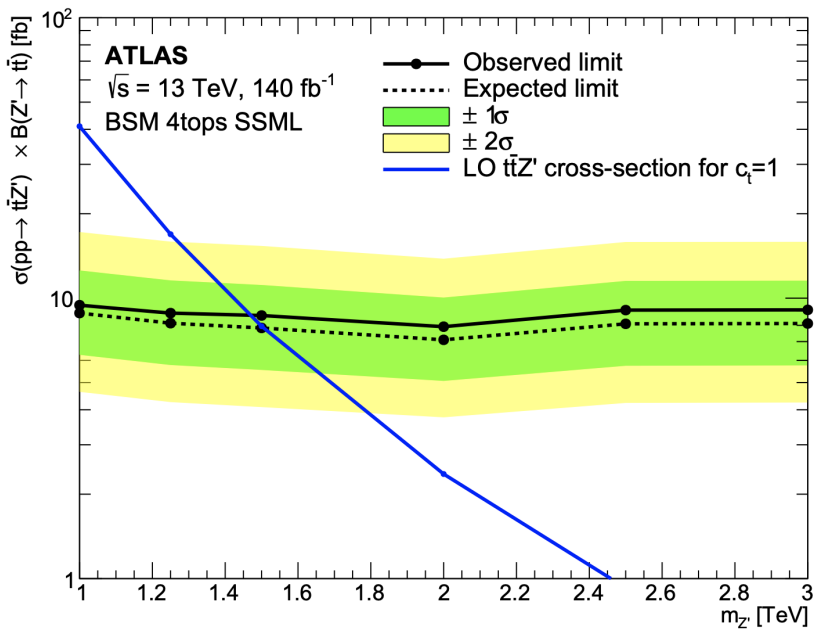


Figure 8.1: Observed (solid line) and expected (dotted line) upper limits as a function of the  $Z'$  mass at 95% CL on the cross-section of  $pp \rightarrow t\bar{t}Z'$  production times the  $Z' \rightarrow t\bar{t}$  branching ratio. The region above the observed limit is excluded. The solid blue line represents the theoretical signal cross-section with  $c_t = 1$  at LO in QCD [71]. The green and yellow bands represent the 68% ( $\pm\sigma$ ) and 95% ( $\pm 2\sigma$ ) confidence intervals respectively.

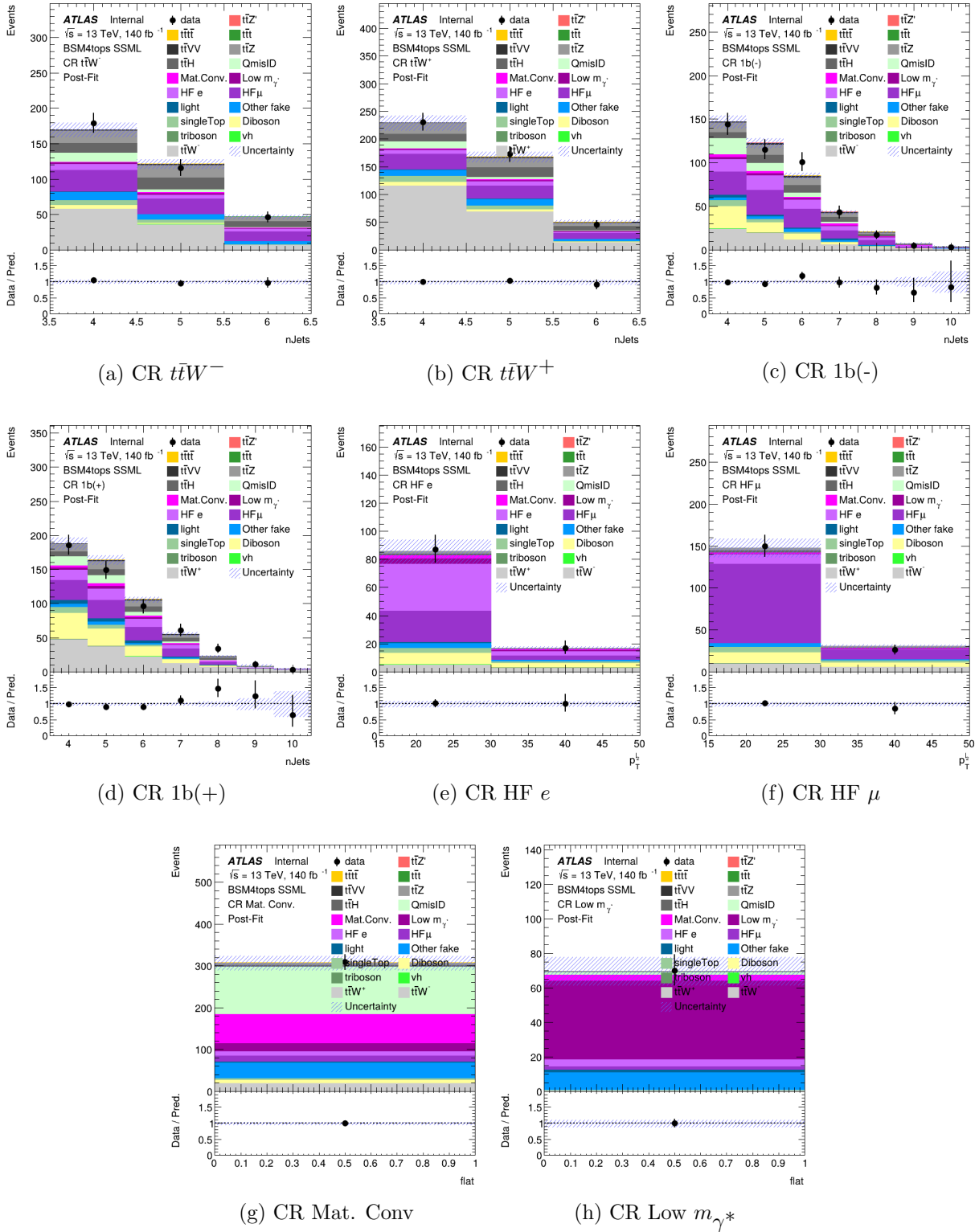


Figure 8.2: Comparison between data and post-fit prediction for the discriminant observable in each non-prompt and  $t\bar{t}W$  background CR. The fit is performed simultaneously in all CRs and SR under the background-only hypothesis. The lower panel shows the ratio between data and post-fit predictions. The shaded band represents the total uncertainty on the fit.

Table 8.2: Pre-fit and post-fit background yields in the inclusive SR. The number of data events and pre-fit estimate signal yields are also shown. Background yields shown are obtained from the fit using the  $t\bar{t}Z'$  signal sample with  $m_{Z'} = 2$  TeV. Total yield uncertainty differs from the quadrature sum of constituent uncertainties due to correlation and anticorrelation effects.

Process	Pre-fit	Post-fit
<b>Background</b>		
$t\bar{t}t\bar{t}$	$42.35 \pm 5.45$	$46.91 \pm 5.19$
$t\bar{t}W^+$	$97.38 \pm 0.71$	$103.93 \pm 15.91$
$t\bar{t}W^-$	$56.92 \pm 0.42$	$55.27 \pm 11.14$
$t\bar{t}Z$	$78.02 \pm 14.12$	$75.57 \pm 11.13$
$t\bar{t}H$	$81.00 \pm 7.10$	$82.90 \pm 7.30$
$t\bar{t}t$	$3.33 \pm 0.59$	$3.37 \pm 0.60$
Single-top ( $tq$ , $tZq$ , $tWZ$ , etc.)	$13.38 \pm 2.87$	$12.69 \pm 2.86$
$t\bar{t}VV/t\bar{t}VH/t\bar{t}HH$	$17.07 \pm 4.66$	$16.44 \pm 4.64$
Charge misidentification	$40.31 \pm 0.32$	$40.33 \pm 0.32$
$VV/VVV/VH$	$10.01 \pm 4.76$	$6.69 \pm 2.75$
Mat. Conv.	$26.20 \pm 0.91$	$25.76 \pm 6.06$
Low $m_{\gamma^*}$	$26.14 \pm 0.66$	$25.62 \pm 4.23$
HF $e$	$21.99 \pm 1.45$	$15.42 \pm 3.70$
HF $\mu$	$31.33 \pm 3.47$	$31.53 \pm 5.06$
Light-flavor decays	$13.47 \pm 0.53$	$13.54 \pm 0.53$
Other fake & non-prompt	$24.90 \pm 2.26$	$26.00 \pm 1.96$
Total background	$593.90 \pm 18.79$	$576.53 \pm 19.86$
<b>Signal <math>t\bar{t}Z' \rightarrow t\bar{t}t\bar{t}</math></b>		
$m_{Z'} = 1$ TeV	$52.83 \pm 1.41$	-
$m_{Z'} = 1.25$ TeV	$52.94 \pm 1.35$	-
$m_{Z'} = 1.5$ TeV	$53.07 \pm 1.47$	-
$m_{Z'} = 2$ TeV	$52.49 \pm 1.43$	-
$m_{Z'} = 2.5$ TeV	$53.07 \pm 1.47$	-
$m_{Z'} = 3$ TeV	$52.45 \pm 1.50$	-
<b>Data</b>	604	

Table 8.3: Post-fit impact of uncertainty sources on the signal strength  $\mu$ , grouped by categories. Values shown are obtained from the fit using the  $t\bar{t}Z'$  signal sample with  $m_{Z'} = 2$  TeV. Impact on  $\mu$  is evaluated for each uncertainty category by re-fitting with the corresponding set of NPs fixed to their best-fit values. Total uncertainty differs from the quadrature sum of constituent uncertainties due to correlation between NPs in the fit.

Uncertainty source	$\Delta\mu$	
<b>Signal modeling</b>		
$t\bar{t}Z'$	+0.00	-0.00
<b>Background modeling</b>		
$t\bar{t}\bar{t}$	+0.15	-0.13
$t\bar{t}W$	+0.04	-0.03
$t\bar{t}Z$	+0.02	-0.02
$t\bar{t}H$	+0.02	-0.02
Non-prompt leptons	+0.00	-0.00
Other backgrounds	+0.02	-0.02
<b>Instrumental</b>		
Luminosity	+0.00	-0.00
Jet uncertainties	+0.04	-0.04
Jet flavor tagging ( $b$ -jets)	+0.04	-0.04
Jet flavor tagging ( $c$ -jets)	+0.01	-0.01
Jet flavor tagging (light-jets)	+0.02	-0.01
MC simulation sample size	+0.01	-0.01
Other experimental uncertainties	+0.01	-0.01
Total systematic uncertainty	+0.15	-0.17
<b>Statistical</b>		
$t\bar{t}W$ NFs and scaling factors	+0.01	-0.01
Non-prompt lepton NFs (HF, Mat. Conv., Low $m_{\gamma^*}$ )	+0.00	-0.00
Total statistical uncertainty	+0.25	-0.23
<b>Total uncertainty</b>	+0.29	-0.29

1636 Chapter 9. Summary

# <sup>1637</sup> References

- <sup>1638</sup> [1] J. Schwinger. *On Quantum-Electrodynamics and the Magnetic Moment of the Elec-*  
<sup>1639</sup> *tron.* Phys. Rev. 73 (4 1948), pp. 416–417 (cit. on p. 1).
- <sup>1640</sup> [2] R. P. Feynman. *Space-Time Approach to Quantum Electrodynamics.* Phys. Rev. 76  
<sup>1641</sup> (6 1949), pp. 769–789 (cit. on p. 1).
- <sup>1642</sup> [3] S. Tomonaga. *On a relativistically invariant formulation of the quantum theory of*  
<sup>1643</sup> *wave fields.* Prog. Theor. Phys. 1 (1946), pp. 27–42 (cit. on p. 1).
- <sup>1644</sup> [4] E. Fermi. *An attempt of a theory of beta radiation. I.* Nuclear Physics B 4 (1967).  
<sup>1645</sup> Translated from the original 1934 German article by C. P. Enz and C. H. Beck, pp. 1–  
<sup>1646</sup> 27 (cit. on p. 1).
- <sup>1647</sup> [5] D. J. Griffiths. *Introduction to Elementary Particles.* 2nd. Weinheim: Wiley-VCH,  
<sup>1648</sup> 2008. ISBN: 978-3-527-40601-2 (cit. on p. 1).
- <sup>1649</sup> [6] C. Yang and R. Mills. *Conservation of Isotopic Spin and Isotopic Gauge Invariance.*  
<sup>1650</sup> Phys. Rev. 96 (1 1954), pp. 191–195 (cit. on pp. 1, 10).
- <sup>1651</sup> [7] A. Milsted and T. J. Osborne. *Quantum Yang-Mills theory: An overview of a program.*  
<sup>1652</sup> Phys. Rev. D 98 (1 2018), p. 014505 (cit. on pp. 1, 10).

- 1653 [8] S. L. Glashow. *Partial-symmetries of weak interactions*. Nuclear Physics 22.4 (1961),  
1654 pp. 579–588. ISSN: 0029-5582 (cit. on p. 1).
- 1655 [9] D. J. Gross and F. Wilczek. *Ultraviolet Behavior of Non-Abelian Gauge Theories*.  
1656 Phys. Rev. Lett. 30 (26 1973), pp. 1343–1346 (cit. on p. 1).
- 1657 [10] H. D. Politzer. *Reliable Perturbative Results for Strong Interactions?* Phys. Rev. Lett.  
1658 30 (26 1973), pp. 1346–1349 (cit. on p. 1).
- 1659 [11] P. Higgs. *Broken symmetries and the masses of gauge bosons*. Phys. Rev. Lett. 13 (16  
1660 1964), pp. 508–509 (cit. on pp. 1, 14).
- 1661 [12] P. Higgs. *Broken symmetries, massless particles and gauge fields*. Physics Letters 12.2  
1662 (1964), pp. 132–133. ISSN: 0031-9163 (cit. on pp. 1, 14).
- 1663 [13] F. Englert and R. Brout. *Broken Symmetry and the Mass of Gauge Vector Mesons*.  
1664 Phys. Rev. Lett. 13 (9 1964), pp. 321–323 (cit. on pp. 1, 14).
- 1665 [14] S. Weinberg. *The making of the Standard Model*. The European Physical Journal C  
1666 34.1 (May 2004), 513. ISSN: 1434-6052. arXiv: hep-ph/0401010 [hep-ph] (cit. on  
1667 p. 2).
- 1668 [15] D. P. Barber et al. *Discovery of Three-Jet Events and a Test of Quantum Chromody-  
1669 namics at PETRA*. Phys. Rev. Lett. 43 (12 1979), pp. 830–833 (cit. on p. 2).
- 1670 [16] G. Arnison et al. *Experimental Observation of Isolated Large Transverse Energy Elec-  
1671 trons with Associated Missing Energy at  $\sqrt{s} = 540 \text{ GeV}$* . Phys. Lett. B 122 (1983),  
1672 pp. 103–116 (cit. on p. 2).

- 1673 [17] G. Arnison and others. *Experimental Observation of Lepton Pairs of Invariant Mass*  
1674       *Around  $95 \text{ GeV}/c^2$  at the CERN SPS Collider.* [Phys. Lett. B 126 \(1983\), pp. 398–410](#)  
1675       (cit. on p. 2).
- 1676 [18] CDF Collaboration. *Observation of Top Quark Production in  $\bar{p}p$  Collisions with the*  
1677       *Collider Detector at Fermilab.* [Phys. Rev. Lett. 74 \(14 1995\), pp. 2626–2631](#) (cit. on  
1678       p. 2).
- 1679 [19] DØ Collaboration. *Observation of the Top Quark.* [Phys. Rev. Lett. 74 \(14 1995\),](#)  
1680       pp. 2632–2637 (cit. on p. 2).
- 1681 [20] ATLAS Collaboration. *Observation of a new particle in the search for the Standard*  
1682       *Model Higgs boson with the ATLAS detector at the LHC.* [Phys. Lett. B 716 \(2012\),](#)  
1683       p. 1. arXiv: 1207.7214 [[hep-ex](#)] (cit. on pp. 2, 14).
- 1684 [21] CMS Collaboration. *Observation of a new boson at a mass of 125 GeV with the CMS*  
1685       *experiment at the LHC.* [Phys. Lett. B 716 \(2012\), p. 30.](#) arXiv: 1207.7235 [[hep-ex](#)]  
1686       (cit. on pp. 2, 14).
- 1687 [22] S. Navas et al. *Review of particle physics.* [Phys. Rev. D 110.3 \(2024\), p. 030001](#) (cit.  
1688       on pp. 2, 8).
- 1689 [23] Y. Fukuda et al. *Evidence for Oscillation of Atmospheric Neutrinos.* [Phys. Rev. Lett.](#)  
1690       81 (8 1998), pp. 1562–1567 (cit. on p. 2).
- 1691 [24] M. Cristinziani and M. Mulders. *Top-quark physics at the Large Hadron Collider.*  
1692       Journal of Physics G: Nuclear and Particle Physics 44.6 (2017), p. 063001. arXiv:  
1693       1606.00327 [[hep-ex](#)] (cit. on pp. 2, 8).

- 1694 [25] ATLAS and CMS Collaborations. *Combination of inclusive top-quark pair production*  
1695 *cross-section measurements using ATLAS and CMS data at  $\sqrt{s} = 7$  and 8 TeV.* JHEP  
1696 07 (2023), p. 213. arXiv: 2205.13830 [hep-ex] (cit. on p. 3).
- 1697 [26] C. Degrande, J.-M. Grard, C. Grojean, F. Maltoni, and G. Servant. *Non-resonant new*  
1698 *physics in top pair production at hadron colliders.* Journal of High Energy Physics  
1699 2011.3 (Mar. 2011). ISSN: 1029-8479. arXiv: 1010.6304 [hep-ph] (cit. on p. 3).
- 1700 [27] ATLAS Collaboration. *The ATLAS Experiment at the CERN Large Hadron Collider.*  
1701 JINST 3 (2008), S08003 (cit. on pp. 3, 21, 24, 25, 27–31).
- 1702 [28] ATLAS Collaboration. *Search for top-philic heavy resonances in pp collisions at  $\sqrt{s} =$*   
1703 *13 TeV with the ATLAS detector.* Eur. Phys. J. C 84 (2024), p. 157. arXiv: 2304.01678  
1704 [hep-ex] (cit. on pp. 3, 4, 17).
- 1705 [29] H. P. Nilles. *Supersymmetry, Supergravity and Particle Physics.* Phys. Rept. 110  
1706 (1984), pp. 1–162 (cit. on p. 3).
- 1707 [30] G. R. Farrar and P. Fayet. *Phenomenology of the Production, Decay, and Detection*  
1708 *of New Hadronic States Associated with Supersymmetry.* Phys. Lett. B 76 (1978),  
1709 pp. 575–579 (cit. on p. 3).
- 1710 [31] T. Plehn and T. M. P. Tait. *Seeking sgluons.* Journal of Physics G: Nuclear and  
1711 Particle Physics 36.7 (2009), p. 075001. arXiv: 0810.3919 [hep-ph] (cit. on p. 3).
- 1712 [32] S. Calvet, B. Fuks, P. Gris, and L. Valry. *Searching for sgluons in multitop events*  
1713 *at a center-of-mass energy of 8 TeV.* Journal of High Energy Physics 2013.4 (Apr.  
1714 2013). ISSN: 1029-8479. arXiv: 1212.3360 [hep-ph] (cit. on p. 3).

- 1715 [33] A. Pomarol and J. Serra. *Top quark compositeness: Feasibility and implications*. Phys-  
1716       ical Review D 78.7 (Oct. 2008). ISSN: 1550-2368. arXiv: 0806.3247 [hep-ph] (cit. on  
1717       p. 3).
- 1718 [34] K. Kumar, T. M. Tait, and R. Vega-Morales. *Manifestations of top compositeness at*  
1719       *colliders*. Journal of High Energy Physics 2009.05 (May 2009), 022022. ISSN: 1029-  
1720       8479. arXiv: 0901.3808 [hep-ph] (cit. on p. 3).
- 1721 [35] G. Banelli, E. Salvioni, J. Serra, T. Theil, and A. Weiler. *The present and future of*  
1722       *four top operators*. Journal of High Energy Physics 2021.2 (Feb. 2021). ISSN: 1029-  
1723       8479. arXiv: 2010.05915 [hep-ph] (cit. on p. 3).
- 1724 [36] R. Aoude, H. El Faham, F. Maltoni, and E. Vryonidou. *Complete SMEFT predictions*  
1725       *for four top quark production at hadron colliders*. Journal of High Energy Physics  
1726       2022.10 (Oct. 2022). ISSN: 1029-8479. arXiv: 2208.04962 [hep-ph] (cit. on p. 3).
- 1727 [37] C. Zhang. *Constraining qqtt operators from four-top production: a case for enhanced*  
1728       *EFT sensitivity*. Chinese Physics C 42.2 (Feb. 2018), p. 023104. ISSN: 1674-1137.  
1729       arXiv: 1708.05928 [hep-ph] (cit. on p. 3).
- 1730 [38] L. Darmé, B. Fuks, and F. Maltoni. *Topophilic heavy resonances in four-top final*  
1731       *states and their EFT interpretation*. Journal of High Energy Physics 2021.9 (Sept.  
1732       2021). ISSN: 1029-8479. arXiv: 2104.09512 [hep-ph] (cit. on pp. 3, 17).
- 1733 [39] N. Craig, F. D'Eramo, P. Draper, S. Thomas, and H. Zhang. *The Hunt for the Rest*  
1734       *of the Higgs Bosons*. JHEP 06 (2015), p. 137. arXiv: 1504.04630 [hep-ph] (cit. on  
1735       pp. 3, 17, 19).

- 1736 [40] N. Craig, J. Hajer, Y.-Y. Li, T. Liu, and H. Zhang. *Heavy Higgs bosons at low  $\tan \beta$ :  
1737 from the LHC to 100 TeV*. *Journal of High Energy Physics* 2017.1 (Jan. 2017). ISSN:  
1738 1029-8479. arXiv: [1605.08744 \[hep-ph\]](#) (cit. on pp. 3, 17, 19).
- 1739 [41] G. C. Branco et al. *Theory and phenomenology of two-Higgs-doublet models*. *Phys.  
1740 Rept.* 516 (2012), pp. 1–102. arXiv: [1106.0034 \[hep-ph\]](#) (cit. on pp. 3, 17, 19).
- 1741 [42] S. Gori, I.-W. Kim, N. R. Shah, and K. M. Zurek. *Closing the wedge: Search strategies  
1742 for extended Higgs sectors with heavy flavor final states*. *Phys. Rev. D* 93 (7 2016),  
1743 p. [075038](#) (cit. on pp. 3, 17, 19).
- 1744 [43] P. S. B. Dev and A. Pilaftsis. *Maximally symmetric two Higgs doublet model with  
1745 natural Standard Model alignment*. *Journal of High Energy Physics* 2014.12 (Dec.  
1746 2014), p. 024. arXiv: [1408.3405 \[hep-ph\]](#) (cit. on pp. 3, 17, 19).
- 1747 [44] ATLAS Collaboration. *Observation of four-top-quark production in the multilepton  
1748 final state with the ATLAS detector*. *Eur. Phys. J. C* 83 (2023), p. 496. arXiv: [2303.  
1749 15061 \[hep-ex\]](#) (cit. on pp. 3, 4, 17, 50, 60, 67, 77).
- 1750 [45] N. Greiner, K. Kong, J.-C. Park, S. C. Park, and J.-C. Winter. *Model-independent  
1751 production of a topophilic resonance at the LHC*. *Journal of High Energy Physics*  
1752 2015.4 (2015), p. 29. ISSN: 1029-8479. arXiv: [1410.6099 \[hep-ph\]](#) (cit. on pp. 3, 17–  
1753 19).
- 1754 [46] ATLAS Collaboration. *Evidence for  $t\bar{t}t\bar{t}$  production in the multilepton final state in  
1755 proton–proton collisions at  $\sqrt{s} = 13\text{TeV}$  with the ATLAS detector*. *Eur. Phys. J. C*  
1756 80 (2020), p. 1085. arXiv: [2007.14858 \[hep-ex\]](#) (cit. on pp. 4, 67).
- 1757 [47] D. H. Perkins. *Introduction to High Energy Physics*. 4th. Cambridge, UK: Cambridge  
1758 University Press, Apr. 2000. ISBN: 9780521621960 (cit. on p. 5).

- 1759 [48] C. Burgard and D. Galbraith. *Standard Model of Physics*. URL: <https://texample.net/model-physics/> (visited on 06/02/2025) (cit. on p. 6).
- 1760
- 1761 [49] H. Georgi. *Lie Algebras in Particle Physics: from Isospin to Unified Theories*. 2nd.
- 1762 CRC Press, 2000. ISBN: 9780429499210 (cit. on pp. 7, 10).
- 1763 [50] ATLAS and CMS Collaborations. *Combination of Measurements of the Top Quark*
- 1764 *Mass from Data Collected by the ATLAS and CMS Experiments at  $\sqrt{s} = 7$  and 8 TeV*.
- 1765 *Phys. Rev. Lett.* **132** (2023), p. 261902. arXiv: [2402.08713 \[hep-ex\]](https://arxiv.org/abs/2402.08713) (cit. on p. 8).
- 1766 [51] H. de la Torre and T. Farooque. *Looking beyond the Standard Model with Third Gen-*
- 1767 *eration Quarks at the LHC*. *Symmetry* **14**.3 (2022), p. 444 (cit. on p. 8).
- 1768 [52] Q.-H. Cao, J.-N. Fu, Y. Liu, X.-H. Wang, and R. Zhang. *Probing Top-philic New*
- 1769 *Physics via Four-Top-Quark Production*. *Chinese Physics C* **45**.9 (2021), p. 093107.
- 1770 arXiv: [2105.03372 \[hep-ph\]](https://arxiv.org/abs/2105.03372) (cit. on p. 8).
- 1771 [53] H. Beauchesne et al. *A case study about BSM vector resonances with direct couplings*
- 1772 *to the third quark generation*. *European Physical Journal C* **80**.5 (2020), p. 485. arXiv:
- 1773 [1908.11619 \[hep-ph\]](https://arxiv.org/abs/1908.11619) (cit. on p. 8).
- 1774 [54] F. Maltoni, D. Pagani, and S. Tentori. *Top-quark pair production as a probe of light*
- 1775 *top-philic scalars and anomalous Higgs interactions*. *Journal of High Energy Physics*
- 1776 **2024**.9 (Sept. 2024), p. 098. arXiv: [2406.06694 \[hep-ph\]](https://arxiv.org/abs/2406.06694) (cit. on p. 8).
- 1777 [55] CMS Collaboration. *Search for  $t\bar{t}H$  production in the  $H \rightarrow b\bar{b}$  decay channel with*
- 1778 *leptonic  $t\bar{t}$  decays in proton–proton collisions at  $\sqrt{s} = 13$  TeV*. *JHEP* **03** (2019),
- 1779 p. 026. arXiv: [1804.03682 \[hep-ex\]](https://arxiv.org/abs/1804.03682) (cit. on p. 8).

- 1780 [56] Y. Grossman and Y. Nir. *The Standard Model: From Fundamental Symmetries to Ex-*  
1781 *perimental Tests*. See Chapter 8.2. Cambridge University Press, 2023. ISBN: 9781009320378  
1782 (cit. on p. 9).
- 1783 [57] M. E. Peskin and D. V. Schroeder. *An Introduction to Quantum Field Theory*. 1st.  
1784 Reading, MA, USA: AddisonWesley, 1995. ISBN: 978-0-201-50397-5 (cit. on p. 9).
- 1785 [58] D. J. Gross. *The role of symmetry in fundamental physics*. Proceedings of the National  
1786 Academy of Sciences of the United States of America 93.25 (Dec. 1996), pp. 14256–  
1787 14259 (cit. on p. 9).
- 1788 [59] M. Bañados and I. Reyes. *A short review on Noethers theorems, gauge symmetries*  
1789 *and boundary terms*. International Journal of Modern Physics D 25.10 (Aug. 2016),  
1790 p. 1630021. ISSN: 1793-6594. arXiv: 1601.03616 [hep-th] (cit. on p. 9).
- 1791 [60] A. Pich. *The Standard Model of electroweak interactions. 2004 European School of*  
1792 *High-Energy Physics*. Feb. 2005, pp. 1–48. arXiv: hep-ph/0502010 [hep-ex] (cit. on  
1793 pp. 11–13).
- 1794 [61] P. Dev and A. Pilaftsis. *High-temperature electroweak symmetry non-restoration from*  
1795 *new fermions and implications for baryogenesis*. Journal of High Energy Physics  
1796 2020.9 (Sept. 2020), p. 012. arXiv: 2002.05174 [hep-ph] (cit. on p. 13).
- 1797 [62] J. Riebesell. *Higgs Potential*. URL: <https://tikz.net/higgs-potential/> (visited on  
1798 07/07/2025) (cit. on p. 15).
- 1799 [63] J. Goldstone, A. Salam, and S. Weinberg. *Broken Symmetries*. Phys. Rev. 127 (3  
1800 1962), pp. 965–970 (cit. on p. 15).
- 1801 [64] J. Ellis. *Higgs Physics. 2013 European School of High-Energy Physics*. 2015, pp. 117–  
1802 168. arXiv: 1312.5672 [hep-ph] (cit. on pp. 15, 16).

- 1803 [65] CDF Collaboration. *Search for New Physics in High-Mass Electron-Positron Events*  
1804        *in  $p\bar{p}$  Collisions at  $\sqrt{s} = 1.96$  TeV.* Phys. Rev. Lett. 99 (17 2007), p. 171802. arXiv:  
1805        0707.2524 [hep-ex] (cit. on p. 17).
- 1806 [66] M. Battaglia and G. Servant. *Four-top production and  $t\bar{t}$ +missing energy events at*  
1807        *multi TeV  $e^+e^-$  colliders.* Nuovo Cim. C 033N2 (2010), pp. 203–208. arXiv: 1005.4632  
1808        [hep-ex] (cit. on p. 17).
- 1809 [67] N. Arkani-Hamed, A. G. Cohen, and H. Georgi. *Electroweak symmetry breaking from*  
1810        *dimensional deconstruction.* Physics Letters B 513.1-2 (July 2001), pp. 232–240. arXiv:  
1811        hep-ph/0105239 [hep-ph] (cit. on p. 17).
- 1812 [68] T. Han, H. E. Logan, B. McElrath, and L.-T. Wang. *Phenomenology of the little Higgs*  
1813        *model.* Phys. Rev. D 67 (9 2003), p. 095004. arXiv: hep-ph/0301040 [hep-ph] (cit. on  
1814        p. 17).
- 1815 [69] P. Langacker and M. Plümacher. *Flavor changing effects in theories with a heavy  $Z'$*   
1816        *boson with family nonuniversal couplings.* Phys. Rev. D 62 (1 2000), p. 013006. arXiv:  
1817        hep-ph/0001204 [hep-ph] (cit. on p. 17).
- 1818 [70] P. Langacker. *The Physics of Heavy  $Z'$  Gauge Bosons.* Rev. Mod. Phys. 81 (2009),  
1819        pp. 1199–1228. arXiv: 0801.1345 [hep-ph] (cit. on p. 17).
- 1820 [71] J. H. Kim, K. Kong, S. J. Lee, and G. Mohlabeng. *Probing TeV scale top-philic*  
1821        *resonances with boosted top-tagging at the high luminosity LHC.* Phys. Rev. D 94 (3  
1822        2016), p. 035023. arXiv: 1604.07421 [hep-ph] (cit. on pp. 17, 85).
- 1823 [72] P. J. Fox, I. Low, and Y. Zhang. *Top-philic  $Z'$  forces at the LHC.* Journal of High  
1824        Energy Physics 2018.3 (Mar. 2018). ISSN: 1029-8479. arXiv: 1801.03505 [hep-ph]  
1825        (cit. on p. 17).

- 1826 [73] CMS Collaboration. *Observation of four top quark production in proton-proton col-*  
1827 *lisions at  $\sqrt{s} = 13\text{TeV}$* . Physics Letters B 847 (2023), p. 138290. arXiv: 2305.13439  
1828 [hep-ex] (cit. on p. 17).
- 1829 [74] G. Ferretti and D. Karateev. *Fermionic UV completions of composite Higgs models*.  
1830 Journal of High Energy Physics 2014.3 (Mar. 2014). ISSN: 1029-8479 (cit. on p. 19).
- 1831 [75] L. Vecchi. *A dangerous irrelevant UV-completion of the composite Higgs*. JHEP 02  
1832 (2017), p. 094. arXiv: 1506.00623 [hep-ph] (cit. on p. 19).
- 1833 [76] P. Sabatini. *Evidence for four-top-quarks production with the ATLAS detector at the*  
1834 *Large Hadron Collider*. Tech. rep. Geneva: CERN, 2021. URL: <https://cds.cern.ch/record/2784150> (cit. on p. 20).
- 1836 [77] L. Evans and P. Bryant. *LHC Machine*. JINST 3 (2008), S08001 (cit. on p. 21).
- 1837 [78] CMS Collaboration. *The CMS Experiment at the CERN LHC*. JINST 3 (2008),  
1838 S08004 (cit. on p. 21).
- 1839 [79] The ALICE Collaboration. *The ALICE experiment at the CERN LHC*. JINST 3  
1840 (2008), S08002 (cit. on p. 21).
- 1841 [80] The LHCb Collaboration. *The LHCb Detector at the LHC*. JINST 3 (2008), S08005  
1842 (cit. on p. 21).
- 1843 [81] E. e. a. Gschwendtner. *AWAKE, The Advanced Proton Driven Plasma Wakefield*  
1844 *Acceleration Experiment at CERN*. Nuclear Instruments and Methods in Physics Re-  
1845 search Section A 829 (2016), pp. 76–82. arXiv: 1512.05498 [physics.acc-ph] (cit. on  
1846 p. 22).

- 1847 [82] J. L. Feng, I. Galon, F. Kling, and S. Trojanowski. *ForwArd Search ExpeRiment at*  
1848 *the LHC*. Phys. Rev. D 97 (3 2018), p. 035001. arXiv: 1708.09389 [hep-ph] (cit. on  
1849 p. 22).
- 1850 [83] The KATRIN collaboration. *The design, construction, and commissioning of the KA-*  
1851 *TRIN experiment*. Journal of Instrumentation 16.08 (2021), T08015. arXiv: 2103.  
1852 04755 [physics.ins-det] (cit. on p. 22).
- 1853 [84] E. Lopienska. *The CERN accelerator complex, layout in 2022*. General Photo. 2022.  
1854 URL: <https://cds.cern.ch/record/2800984> (visited on 07/08/2025) (cit. on p. 22).
- 1855 [85] High Luminosity LHC Project Organization. *The HL-LHC project*. 2025. URL: <https://hilumilhc.web.cern.ch/content/hl-lhc-project> (visited on 06/11/2025) (cit. on  
1856 p. 23).
- 1857 [86] ATLAS Collaboration. *Performance of the ATLAS detector using first collision data*.  
1859 JHEP 09 (2010), p. 056. arXiv: 1005.5254 [hep-ex] (cit. on p. 23).
- 1860 [87] ATLAS Collaboration. *Luminosity determination in pp collisions at  $\sqrt{s} = 13 \text{ TeV}$*   
1861 *using the ATLAS detector at the LHC*. Eur. Phys. J. C 83 (2023), p. 982. arXiv:  
1862 2212.09379 [hep-ex] (cit. on pp. 24, 50, 70).
- 1863 [88] J. M. Butterworth, G. Dissertori, and G. P. Salam. *Hard Processes in Proton-Proton*  
1864 *Collisions at the Large Hadron Collider*. Annu. Rev. Nucl. Part. Sci. 62 (2012),  
1865 pp. 387–405. arXiv: 1202.0583 [hep-ex] (cit. on p. 24).
- 1866 [89] J. Campbell, J. Huston, and W. J. Stirling. *Hard interactions of quarks and gluons:*  
1867 *a primer for LHC physics*. Reports on Progress in Physics 70.1 (2006), p. 89. arXiv:  
1868 hep-ph/0611148 [hep-ex] (cit. on p. 24).

- 1869 [90] ATLAS Collaboration. *Standard Model Summary Plots October 2023*. ATL-PHYS-  
1870 PUB-2023-039. 2023. URL: <https://cds.cern.ch/record/2882448> (cit. on p. 25).
- 1871 [91] J. Pequenao and P. Schaffner. *How ATLAS detects particles: diagram of particle*  
1872 *paths in the detector*. 2013. URL: <https://cds.cern.ch/record/1505342> (visited on  
1873 07/08/2025) (cit. on p. 26).
- 1874 [92] J. Pequenao. *Computer generated image of the ATLAS inner detector*. 2008. URL:  
1875 <https://cds.cern.ch/record/1095926> (visited on 07/08/2025) (cit. on p. 27).
- 1876 [93] J. Pequenao. *Computer Generated image of the ATLAS calorimeter*. 2008. URL: <https://cds.cern.ch/record/1095927> (visited on 07/08/2025) (cit. on p. 29).
- 1878 [94] ATLAS Collaboration. *Operation of the ATLAS trigger system in Run 2*. **JINST** 15  
1879 (2020), P10004. arXiv: [2007.12539 \[physics.ins-det\]](https://arxiv.org/abs/2007.12539) (cit. on p. 32).
- 1880 [95] ATLAS Collaboration. *Performance of the ATLAS track reconstruction algorithms*  
1881 *in dense environments in LHC Run 2*. **Eur. Phys. J. C** 77 (2017), p. 673. arXiv:  
1882 [1704.07983 \[hep-ex\]](https://arxiv.org/abs/1704.07983) (cit. on p. 33).
- 1883 [96] T. Cornelissen et al. *Concepts, design and implementation of the ATLAS New Track-*  
1884 *ing (NEWT)*. Tech. rep. Geneva: CERN, 2007. URL: <https://cds.cern.ch/record/1020106> (cit. on p. 33).
- 1886 [97] A. Salzburger. *Optimisation of the ATLAS Track Reconstruction Software for Run-2*.  
1887 *Journal of Physics: Conference Series* 664.7 (2015), p. 072042 (cit. on p. 33).
- 1888 [98] R. Frühwirth. *Application of Kalman filtering to track and vertex fitting*. **Nucl. In-**  
1889 *strum. Methods Phys. Res. A* 262.2 (1987), pp. 444–450. ISSN: 0168-9002 (cit. on  
1890 p. 33).

- 1891 [99] T. Cornelissen et al. *The global  $\chi^2$  track fitter in ATLAS*. Journal of Physics: Con-  
1892 ference Series 119.3 (2008), p. 032013 (cit. on p. 33).
- 1893 [100] ATLAS Collaboration. *Improved electron reconstruction in ATLAS using the Gaus-  
1894 sian Sum Filter-based model for bremsstrahlung*. ATLAS-CONF-2012-047. 2012. URL:  
1895 <https://cds.cern.ch/record/1449796> (cit. on p. 33).
- 1896 [101] D. Wicke. *A new algorithm for solving tracking ambiguities*. Tech. rep. Oct. 1998.  
1897 URL: <https://cds.cern.ch/record/2625731> (cit. on p. 34).
- 1898 [102] ATLAS Collaboration. *Reconstruction of primary vertices at the ATLAS experiment  
1899 in Run 1 proton–proton collisions at the LHC*. Eur. Phys. J. C 77 (2017), p. 332.  
1900 arXiv: [1611.10235 \[physics.ins-det\]](https://arxiv.org/abs/1611.10235) (cit. on p. 34).
- 1901 [103] W. Waltenberger, R. Frühwirth, and P. Vanlaer. *Adaptive vertex fitting*. Journal of  
1902 Physics G: Nuclear and Particle Physics 34.12 (2007), N343 (cit. on p. 34).
- 1903 [104] ATLAS Collaboration. *Secondary vertex finding for jet flavour identification with the  
1904 ATLAS detector*. ATL-PHYS-PUB-2017-011. 2017. URL: <https://cds.cern.ch/record/2270366> (cit. on p. 34).
- 1905 [105] ATLAS Collaboration. *Performance of pile-up mitigation techniques for jets in pp  
collisions at  $\sqrt{s} = 8 \text{ TeV}$  using the ATLAS detector*. Eur. Phys. J. C 76 (2016),  
1907 p. 581. arXiv: [1510.03823 \[hep-ex\]](https://arxiv.org/abs/1510.03823) (cit. on pp. 35, 38).
- 1908 [106] ATLAS Collaboration. *Topological cell clustering in the ATLAS calorimeters and its  
1909 performance in LHC Run 1*. Eur. Phys. J. C 77 (2017), p. 490. arXiv: [1603.02934](https://arxiv.org/abs/1603.02934)  
1910 [hep-ex] (cit. on pp. 35, 36).
- 1911

- 1912 [107] ATLAS Collaboration. *Jet reconstruction and performance using particle flow with*  
1913 *the ATLAS Detector.* *Eur. Phys. J. C* **77** (2017), p. 466. arXiv: [1703.10485 \[hep-ex\]](#)  
1914 (cit. on p. 37).
- 1915 [108] M. Cacciari, G. P. Salam, and G. Soyez. *The anti- $k_t$  jet clustering algorithm.* *JHEP*  
1916 **04** (2008), p. 063. arXiv: [0802.1189 \[hep-ph\]](#) (cit. on p. 37).
- 1917 [109] ATLAS Collaboration. *Jet energy scale and resolution measured in proton–proton*  
1918 *collisions at  $\sqrt{s} = 13\text{ TeV}$  with the ATLAS detector.* *Eur. Phys. J. C* **81** (2021),  
1919 p. 689. arXiv: [2007.02645 \[hep-ex\]](#) (cit. on pp. 38, 72–74).
- 1920 [110] ATLAS Collaboration. *Jet energy scale measurements and their systematic uncertainties*  
1921 *in proton–proton collisions at  $\sqrt{s} = 13\text{ TeV}$  with the ATLAS detector.* *Phys. Rev.*  
1922 **D 96** (2017), p. 072002. arXiv: [1703.09665 \[hep-ex\]](#) (cit. on pp. 38, 72).
- 1923 [111] ATLAS Collaboration. *Transforming jet flavour tagging at ATLAS.* Tech. rep. Sub-  
1924 mitted to: Nature Communications. Geneva: CERN, 2025. arXiv: [2505.19689](#) (cit. on  
1925 pp. 39–41).
- 1926 [112] A. Vaswani et al. *Attention Is All You Need.* 2023. arXiv: [1706.03762 \[cs.CL\]](#) (cit. on  
1927 p. 39).
- 1928 [113] ATLAS Collaboration. *Measurements of  $b$ -jet tagging efficiency with the ATLAS de-*  
1929 *tector using  $t\bar{t}$  events at  $\sqrt{s} = 13\text{ TeV}.$*  *JHEP* **08** (2018), p. 089. arXiv: [1805.01845](#)  
1930 [[hep-ex](#)] (cit. on pp. 41, 74).
- 1931 [114] ATLAS Collaboration. *Electron reconstruction and identification in the ATLAS ex-*  
1932 *periment using the 2015 and 2016 LHC proton–proton collision data at  $\sqrt{s} = 13\text{ TeV}.$*   
1933 *Eur. Phys. J. C* **79** (2019), p. 639. arXiv: [1902.04655 \[physics.ins-det\]](#) (cit. on  
1934 pp. 42–44).

- 1935 [115] ATLAS Collaboration. *Electron Identification with a Convolutional Neural Network*  
1936            *in the ATLAS Experiment*. ATL-PHYS-PUB-2023-001. 2023. URL: <https://cds.cern.ch/record/2850666>.
- 1937
- 1938 [116] ATLAS Collaboration. *Muon reconstruction and identification efficiency in ATLAS*  
1939            *using the full Run 2 pp collision data set at  $\sqrt{s} = 13 \text{ TeV}$* . *Eur. Phys. J. C* **81** (2021),  
1940            p. 578. arXiv: [2012.00578 \[hep-ex\]](https://arxiv.org/abs/2012.00578) (cit. on pp. 45, 46).
- 1941 [117] ATLAS Collaboration. *Muon reconstruction performance of the ATLAS detector in*  
1942            *proton–proton collision data at  $\sqrt{s} = 13 \text{ TeV}$* . *Eur. Phys. J. C* **76** (2016), p. 292. arXiv:  
1943            [1603.05598 \[hep-ex\]](https://arxiv.org/abs/1603.05598) (cit. on p. 46).
- 1944 [118] ATLAS Collaboration. *Performance of missing transverse momentum reconstruction*  
1945            *with the ATLAS detector using proton–proton collisions at  $\sqrt{s} = 13 \text{ TeV}$* . *Eur. Phys.*  
1946            *J. C* **78** (2018), p. 903. arXiv: [1802.08168 \[hep-ex\]](https://arxiv.org/abs/1802.08168) (cit. on pp. 47, 74).
- 1947 [119] ATLAS Collaboration.  *$E_T^{\text{miss}}$  performance in the ATLAS detector using 2015–2016*  
1948            *LHC pp collisions*. ATLAS-CONF-2018-023. 2018. URL: <https://cds.cern.ch/record/2625233> (cit. on p. 48).
- 1949
- 1950 [120] J. Alwall et al. *The automated computation of tree-level and next-to-leading order*  
1951            *differential cross sections, and their matching to parton shower simulations*. *JHEP* **07**  
1952            (2014), p. 079. arXiv: [1405.0301 \[hep-ph\]](https://arxiv.org/abs/1405.0301) (cit. on pp. 51, 53, 54).
- 1953 [121] NNPDF Collaboration, R. D. Ball, et al. *Parton distributions for the LHC run II*.  
1954            *JHEP* **04** (2015), p. 040. arXiv: [1410.8849 \[hep-ph\]](https://arxiv.org/abs/1410.8849) (cit. on pp. 51, 53, 54).
- 1955 [122] T. Sjöstrand et al. *An introduction to PYTHIA 8.2*. *Comput. Phys. Commun.* **191**  
1956            (2015), p. 159. arXiv: [1410.3012 \[hep-ph\]](https://arxiv.org/abs/1410.3012) (cit. on pp. 51, 53, 54).

- 1957 [123] ATLAS Collaboration. *ATLAS Pythia 8 tunes to 7 TeV data*. ATL-PHYS-PUB-2014-  
 1958 021. 2014. URL: <https://cds.cern.ch/record/1966419> (cit. on pp. 53, 54).
- 1959 [124] S. Frixione, E. Laenen, P. Motylinski, and B. R. Webber. *Angular correlations of*  
 1960 *lepton pairs from vector boson and top quark decays in Monte Carlo simulations*.  
 1961 JHEP 04 (2007), p. 081. arXiv: [hep-ph/0702198](https://arxiv.org/abs/hep-ph/0702198) (cit. on p. 53).
- 1962 [125] P. Artoisenet, R. Frederix, O. Mattelaer, and R. Rietkerk. *Automatic spin-entangled*  
 1963 *decays of heavy resonances in Monte Carlo simulations*. JHEP 03 (2013), p. 015.  
 1964 arXiv: [1212.3460 \[hep-ph\]](https://arxiv.org/abs/1212.3460) (cit. on p. 53).
- 1965 [126] D. J. Lange. *The EvtGen particle decay simulation package*. Nucl. Instrum. Meth. A  
 1966 462 (2001), p. 152 (cit. on p. 53).
- 1967 [127] R. Frederix, D. Pagani, and M. Zaro. *Large NLO corrections in  $t\bar{t}W^\pm$  and  $t\bar{t}t\bar{t}$*   
 1968 *hadroproduction from supposedly subleading EW contributions*. JHEP 02 (2018), p. 031.  
 1969 arXiv: [1711.02116 \[hep-ph\]](https://arxiv.org/abs/1711.02116) (cit. on pp. 53, 76).
- 1970 [128] E. Bothmann et al. *Event generation with Sherpa 2.2*. SciPost Phys. 7.3 (2019), p. 034.  
 1971 arXiv: [1905.09127 \[hep-ph\]](https://arxiv.org/abs/1905.09127) (cit. on pp. 53, 54).
- 1972 [129] S. Schumann and F. Krauss. *A parton shower algorithm based on Catani–Seymour*  
 1973 *dipole factorisation*. JHEP 03 (2008), p. 038. arXiv: [0709.1027 \[hep-ph\]](https://arxiv.org/abs/0709.1027) (cit. on  
 1974 p. 53).
- 1975 [130] S. Höche, F. Krauss, M. Schönher, and F. Siegert. *A critical appraisal of NLO+PS*  
 1976 *matching methods*. JHEP 09 (2012), p. 049. arXiv: [1111.1220 \[hep-ph\]](https://arxiv.org/abs/1111.1220) (cit. on p. 53).
- 1977 [131] S. Höche, F. Krauss, M. Schönher, and F. Siegert. *QCD matrix elements + parton*  
 1978 *showers. The NLO case*. JHEP 04 (2013), p. 027. arXiv: [1207.5030 \[hep-ph\]](https://arxiv.org/abs/1207.5030) (cit. on  
 1979 p. 53).

- 1980 [132] S. Catani, F. Krauss, B. R. Webber, and R. Kuhn. *QCD Matrix Elements + Parton  
1981 Showers*. JHEP 11 (2001), p. 063. arXiv: [hep-ph/0109231](#) (cit. on p. 53).
- 1982 [133] S. Höche, F. Krauss, S. Schumann, and F. Siegert. *QCD matrix elements and truncated  
1983 showers*. JHEP 05 (2009), p. 053. arXiv: [0903.1219 \[hep-ph\]](#) (cit. on p. 53).
- 1984 [134] F. Caccioli, P. Maierhöfer, and S. Pozzorini. *Scattering Amplitudes with Open Loops*.  
1985 Phys. Rev. Lett. 108 (2012), p. 111601. arXiv: [1111.5206 \[hep-ph\]](#) (cit. on p. 53).
- 1986 [135] A. Denner, S. Dittmaier, and L. Hofer. *COLLIER: A fortran-based complex one-loop  
1987 library in extended regularizations*. Comput. Phys. Commun. 212 (2017), pp. 220–238.  
1988 arXiv: [1604.06792 \[hep-ph\]](#) (cit. on p. 53).
- 1989 [136] F. Buccioni et al. *OpenLoops 2*. Eur. Phys. J. C 79.10 (2019), p. 866. arXiv: [1907.13071](#)  
1990 [[hep-ph](#)] (cit. on p. 53).
- 1991 [137] ATLAS Collaboration. *ATLAS data quality operations and performance for 2015–  
1992 2018 data-taking*. JINST 15 (2020), P04003. arXiv: [1911.04632 \[physics.ins-det\]](#)  
1993 (cit. on p. 55).
- 1994 [138] ATLAS Collaboration. *Analysis of  $t\bar{t}H$  and  $t\bar{t}W$  production in multilepton final states  
1995 with the ATLAS detector*. ATLAS-CONF-2019-045. 2019. URL: <https://cds.cern.ch/record/2693930> (cit. on pp. 60, 64, 78).
- 1997 [139] ATLAS Collaboration. *Measurement of the total and differential cross-sections of  $t\bar{t}W$   
1998 production in  $pp$  collisions at  $\sqrt{s} = 13 \text{ TeV}$  with the ATLAS detector*. JHEP 05 (2024),  
1999 p. 131. arXiv: [2401.05299 \[hep-ex\]](#) (cit. on p. 62).
- 2000 [140] ATLAS Collaboration. *Search for new phenomena in events with same-charge leptons  
2001 and  $b$ -jets in  $pp$  collisions at  $\sqrt{s} = 13 \text{ TeV}$  with the ATLAS detector*. JHEP 12 (2018),  
2002 p. 039. arXiv: [1807.11883 \[hep-ex\]](#) (cit. on p. 65).

- 2003 [141] ATLAS Collaboration. *Search for R-parity-violating supersymmetry in a final state*  
2004 *containing leptons and many jets with the ATLAS experiment using  $\sqrt{s} = 13\text{ TeV}$*   
2005 *proton–proton collision data.* *Eur. Phys. J. C* **81** (2021), p. 1023. arXiv: [2106.09609](https://arxiv.org/abs/2106.09609)  
2006 [[hep-ex](#)] (cit. on p. 67).
- 2007 [142] E. Gerwick, T. Plehn, S. Schumann, and P. Schichtel. *Scaling Patterns for QCD Jets.*  
2008 *JHEP* **10** (2012), p. 162. arXiv: [1208.3676](https://arxiv.org/abs/1208.3676) [[hep-ph](#)] (cit. on pp. 67, 68).
- 2009 [143] G. Avoni et al. *The new LUCID-2 detector for luminosity measurement and moni-*  
2010 *toring in ATLAS.* *JINST* **13.07** (2018), P07017 (cit. on p. 70).
- 2011 [144] ATLAS Collaboration. *Tagging and suppression of pileup jets.* ATL-PHYS-PUB-2014-  
2012 001. 2014. URL: <https://cds.cern.ch/record/1643929> (cit. on pp. 72, 74).
- 2013 [145] ATLAS Collaboration. *Measurements of inclusive and differential fiducial cross-sections*  
2014 *of  $t\bar{t}$  production with additional heavy-flavour jets in proton–proton collisions at  $\sqrt{s} =$*   
2015 *13 TeV with the ATLAS detector.* *JHEP* **04** (2019), p. 046. arXiv: [1811.12113](https://arxiv.org/abs/1811.12113) [[hep-ex](#)]  
2016 (cit. on p. 76).
- 2017 [146] D. de Florian et al. *Handbook of LHC Higgs Cross Sections: 4. Deciphering the Nature*  
2018 *of the Higgs Sector.* CERN Yellow Rep. Monogr. 2 (2017), pp. 1–869. arXiv: [1610.07922](https://arxiv.org/abs/1610.07922) [[hep-ph](#)] (cit. on p. 76).
- 2020 [147] ATLAS Collaboration. *Measurement of the production cross-section of a single top*  
2021 *quark in association with a Z boson in proton–proton collisions at 13 TeV with the*  
2022 *ATLAS detector.* ATLAS-CONF-2017-052. 2017. URL: <https://cds.cern.ch/record/2273868> (cit. on p. 76).

- 2024 [148] F. Demartin, B. Maier, F. Maltoni, K. Mawatari, and M. Zaro. *tWH associated*  
2025 *production at the LHC*. EPJC 77.1 (2017). arXiv: 1607.05862 [hep-ph]. URL: <https://doi.org/10.1140/epjc/s10052-017-4601-7> (cit. on p. 76).
- 2026
- 2027 [149] ATLAS Collaboration. *Measurement of  $W^\pm Z$  production cross sections and gauge*  
2028 *boson polarisation in pp collisions at  $\sqrt{s} = 13$  TeV with the ATLAS detector*. Eur.
- 2029 Phys. J. C 79 (2019), p. 535. arXiv: 1902.05759 [hep-ex] (cit. on p. 76).
- 2030 [150] G. Cowan, K. Cranmer, E. Gross, and O. Vitells. *Asymptotic formulae for likelihood-*  
2031 *based tests of new physics*. The European Physical Journal C 71.2 (Feb. 2011). ISSN:  
2032 1434-6052. arXiv: 1007.1727 [physics.data-an]. URL: <http://dx.doi.org/10.1140/epjc/s10052-011-1554-0> (cit. on p. 80).
- 2033
- 2034 [151] J. Neyman and E. S. Pearson. *IX. On the problem of the most efficient tests of*  
2035 *statistical hypotheses*. Philosophical Transactions of the Royal Society of London.  
2036 Series A, Containing Papers of a Mathematical or Physical Character 231.694-706  
2037 (1933), pp. 289–337 (cit. on p. 80).
- 2038 [152] S. S. Wilks. *The large-sample distribution of the likelihood ratio for testing composite*  
2039 *hypotheses*. Annals of Mathematical Statistics 9.1 (1938), pp. 60–62 (cit. on p. 81).
- 2040 [153] T. Junk. *Confidence level computation for combining searches with small statistics*.  
2041 Nuclear Instruments and Methods in Physics Research Section A: Accelerators, Spec-  
2042 *rometers, Detectors and Associated Equipment* 434.23 (Sept. 1999), 435443. ISSN:  
2043 0168-9002. arXiv: hep-ex/9902006 [hep-ex] (cit. on p. 82).
- 2044 [154] A. L. Read. *Modified frequentist analysis of search results: The CLs method*. Tech.  
2045 rep. CERN-OPEN-2000-205. Presented at Workshop on Confidence Limits, Geneva,  
2046 Switzerland. CERN, 2000. URL: <https://cds.cern.ch/record/451614> (cit. on p. 82).